12-2021

An Examination of Environmental Applications for Uncooled Thermal Infrared Remote Sensing Instruments

Cody M. Webber
cmw3698@rit.edu

ROCHESTER INSTITUTE OF TECHNOLOGY

An Examination of Environmental Applications for Uncooled Thermal Infrared Remote Sensing Instruments

---

By Cody M Webber

A dissertation submitted in partial fulfillment of the requirements for the degree of Doctor of Philosophy in Imaging Science

Chester F. Carlson Center for Imaging Science

College of Science

Rochester Institute of Technology

December 2021

CHESTER F. CARLSON CENTER FOR IMAGING SCIENCE
COLLEGE OF SCIENCE
ROCHESTER INSTITUTE OF TECHNOLOGY
ROCHESTER, NEW YORK

CERTIFICATE OF APPROVAL

Ph.D. DEGREE DISSERTATION

The Ph.D. Degree Dissertation of Cody M. Webber has
been examined and approved by the
dissertation committee as satisfactory for the
dissertation required for the
Ph.D. degree in Imaging Science

Dr. John P. Kerekes, Advisor

Dr. Alan Raisanen, External Chair

Dr. Carl Salvaggio

Dr. Aaron Gerace

Date

"Education without values, as useful as it is, seems rather to make man a more clever devil"

C.S. Lewis

For Kara

ROCHESTER INSTITUTE OF TECHNOLOGY

Abstract

Chester F. Carlson Center for Imaging Science

An Examination of Environmental Applications for Uncooled Thermal Infrared Remote Sensing Instruments

by Cody M. WEBBER

Advancements in system design for thermal instruments require assessment of potential environmental applications and appropriate data processing techniques. A novel multi-band thermal imaging system was proposed by DRS Leonardo for the National Aeronautics and Space Administration Earth Science Technology Office Instrument Incubator Program, for which these criteria were assessed. The Multi-Band Uncooled Radiometer Imager (MURI) is a six spectral channel instrument designed to collect images in the thermal infrared, specifically in the range of 7.5 to 12.5 μm. The work detailed in this thesis characterizes the ability of a thermal imager with an uncooled microbolometer focal plane array to provide valuable data for environmental science applications. Here, a pair of studies using simulated data demonstrates the ability of a multispectral instrument such as MURI to detect enhanced levels of atmospheric methane using a novel approach that performs similarly to a state of the art algorithm when applied to MURI data. The novel method is evaluated using a controlled concentration simulated dataset to determine the extent of its detection capabilities and its dependence on atmospheric conditions. The methane investigations reveal the system is capable of detecting a 20 m thick CH_4 plume of 10-20 ppm above background levels when column water vapor is low using both the NDMI and matched filter approaches. Additionally, land surface temperature and emissivity retrieval techniques were applied to experimental MURI data recorded during initial test flights to assess their accuracy with MURI data. Utilizing split window and Temperature Emissivity Separation make this examination distinct as this establishes that proven methods can be applied to uncooled multiband imager data. Application of these methods to MURI data demonstrated the system is capable of temperature retrievals with Root Mean Square Errors of less than 1 K to measured reference values and surface emissivity retrievals within 2% of reference database values. The definition and application of the Normalized Differential Methane Index in this thesis demonstrates a novel approach for detection of enhanced plumes of methane utilizing a multispectral system with only a single band allocated to methane absorption features.

Acknowledgements

I would like to express my gratitude to the members of my committee for their guidance and willingness to make this project a positive and collaborative effort. To Dr. Kerekes, thank you for helping me become a better scientist and communicator.

Next, I would like to thank the MURI team from DRS Leonardo and acknowledge the efforts of the other members of the RIT MURI science team: Aaron Gerace, Tania Kleynhans, Rehman Eon. Much of the work performed in this thesis would not have been possible without your help. A special thank you to Nina Raqueño for your efforts towards the data collection, making instrument training easy, and for being an excellent person to travel with. Additional thank yous to Jared Gregor and Jon Miller for joining the data collection campaign. Special thanks to Rolando Raqueño for your guidance and for the time you set aside to help me.

To my instructors, thank you for showing passion in teaching and for the great job you do laying the foundations of knowledge that makes this work possible. Of course, I must acknowledge the administrative staff of CIS who made everything about this project, and my time as a graduate student in the center, operate smoothly. To Colleen McMahon, Mel Warren, and Marci Sanders-Arnett, thank you for making travel and purchases for this project hassle free. Thank you Beth Lockwood and Joyce French for all of you administrative assistance over the years.

To the members of my class: it was a true pleasure being able to go through graduate school alongside such bright and fun people as you. I have fond memories of every one of you, so I thank you not only for those, but everything you taught me as well. Special thanks to Anjali Jogeshwar, Baabak Mamaghani, and Zachary Mulhollan; I've always loved to learn, but it was a lot more enjoyable and easier to learn with you.

Finally, I'd like to thank my family. To my mother and father, I couldn't have asked for more loving and supportive parents, or better models of work ethic. Thank you for all you have done for me. To the rest of my family, Nicole, Jordan, Sally, Rich, Dewey, Margie, Nancy, Bruce, and Camille, thank you for always making me feel loved and supported. Kara, there is so much to thank you for. There is no one I

would rather spend a year in lockdown with. None of this would have been possible without you.

Contents

List of Figures

List of Tables

List of Abbreviations

GSD	**G**round **S**ample **D**istance
HITRAN	**HI**gh-resolution **TRAN**smission molecular absorption database
HyTES	**Hy**perspectral **T**hermal **E**mission **S**pectrometer
LSE	**L**and **S**urface **E**missivity
LST	**L**and **S**urface **T**emperature
MMD	**M**aximum-**M**inimum **D**ifference
MODTRAN	**MOD**erate resolution atmospheric **TRAN**smission computer code
MURI	**M**ulti Band **U**ncooled **R**adiameter **I**mager
NDMI	**N**ormalized **D**iffernti**a**l **M**ethane **I**ndex
NEdL	**N**oise **E**quivalent **d**elta Radiance
NEdT	**N**oise **E**quivalent **d**elta **T**emperature
NEM	**N**ormalized **E**missivity **M**ethod
RMSE	**R**oot **M**ean **S**quared **E**rror
ROI	**R**egion **O**f **I**nterest
SE	**S**urface **E**missivity
SRM	**S**pectral **R**atio **M**odule
ST	**S**urface **T**emperature
TES	**T**emperature **E**missivity **S**eparation
TIRS	**T**hermal **I**nfrared **S**ensor

Physical Constants

Planck's Constant	$h = 6.626\,070\,15 \times 10^{-34}\,\mathrm{J/s}$
Speed of Light	$c = 2.997\,924\,58 \times 10^{8}\,\mathrm{m\,s^{-1}}$
Boltzmann constant	$k_B = 1.380\,649 \times 10^{-23}\,\mathrm{J/K}$

Chapter 1

Introduction and Motivation

1.1 Introduction

The field of remote sensing provides tools suitable for large scale environmental monitoring and research. Remote imagers and detectors have the unique ability to record sizeable swaths of land surface and atmospheric column data without requiring costly and time consuming ground truth collections. Imaging systems designed to collect data in the thermal infrared have demonstrated the ability to determine land surface temperature and retrieve land surface emissivity [24, 35, 36, 59, 94, 93], both of which are important variables for studying climatology, evapotranspiration, and vegetation monitoring [50, 53, 59]. Airborne imagers have been used to detect the presence of enhanced levels or rogue emissions of gasses [17, 47, 55, 89, 90]. Advancements in system design for thermal instruments requires assessment of potential environmental applications and data processing methods. The work performed for this thesis evaluates the potential of an uncooled multispectral imaging system to provide data viable for environmental applications. This evaluation includes identifying and formulating methods for a multispectral instrument to retrieve land surface temperature and identify enhanced levels of atmospheric gasses. In order to accomplish these goals, the Multiband Uncooled Radiometer Imager (MURI) instrument was chosen as an example for evaluating methods and applications.

1.2 Motivation for Thesis

DRS Leonardo proposed a novel multi-band thermal imaging system for the National Aeronautics and Space Administration Earth Science Technology Office Instrument Incubator Program. The design for this system utilizes a microbolometer focal plane array. This allows the imaging instrument to operate at ambient temperature without requiring a cooling system for the focal plane array. The Multi-Band Uncooled Radiometer Imager (MURI) is a six spectral channel instrument designed to collect images in the thermal infrared, specifically in the range of 7.5 to 12.5 μm. In preparation for test flights of the airborne demonstration instrument, the science team at the Rochester Institute of Technology was tasked with producing performance predictions as well as exploring environmental applications and methods that could utilize MURI's six bands [28].

The six MURI bands are specified below in Table 1.1, along with potential applications. This thesis will focus on two environmental applications. The first application is methane monitoring. MURI's band 1 is allocated to overlap with a set of strong absorption features present around 7.68 μm. The second application is retrieval of surface temperature. Of the six bands, two bands are allocated to resemble the Thermal Infrared Sensor (TIRS) aboard NASA's Landsat 8 satellite, which is used for land surface temperature retrieval. This overlap provides an avenue for comparison between temperature retrieval methods applied to MURI and TIRS [28].

TABLE 1.1: MURI Band Allocations and Potential Applications

Band #	Center Wavelength	Band Width	Potential Application
B1	$7.68\mu m$	$0.10\mu m$	methane monitoring
B2	$8.55\mu m$	$0.35\mu m$	SO_2, cloud/volcanic ash properties
B3	$9.07\mu m$	$0.36\mu m$	surface minerals, SO_2
B4	$10.05\mu m$	$0.54\mu m$	LST, vegetation, surface minerals
B5	$10.90\mu m$	$0.59\mu m$	LST, TIRS (band 10) overlap
B6	$12.05\mu m$	$1.01\mu m$	LST, TIRS (band 11) overlap

1.2.1 Detection of Enhanced Atmospheric Methane Using Simulated Multispectral Remote Sensing Data Context and Motivation

Remote detection of methane is a useful tool for detecting and eliminating rogue emission sources. In an effort to be applied to the field of enhanced methane detection, the design of the MURI instrument takes advantage of a collection of methane absorption lines around 7.6 μm by including a single spectral band centered on 7.68 μm. The studies described in Chapter 3 were performed in order to determine if detection of enhanced levels of atmospheric methane was possible with only a single broadband thermal infrared channel dedicated to methane spectral features. In support of that goal, identifying methods of enhanced methane detection that could work with a multispectral instrument was essential. Once we established detection was possible with the system, predicting detectable scenarios became the new focus.

1.2.2 Motivation and Context for Examination of Land Surface Temperature Retrieval Methods on Simulated MURI Data

Land surface temperature is a key factor and the direct driving force in the exchange of long-wave infrared radiation at the interface between the surface of the Earth and the atmosphere [59][70]. Accurate land surface temperature retrievals are important for a myriad of environmental remote sensing applications such as evapotranspiration, vegetation monitoring, and carbon flux mapping [1][50][53]. A primary goal of the MURI project is to demonstrate that accurate land surfaces temperature retrievals can be accomplished using an uncooled microbolometer imager. Chapter 4 details efforts to identify multispectral temperature retrieval methods to use on MURI data collected during test flights. Land surface temperature will serve as the primary metric of comparison between this instrument and the state of the art, Landsat 8 TIRS, and ground truth measurements.

1.2.3 Motivation and Context for Enhanced Atmospheric Methane Detection Method Validation Experiments

While Chapter 3 details the efforts to determine the effectiveness of detecting enhanced level of atmospheric methane, Chapter 5 details attempts to validate both the

MURI system's methane detection capabilities and the novel approach to methane detection designed using the MURI system's specifications. While a physical experiment was planned, due to the novel coronavirus pandemic of 2020, simulated data are once again used here in place of collected thermal infrared imagery. As detection with the system and the novel approach have been determined to be possible, the focus is to validate the results and characterize performance across various scenarios.

1.2.4 Motivation and Context for Land Surface Temperature Retrieval for MURI's Airborne Demonstration Instrument

Initial test flights for MURI's airborne demonstration instrument were performed in August and September of 2019. These test flights are the first opportunity to validate not only the ability of MURI to collect images, but the methods chosen for data evaluation. Test flights for the MURI system provide an avenue for validating the system's temperature retrieval capability using real MURI data. During these test flights, ground surface measurements of temperature and emissivity were recorded. Chapter 6 describes the test flight experimental setup to record ground measurements and provides the results of applying two temperature retrieval methods to real MURI data for these test flights. During the application of the Temperature and Emissivity Separation method, an examination was performed to examine the best way to calculate coefficients necessary for the algorithm.

1.3 Objectives

The overall goal of the MURI science team at RIT is to produce performance predictions and test flight results for MURI in the environmental applications of enhanced atmospheric methane detection and land surface temperature retrieval. This thesis describes three primary objectives pursued in support of that goal:

1. Determine the Atmospheric Methane Detection Capability of the MURI Instrument

   (a) Identify or define multispectral methods for methane detection (Matched Filter and Normalized Differential Methane Index)

   (b) Identify scene conditions that allow for detection of enhanced atmospheric methane using the MURI instrument

2. Characterize the Land Surface Temperature Retrieval Capabilities of the MURI Instrument

   (a) MURI performance predictions using the Split Window Technique and comparison to Landsat 8 TIRS

   (b) Identify a temperature retrieval approach that utilizes all 6 MURI bands (TES)

3. Validate the MURI Instrumental Design and Performance Predictions

   (a) Perform a controlled concentration methane experiment (simulated substitute)

   (b) Compile ground reference data for MURI test flights over temperature and methane targets

   (c) Apply temperature retrieval and methane detection methods to representative MURI data and characterize performance.

1.4 Contribution

Demonstration of this system's capability to retrieve land surface temperatures and land surface emissivities establishes the value of these novel uncooled imagers to provide data for environmental applications. Utilizing split window and Temperature Emissivity Separation make this examination distinct as this establishes that state of the art methods can be applied to uncooled multiband imager data. This thesis also describes a novel approach for detection of enhanced plumes of methane utilizing a multispectral system with only a single band allocated to methane absorption features. The methane detection investigations include the definition and validation of a novel approach to methane detection: the normalized differential methane index.

1.5 Thesis Proposal Layout

This thesis is organized according to the following objectives. Chapter 1 details the motivation and context for the studies performed in this thesis. Chapter 2 provides relevant and important background information on the radiometric equations that describe the remote sensing scenarios of interest as well as details of the MURI instrument. Chapter 3 details the work done to meet objective 1, determining the MURI system's methane detection capability. The work performed to meet objective 2 is detailed in Chapter 4. The last objective is split between Chapters 5 and 6, which detail validation effort for methane detection and the application of temperature/emissivity retrieval techniques on MURI data respectively. Chapter 7 provides a conclusion and Chapter 8 details future directions from the work described in this thesis.

1.6 Related Publications

1.6.1 Conference Proceedings

- Webber, C.M., Kerekes, J.P., Raqueno, R., Detecting Enhanced Levels of Atmospheric Methane Using Thermal Infrared Imagery, *Atmospheric Transmission Models- Modeling In Remote Sensing*, June 5^{th}, 2018, Newton, Massachusetts, ATM.

- Kerekes, J.P., Webber, C.M., Raqueno, R., Methane Detection in the Longwave Infrared, *International Geoscience and Remote Sensing Symposium*, July 24^{th}, 2018, Valencia, Spain, IEEE.

1.6.2 Journal Publications

- Webber, C.M., Kerekes, J.P., An Examination of Enhanced Atmospheric Methane Detection Methods for Predicting Performance of a Novel Multiband Uncooled Radiometer Imager, *Atmospheric Measurement Techniques*, vol 13, 5359-5367, October 9^{th}, 2020

- Gerace, A., Eon, R., Kleynhans, T., Raqueno, N., Webber, C.M., Ely, P., Ventresco, S., In-Flight Performance of the Multi-band Uncooled Radiometer Instrument (MURI) Thermal Sensor, Under review with *Remote Sensing of Environment*.

Chapter 2

Background

2.1 Radiometric Theory of Thermal Infrared Energy

This section discusses the basic radiometry and necessary considerations for the remote sensing studies presented in this thesis. This section begins with a discussion of the general radiometric equation for thermal infrared systems, describing in detail the main radiometric contributions to at sensor radiance in the thermal infrared. The section will then provide a discussion of the radiometric equation for the specific case of an enhanced level of atmospheric gas in the column, including a discussion of the effect of a plume in absorption or emission on sensor reaching radiance.

2.1.1 General Radiometric Equation for Sensor Reaching Radiance

The Multiband Uncooled Radiometer Imager is sensitive to energy in the thermal infrared (TIR) of the electromagnetic radiation spectrum, around 7 to 14 μm. This range of wavelengths covers the peak of the emission curves for warm surfaces on Earth and is a spectral range where the atmosphere is relatively transparent [25][41][87]. In Earth remote sensing, this region is typically dominated by the emission of surfaces due to their temperatures. This feature of this spectral region is advantageous as it does not rely on reflected solar energy, and therefore provides an avenue of 24-hour remote sensing with a passive system, or a system without a source [78][87].

While the sensor reaching radiance in the thermal infrared is typically dominated by radiance emitted from the Earth's surface, it can better be described as a

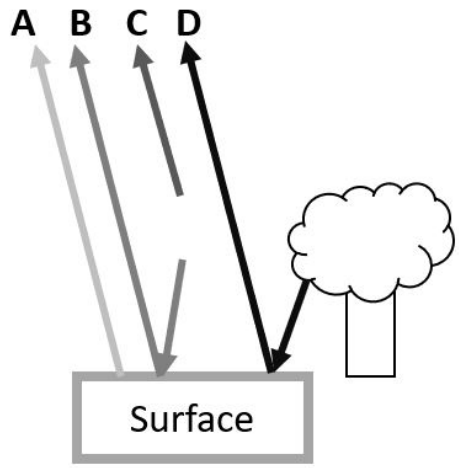

FIGURE 2.1: Thermal energy paths that contribute to sensor reaching radiance.

combination of surface leaving radiance, atmospheric path radiance, and reflected downwelling sky irradiance. Surface emission can be defined as:

$$L_{surface} = \epsilon(\lambda)B(\lambda, T) \tag{2.1}$$

where ϵ is the emissivity of the surface, λ is the wavelength, T is temperature, and B is the wavelength dependant Planck function describing the radiation of energy from a blackbody, or a perfect emitter. The Planck Function is defined as:

$$B = \frac{2hc^2}{\lambda^5} \frac{1}{e^{\frac{hc}{\lambda kT}} - 1} \tag{2.2}$$

where h is Planck's constant, c is the speed of light, and k is the Boltzmann constant. An ideal blackbody would emit radiance according to this function, and can be defined to have an emissivity, ϵ, of 1. Earth surfaces, however, have a wavelength dependant emissivity function that describes how the surface emits energy in reference to the ideal blackbody.

The total radiance emitted from the surface then passes through the atmosphere before reaching the sensor. While the atmosphere is highly transmissive throughout the thermal infrared, it is not perfectly transmissive, and some of the radiance from the surface will be absorbed or deflected, resulting in some attenuation of the surface radiance. The resultant radiance is described as Path A radiance, as shown in 2.1,

and can be defined as:

$$L_A = \epsilon(\lambda)B(\lambda, T)\tau(\lambda) \tag{2.3}$$

where τ describes the wavelength dependant transmissivity of the path through the atmosphere.

The next contribution to the sensor leaving radiance can also be described as a contributor to surface leaving radiance. This is a contribution by downwelling irradiance, or energy radiated from the atmosphere, which is reflected from the surface back to the sensor. Conservation of energy requires all incident flux must be absorbed, transmitted, or reflected. The conservation of energy relationship can be written in terms of emission, as Kirchoff's law states that, for an object at thermal equilibrium, emissivity must be equal to the absorbance [41][87].

$$1 = \epsilon(\lambda) + \tau(\lambda) + \rho(\lambda) \tag{2.4}$$

Where ρ is the surfaces reflectance. For opaque objects, or objects with negligable transmissivity, the equation can be written as:

$$1 = \epsilon(\lambda) + \rho(\lambda) \tag{2.5}$$

It follows that the equation can be written as:

$$1 - \epsilon(\lambda) = \rho(\lambda) \tag{2.6}$$

Therefore, the reflected downwelling irradiance that contributes to surface leaving radiance can be written as:

$$L_{dsl} = [1 - \epsilon(\lambda)]L_d(\lambda) \tag{2.7}$$

This radiance then passes through the atmosphere before reaching the sensor, experiencing some attenuation. This radiance can be described as Path B radiance:

$$L_B = [1 - \epsilon(\lambda)]L_d(\lambda)\tau(\lambda) \tag{2.8}$$

The next considerable contributor for thermal scene is Path C radiance, or upwelling atmospheric radiance for the path between the sensor and the surface. This will simply be referred to as L_u [78][102].

Finally, the last considerable contributor is reflected background radiance, which can also be described as a contributor to total target surface emission. This is energy emitted from an off target surface that is reflected from the target surface back through the atmosphere, experiencing attenuation. This is written as path D radiance:

$$L_D = [1 - \epsilon(\lambda)]\epsilon_{ots}(\lambda)B(\lambda, T_{ots})\tau(\lambda) \tag{2.9}$$

where ϵ_{ots} and T_{ots} describe the emissivity and temperature of the off target surface. As the emissivity of the surface increases, the contributions for both Path B and D lessen. For high emissivity targets Path B and D become negligible [78].

Unlike other spectral regions, the sensor reaching radiance contributions from direct and reflected solar irradiance are negligible in the thermal infrared, and therefore is not required for considerations in these models. The final equation including major contributors can be written as:

$$L_{sr} = L_A + L_B + L_C + L_D \tag{2.10}$$

$$L_{sr} = \epsilon(\lambda)B(\lambda, T)\tau(\lambda) + L_u(\lambda) + [1-\epsilon(\lambda)]L_d(\lambda)\tau(\lambda) + [1-\epsilon(\lambda)]\epsilon_{ots}(\lambda)B(\lambda, T_{ots})\tau(\lambda) \tag{2.11}$$

2.1.2 Radiometric Equation Describing the Presence of a Localized Gas Plume in the Atmospheric Column

The presence of a gas plume in the atmospheric column between a detector and the ground introduces an additional emission term due to the temperature of the plume and a transmissivity term, to describe the attenuation of the surface radiance due to the presence of the plume. Beer's law defines the weak plume transmissivity as:

$$\tau_{plume}(\lambda) = e^{-n_o b(\lambda)} \tag{2.12}$$

where n_o is defined as the gas column density and b is defined as the gas absorbance spectra. The gas absorbance spectra is also referred to as the plume signature. This transmission function can be simplified by first expanding the function via the Taylor Series Expansion:

$$\tau_{plume}(\lambda) = 1 - n_o b(\lambda) + \frac{n_o^2 b^2(\lambda)}{2!} - \frac{n_o^3 b^3(\lambda)}{3!} + ... \tag{2.13}$$

By making the assumption that the plume is optically thin, meaning $n_o b$, or plume absorbance is small, equation can be simplified to:

$$\tau_{plume}(\lambda) \approx 1 - n_o b(\lambda) \tag{2.14}$$

It follows that the Beer-Lambert law can be used to write the transittance in terms of emissivity [47][78]. Rearranging the equation to solve for emissivity yields the following equation:

$$\epsilon_{plume} = 1 - \tau_{plume}(\lambda) \approx n_o b(\lambda) \tag{2.15}$$

With this information, the contribution to sensor reaching radiance of the emissions of the plume can be written as:

$$L_{plume} = \epsilon_{plume} B(\lambda, T_{plume}) \tau_{atm}(\lambda) = n_o b(\lambda) B(\lambda, T_{plume}) \tau_{atm}(\lambda) \tag{2.16}$$

This path will be referred to as Path E, which is shown in 2.2. The remaining effects of the plume will are applied to the surface leaving radiance and are defined by including the additional transmissivity term:

$$L_{sr} = \tau_{plume} L_A + \tau_{plume} L_B + L_C + \tau_{plume} L_D + L_{plume} \tag{2.17}$$

Substituting in the values from above the equation becomes:

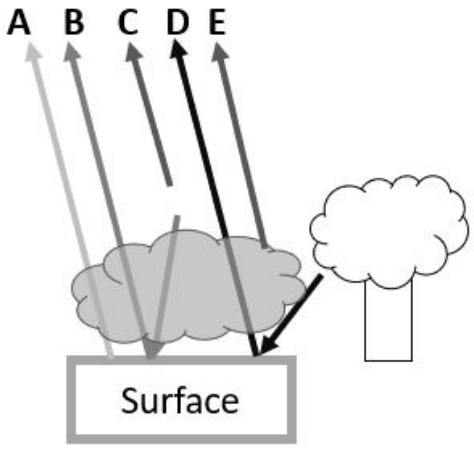

FIGURE 2.2: Thermal energy paths that contribute to sensor reaching radiance.

$$L_{sr} = \epsilon(\lambda)\tau[B(\lambda,T) - L_d - \epsilon_{ots}B(\lambda,T_{ots})] + \tau[L_d + \epsilon_{ots}B(\lambda,T_{ots})] + n_o b(\lambda)(\lambda)[B(\lambda,T_{plume}) - \epsilon_{ots}B(\lambda,T_{ots})] - \tau[L_d + \epsilon_{ots}B(\lambda,T_{ots})]] + L_u \quad (2.18)$$

While this equation is long, it is best explained as the ground leaving radiance passing through the plume experiences attenuation due to the plume and due to the atmosphere. The plume emitted radiance also experiences attenuation due to the atmosphere. In a simpler form, this equation can be written as:

$$L_{sr} = L_u + L_{groundleaving}(\lambda)\tau + n_o b(\lambda)\tau[B(\lambda,T_{ots}) - L_{groundleaving}(\lambda)] \quad (2.19)$$

Note that a plume experiencing higher absorption will attenuate the ground leaving radiance more, leading to lower radiances in wavelengths where the plume absorbs. Plumes experiencing high emissions, typically at higher temperatures, will contribute higher radiance from the plume emission term, following Planck's law for blackbody radiation.

2.2 Details of the MURI Instrument

This section details the specifications of the MURI instrument, first by describing the microbolometer components of the focal plane array.

2.2.1 MURI System Concept

Leonardo DRS has proposed a Multi-Band Uncooled Radiometer Imager (MURI) for the National Aeronautics and Space Administration's Instrument Incubator Program (IIP). IIP is designed to promote advancement in remote sensing technologies and techniques by funding projects that demonstrate feasible improvement in the field[67]. The MURI instrument is designed to collect images in the thermal infrared which will be applied to the study of land surface climatology, soil moisture content, ecosystem dynamics, hazard and volcano emission (SO_2) monitoring, and methane detection [28]. The goal of this project is to demonstrate the potential value of utilizing low cost microbolometers in Earth science remote sensing applications. DRS Technologies aims to show that implementing methods applied in the construction of MURI will reduce the cost and development time for airborne and space based imagers while maintaining a satisfactory performance in the thermal region of the infrared. Two designs have been compiled for the MURI: an airborne demonstration system and a satellite mounted system. The airborne demonstration instrument has been constructed and test fights were performed in September and October of 2019. The airborne systems utilize a $17\mu m/pixel$ microbolometer FPA, an integration time of $14\mu s$, and uses optics with an effective focal length of $120mm$ and an f_{number} of 1. The design utilizes six spectral channels which are detailed in Table 2.1, along with predictions of Noise Equivalent delta Temperature (NEdT) or the minimum brightness temperature difference each band can detect, provided by DRS [26].

The MURI system is designed with the specific goal of achieving land surface temperature retrievals with acceptable accuracy in comparison to the state of the art system Landsat 8's Thermal Infrared Sensor (TIRS). Of the six bands proposed for the MURI design, two bands (band 5 and 6) were designed to overlap with TIRS. Figure 2.3 provides a visual representation of the spectral response functions of the two TIRS bands and the as-built filter function for MURI band 5 and 6[4][26][74][88].

TABLE 2.1: MURI Band Allocations and Predicted Noise Equivalent delta Temperature

Band #	Center Wavelength	Band Width	Predicted NEdT
B1	7.68μm	0.10μm	0.256K
B2	8.55μm	0.35μm	0.076K
B3	9.07μm	0.36μm	0.078K
B4	10.05μm	0.54μm	0.059K
B5	10.90μm	0.59μm	0.061K
B6	12.05μm	1.01μm	0.036K

The similarity in response not only allows for comparison between the two systems, but also potentially allows any methodologies applied to TIRS to data to be viable for the MURI system.

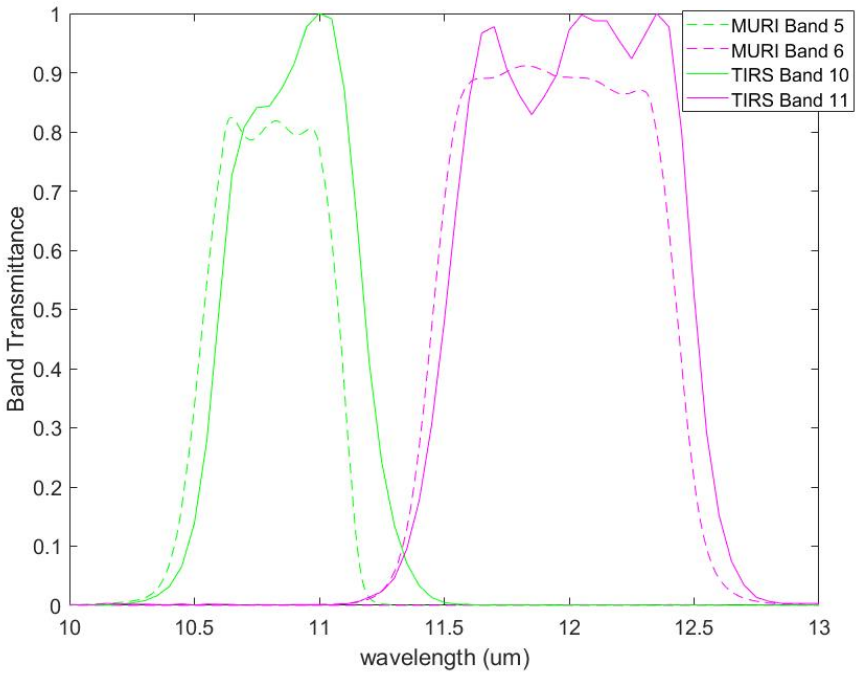

FIGURE 2.3: Comparison between sample MURI filter functions for band 5 and 6 and TIRS responsivity curves.

2.2.2 Microbolometer Focal Plane Array

The MURI system utilizes a relatively low cost microbolometer focal plane array (FPA). Generally, bolometers are thermal infrared detectors that measure changes in incident thermal energy. They typically consist of a material that absorbs infrared

radiation, a thermometer, a thermal heatsink, a thermal insulator, and readout electronics. The absorption of energy leads to a change in temperature for the bolometer, which affects the resistance of the bolometer's elements. It is this change in resistance that is used to measure the change in radiation incident on the bolometer [14][72].

In addition to being relatively cheap, microbolometer FPAs can perform at ambient temperature and therefore do not require potentially expensive and heavy cooling systems like other thermal systems, such as ASTER, MODIS, ECOSTRESS or HyTES [16][81][42]. The lack of a required cooling system not only reduces the cost of microbolometer FPA instruments but reduces the number of elements that could fail in the operation of the instrument and reduces power consumption. The benefits to size, cost, and power consumption distinguish microbolometers as a valuable alternative focal plane array element [14][72].

Long-wave infrared (LWIR) microbolometers cover a spectral range that is useful for Earth observation. This range of wavelengths (8 to 13 μm) covers the peak of the emission curves for warm surfaces on Earth and is a spectral range where the atmosphere is relatively transparent. One issue in utilizing microbolometers for taking airborne measurements is that microbolometers have a relatively long time constant [25][28]. The need for a longer time constant issue is exacerbated by the sensitivity degradation caused by the narrowband filters, which are required for spectral sampling for each band. The long time constant aboard a traveling platform would lead to image smear. To account for this, as well as the low sensitivity of the microbolometers, DRS has designed a backscanning method that uses a scanning piezo stage to match the velocity of the platform and allow the microbolometer to record over a target surface for a longer amount of time. A computer aided design model of the MURI focal plane array and the piezo stage can be seen in Figure 2.4[32][28][29]. The piezo backscan method allows the system to record multiple images of the same target, which provides a way to stack frames of the same target [28][29]. Figure 2.5 provides an illustration of how the step-and-stare operation of the piezo stage was designed to reduce motion blur and compensate for the necessarily long time constant[29].

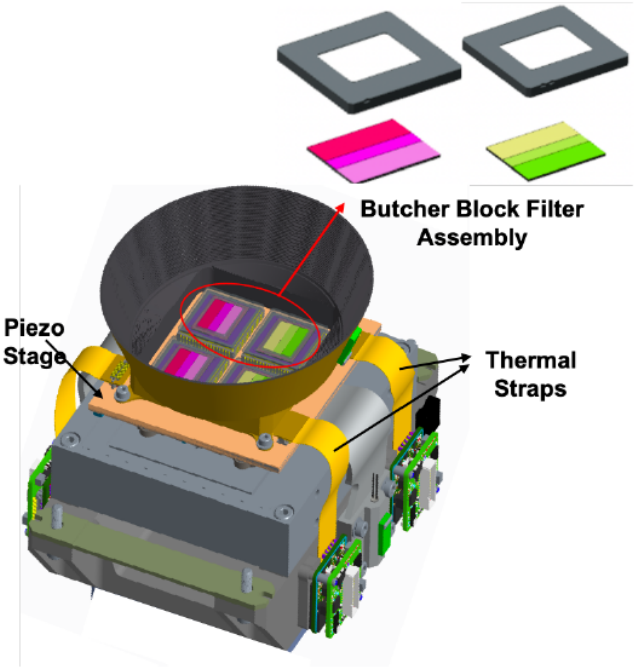

FIGURE 2.4: CAD model of MURI focal plane array, butcher block filter assembly and piezo stage. Figure used with permission of author from Gerace et. al 2021 [32]

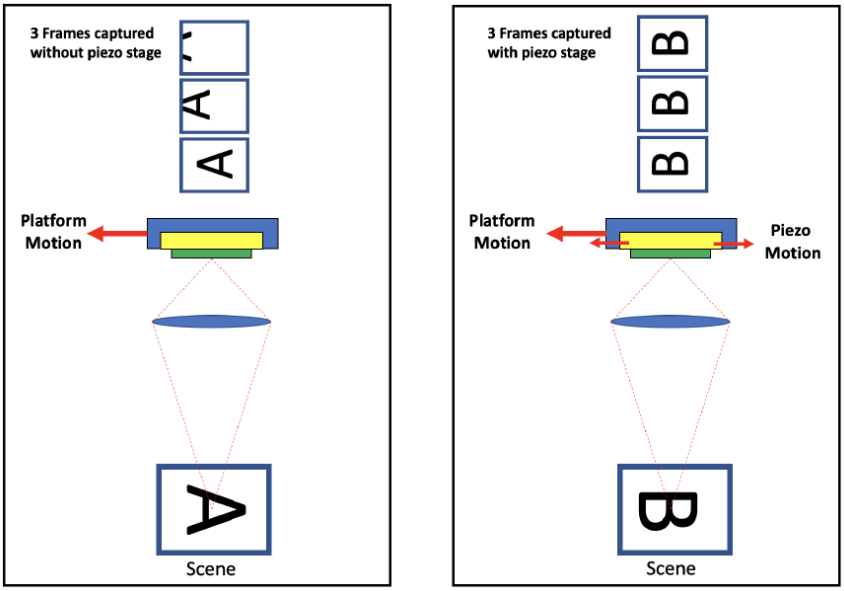

FIGURE 2.5: Illustration of operation of MURI's piezo stage. Left: demonstration of MURI imaging with piezo stage stationary. Right: demonstraction of MURI imaging with piezo stage active. Figure used with permission of author from Gerace et. al 2021 [32]

As the name suggests, the microbolometer focal plane array of the MURI system is uncooled. This leads to image data that is sensitive to the temperature of the surrounding environment and in-scene temperature. A combination of methods are used to combat this sensitivity. First, MURI is designed with a set of thermal straps, heaters at the base of the straps, and a heater control loop, which helps to keep the focal plane at a constant temperature. Second, the system lens is temperature controlled using a heat sink. Third, the instrument is covered with thermal insulation. Finally, a periodic offset calibration using a blackbody of known temperature is performed. This approach restores the instrument's digital counts output using the known temperature reference, which reduces the lens assembly's effect on the radiance. The contributions of these three approaches improves radiometric accuracy of MURI's measurements [32].

2.2.3 Airborne Demonstration Instrument

The airborne system is designed to be mounted on a bush plane or small passenger aircraft and fly at 4.572 km (15000 ft) with a 0.65 m ground sample distance (GSD). During the 2019 testflights, the instrument was flown at 3.35 km (11000 ft) above surface level, resulting in a GSD of 0.48 m. The instrument utilizes four 640x480 Tamarisk, or Tam, microbolometer detector arrays. The Tams are covered with butcher block filter assemblies which contain the filters for the six MURI bands. Tam 1 and Tam 2 are equipped with filters for bands 1, 3, and 5, while Tam 3 and 4 are designed to collect images for bands 2, 4, and 6. The Tams are arranged such that Tam 1 and Tam 3 record the same swath of ground, and the same is true for Tam 2 and 4, as shown in Figure 2.6. Note, the space between the two sets of Tams means that there will be a gap between the parallel strips of MURI data [32].

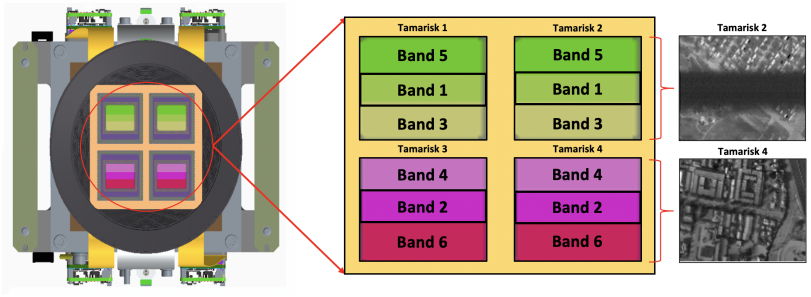

FIGURE 2.6: Illustration of the arrangement of MURI's filters across the four Tams. On the right is MURI data recorded by Tam 2 and 4 over Southern California in October 2020. Figure used with permission of author from Gerace et. al 2021 [32]

Chapter 3

Examination of Enhanced Atmospheric Methane Detection Methods for Predicting Performance of a Novel Multiband Uncooled Radiometer Imager

3.1 Introduction

3.1.1 Context for Examination of Enhanced Atmospheric Methane Detection Capability Study

With the increased risk of climate change, the value of global environmental monitoring has become increasingly important. Methane (CH_4), which naturally exists as the most abundant organic gas in the atmosphere [20], is a potent greenhouse gas with a radiative forcing per molecule approximately 20 times greater than carbon dioxide (CO_2) [71]; [84]. While the atmospheric concentration of methane is lower than that of CO_2, the world has seen a rise in CH_4 emissions since 2007, primarily from anthropogenic sources. CH_4 also has a moderately short lifespan in the atmosphere (about ten years), which means that efforts to reduce anthropogenic emission of CH_4 would aid in slowing human contribution to climate change in a relatively short amount of time. The benefit of curbing CH_4 emissions makes it desirable to

monitor likely sources of CH_4 in order to quantify and limit emission from human activity [77].

Airborne and satellite mounted remote imaging systems provide researchers with the ability to rapidly survey large swaths of Earth's surface and the atmospheric columns above the surface. This feature of remote imaging makes it a useful tool for monitoring atmospheric gas content and sources of rogue emissions. In the shortwave infrared, the Airborne Visible/Infrared Imaging Spectrometer AVIRIS and its successor AVIRIS-NG are high spatial resolution, high spectral resolution imagers that have demonstrated the ability to detect enhanced levels of atmospheric methane by observing strong methane absorption features present between 2.0 and 2.5um [89, 90]. The satellite mounted systems, TROPOspheric Measuring Instrument (TROPOMI) and Greenhouse gases Observing Satellite (GOSAT) are capable of measuring global atmospheric methane content using solar backscattering [45]. The Methane Remote Sensing Lidar Mission (MERLIN) Minisatellite was scheduled to launch in 2020, but has since been rescheduled to launch in 2024. This mission will utilize a short wave infrared source to detect methane plumes [49].

Longwave, or thermal, infrared hyperspectral imagery have been used to identify and track the movement of gas plumes in cluttered urban environments [17]. The Hyperspectral Thermal Emission Spectrometer (HyTES) is a high spectral resolution imager that has proved capable of detecting rogue methane emission sources by utilizing a clutter matched filter approach [47]. The clutter matched filter method, when applied to HyTES imagery, has been proved capable of detecting enhanced levels of methane gas from both cluttered urban environments, such as the La Brea tar pits in Los Angeles, California, and from managed rural scenes, such as oil fields in Kern County, California. HyTES has also been used to develop an algorithm that can predict methane concentration from thermal imagery [55]. Unlike SWIR imagers like AVIRIS and TROPOMI, thermal infared imagers utilize thermal emissions and thermal contrast between gas plumes and background surfaces to detect enhanced levels of atmospheric gases without relying on solar backscattering or an additional source. This feature of thermal imagers makes them useful for nighttime operation as well as removes dependency on surface reflectance properties [47]. However, thermal imagers, such as HyTES, require focal plane array (FPA) cooling systems in

order to reduce noise [17][47].

Improvements in remote thermal imaging systems and the design of new systems necessitates the evaluation of methane detection capabilities. MURI's band 1 has been allocated to be centered on a collection of strong methane absoprtion features located around 7.68 um[28]. The design's 6 spectral channels are detailed again in Table 3.1, along with DRS predictions of Noise Equivalent delta Temperature (NEdT) or the minimum brightness temperature difference each band can detect for the airborne instrument.

The inspiration for this study was to determine if it is possible to detect enhanced levels of atmospheric CH_4 in the thermal infrared using a multispectral instrument with a single band allocated to CH_4 absorption features. To accomplish this, three different types of detection schemes were examined in order to predict performance and provide evidence for which methods provide useful results when applied to multispectral data from an instrument like MURI.

TABLE 3.1: MURI Band Allocations and Predicted Noise Equivalent delta Temperature

Band #	Center Wavelength	Band Width	Predicted NEdT
B1	7.68um	0.10um	0.256K
B2	8.55um	0.35um	0.076K
B3	9.07um	0.36um	0.078K
B4	10.05um	0.54um	0.059k
B5	10.90um	0.59um	0.061K
B6	12.05um	1.01um	0.036K

3.2 Mutispectral Methods for Detecting Enhanced Levels of Atmospheric Methane

In this section, three methods of methane detection used to determine detectable cases for the uncooled instrument are described.

3.2.1 Single Pixel NEdT Comparison

The first study presented here investigates the potential contrast for a single thermal infrared spectral band centered on the CH_4 absorption feature present at 7.68 μm.

Here, a narrow bandpass of 100 nm is considered. The goal of the study is to determine under what scenarios a single band allocated to CH_4 detection is capable of detecting the temperature difference indicative of an enhanced level of atmospheric CH_4.

In order to accomplish this, sensor reaching radiances were calculated using radiative transfer models produced with MODTRAN6. This modeling code provides the ability to define a background surface, surface temperature, and atmosphere to calculate the spectral radiance that reaches a single pixel at the system's height. Utilizing the local chemical plume model option in MODTRAN6, spectral radiances, L_{spec} were calculated for a background case, or a case without enhanced levels of CH_4, and a plume present case, or a case with enhanced levels of CH_4 [13].

Effective radiances, or the amount of light energy that the system is responsive to, can be calculated from the spectral radiance:

$$L_{eff} = \frac{\int_{\lambda_i}^{\lambda_j} L_{spec} R d\lambda}{\int_{\lambda_i}^{\lambda_j} R d\lambda} \tag{3.1}$$

where R is the responsivity of the pixel and λ_i and λ_j are the wavelength limits [78]. Note that this effective radiance is normalized by the responsivity curve of the spectral channel of the instrument. From effective radiance the brightness or effective temperature can be calculated, which is the temperature perceived from the imaging system in reference to a black body.

$$T_{brightness} = \frac{hc}{\lambda_{center} k_b \log \frac{hc}{L_{eff} \lambda_{center}^5}} \tag{3.2}$$

where h is Planck's constant, c is the speed of light, k_b is the Stephan Boltzman constant, and λ_{center} is the center wavelength of the band [78]. By calculating a brightness temperature for both the background and plume present case and then taking the difference of the resultant brightness temperatures, a brightness temperature difference was found. Comparing this brightness temperature difference to the Noise Equivalent delta Temperature (NEdT), or the minimum brightness temperature difference the system is capable of detecting, reveals if the system would be able to detect the increased concentration of CH_4 utilizing only the CH_4 band.

3.2.2 Methane Detection Utilizing a Matched Filter

In order to better assess the system's methane detection capabilities, an approach proven to work for hyperspectral imagery was considered. The study presented here utilizes a matched filter approach to assess MURI's capability of detecting enhanced levels of atmospheric CH_4. While this method has been proven capable of detecting CH_4 using thermal infrared HyTES data, applying the matched filter here is to investigate the viability of this method with a system with considerably fewer spectral bands (6 compared to 256) and only a single band allocated to the thermal infrared CH_4 absorption feature.

The objective of developing a matched filter is to create a weighting function that when applied to an N spatial pixel by n spectral channel radiance matrix, L, the output is a new image where intensity correlates with the presence of the signal of inquiry. Application of the matched filter begins with the assumption that there exists a signal, in this case a methane plume absorption or emission signal, b, that is linearly superimposed on a background of the image, which can be written as:

$$r = \alpha b + c \tag{3.3}$$

where r is the sensor reaching radiance, α is the strength of the spectral signal, and c is a combination of noise and background signal [31, 47]. A realistic model of c considers the correlation between spectral channels, which can be described in terms of the covariance matrix K:

$$K = < c'c'^T > = \frac{1}{N} L'L'^T \tag{3.4}$$

where L' is mean subtracted radiance over all the pixels from matrix L. Knowing, K, the covariance of the image, the optimal matched filter can be matched to both the desired signal b and the background, or "clutter". This clutter matched filter is defined as:

$$q = \frac{K^{-1}b}{\sqrt{b^T K^{-1} b}} \tag{3.5}$$

It should be noted that q is normalized so that if the signal is not present in the

original image, the resultant matched filter image will prove to have a variance of 1. By applying the matched filter q to the N by n matrix of radiances L, the clutter matched filter image is created:

$$CMFI = q^T L \tag{3.6}$$

After computing the CMFI, a simple threshold is applied to determine if the signal is present [31, 47]. For this study, the threshold was varied in order to produce a Receiver Operator Characteristic (ROC) curve to assess the effectiveness of the method, rather than the effectiveness of a single threshold.

The study presented here provides a comparison between the 6 channel multispectral MURI instrument and the 256 channel hyperspectral HyTES instrument when applying the matched filter to simulated imagery containing enhanced levels of atmospheric CH_4.

3.2.3 Methane Detection Using a Normalized Differential Methane Index

The final study described here aims to determine if detection of enhanced atmospheric CH_4 is possible using information from pair of thermal spectral channels. This method has seen use in vegetation based studies in the form of the normalized difference vegetation index, or NDVI [73]. Here, a normalized difference methane index, or NDMI, is calculated using the following equation:

$$NDMI = \frac{SB2 - SB1}{SB2 + SB1} \tag{3.7}$$

Where SB2 and SB1 are the radiance values recorded by two different spectral bands from the instrument which cover the same spatial pixel area, one that includes a CH_4 feature (SB1) and one that does not (SB2). The result is an image of intensity values that can be compared to threshold to determine if CH_4 is present. If the plume is absorbing more thermal energy than passes through and is emitted by it, higher values for NDMI indicate a stronger likelihood of enhanced CH_4. If the plume is emitting more thermal energy than it absorbs, which is characteristic of hotter plumes, lower values of NDMI indicate a stronger likelihood of enhanced CH_4. All cases considered for this study included plumes that produced spectral

absorption features and therefore higher NDMI values were indicative of a stronger likelihood of enhanced CH_4.

For this study, two different band combinations were chosen to be compared. SB1 for each combination was MURI band 1. Centered at 7.68 μm, this band contains the strongest CH_4 absorption feature. Two different bands were chosen for SB2 for comparison, the first was MURI band 2. This band was chosen as this band contains less CH_4 absorption features than band 1 and covers a spectral region that has comparatively higher atmospheric transmission than band 1. The other band chosen for SB2 was MURI band 6. This band was chosen because CH_4 has the weakest effect on this band. After calculating the NDMI, a threshold varying from the lowest value pixel to the highest value pixel of the NDMI image was used to create ROC curves, which inform on how well the NDMI is an indicator of enhanced CH_4 presence.

3.3 Data Set Creation and Validation

This section discusses the process of creating data sets for the three studies above and the validation of the simulated data.

3.3.1 Single-pixel Simulation Validation

In order to create a realistic data set of sensor reaching radiances for these studies, a scenario in which a rogue emission source has been detected was chosen to reference in order to produce a more realistic simulated model. Data from HyTES collections are fitting for this purpose as the system's 256 spectral channels roughly cover the same region in the thermal infrared as the MURI design and collects over the CH_4 absorption feature at 7.68 μm. The chosen HyTES collection is shown in Fig. 3.1 and was recorded over Kern River oil fields on 5 February 2015 [56]. The data set provided by JPL includes a flagged image, shown in Fig. 3.1, that identifies pixels that a matched filter predicted contained enhanced CH_4 concentrations. Figure 3.3 shows typical on and off plume spectra, as well as a simulated recreation of the data using MODTRAN6. Surface level air temperature was retrieved from Weather Underground (www.wunderground.com) and was set to 293.5 K. The concentration of the plume was determined by Kuai et al to be 6 ppm [55]. A list of notable model

inputs is recorded in Table 3.2. The model was able to recreate the the HyTES spectra with a RMSE of $0.25\frac{W}{m^2 sr\mu}$ for the CH_4 present case and $0.15\frac{W}{m^2 sr\mu}$ for the background case. While these errors are relatively low, they are higher than MURI band 1's Noise Equivalent delta Radiance, which is $0.06\frac{W}{m^2 sr\mu}$. Recreation of this data provided confidence that realistic scenes could be reproduced in MODTRAN6 and helped inform the input parameters for the other simulated datasets.

TABLE 3.2: MODTRAN Parameter Settings for Validation of HyTES Simulated Radiances

Model Input	Value
Atmosphere	Midlatitude Summer
Water Vapor Scaling Factor	0.07
CH_4 Scaling Factor	0.4
Collection Height	4.572km (15000 feet)
On Plume Emitting Surface Temperature	311.5 K
Off Plume Emitting Surface Temperature	305 K
Plume Thickness	10 m
Surface Emissivity	LAMB_SANDY_LOAM
Plume Base Altitude	10 m
Ambient Temperature at Plume Altitude	293.5 K
Plume Concentration	6 ppm
Plume Temperature Difference to Ambient	-7 K

3.3.2 Matched Filter and NDMI Data Set Creation

To evaluate the multi-band methods, a simulated MURI image was created using higher spectral resolution HyTES imagery. By applying the MURI spectral response to the HyTES data, a six channel image with MURI's spectral channels was created. The synthetic MURI image was created using a subset of HyTES images recorded on July 8th, 2014, which can be seen in Figure 3.4. The chosen subset was determined to contain no detected enhanced methane pixels [56].

The images created by applying MURI's spectral response initially had less noise than the predicted noise for MURI. The noise in this image is defined as:

$$N_{simulated} = \frac{N_{HyTES}}{\sqrt{(\#of HyTES Bands)}} \tag{3.8}$$

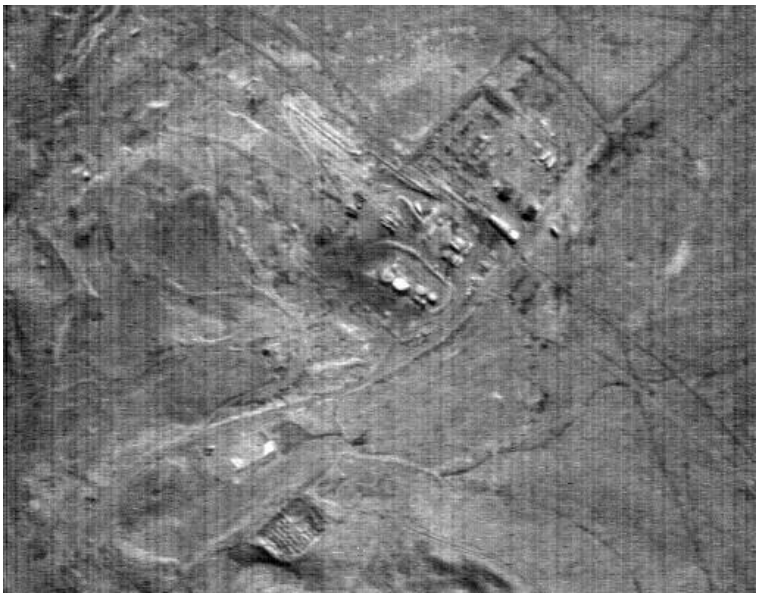

FIGURE 3.1: 7.68 μm HyTES band recorded on 5 February 2015 with a ground sample distance of 2 m This image was used to validate our model method in MODTRAN 6

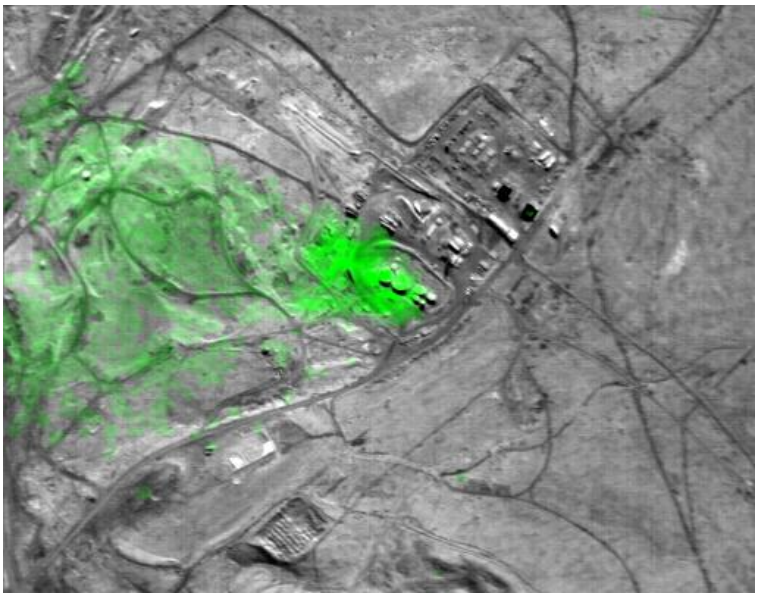

FIGURE 3.2: Flagged image, green indicates HyTES clutter matched filter has detected methane in that pixel.

This means that additional noise needed to be simulated in the image in order to better estimate a MURI image. The amount of additional noise can be defined as:

$$N_{add} = sqrt(N_{MURI}^2 - (\frac{N_{HyTESimage}}{\sqrt{(\#ofHyTESBands)}})^2) \tag{3.9}$$

This additional noise was calculated from the Noise Equivalent delta Temperature by first calculating Noise Equivalent delta Radiance:

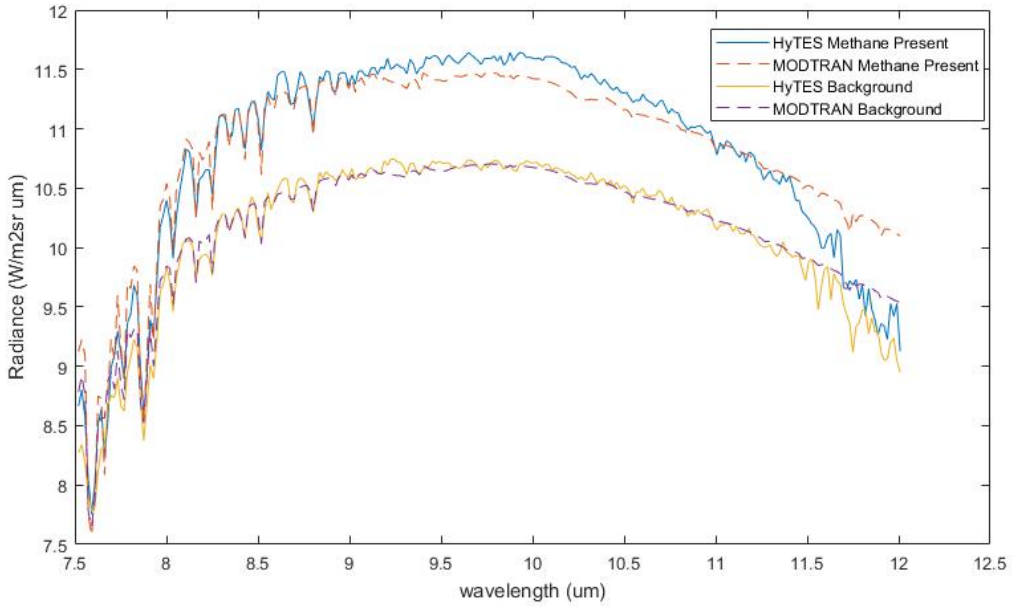

FIGURE 3.3: Recreation of HyTES spectra from data set used by Kuai et al. using MODTRAN 6. This is the recreation of one on plume and one off plume pixel.

$$NEdL = NEdT * \frac{dB}{dT} \tag{3.10}$$

Where $\frac{dB}{dT}$ is the derivative of Planck's Blackbody function with respect to temperature. The noise was then added to the image by multiplying the difference in quadrature of the NEdLs with a Gaussian random number with mean 0 and standard deviation of 1.

The simulated dataset was created to determine the ability of MURI to detect higher concentration CH_4 plumes. The data set for this investigation required an image with realistic variation and a known presence of CH_4. In order to accomplish this, a set of CH_4 present HyTES images were created. These images were created using the local chemical plume model of MODTRAN6, which outputs an on plume and off plume curve for at sensor radiance[13]. Both the off plume and on plume simulations were run with a limited atmosphere with only small amounts of CO_2. The off plume simulation contained only background levels of CH_4 while the on plume model contained an enhanced concentration plume, ranging from 1-20 ppm above ambient methane. Then a radiance difference was calculated between the

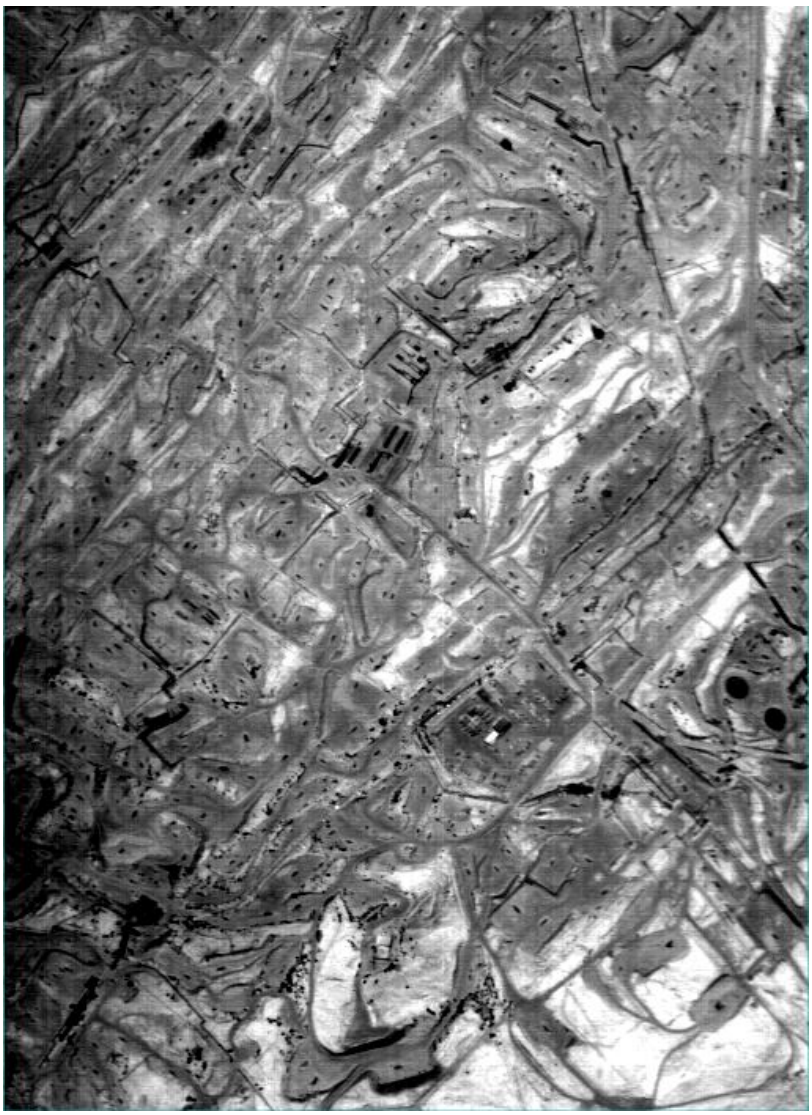

FIGURE 3.4: Single band view of HyTES image subset from July 8th, 2014. This subset was used to produce the simulated dataset.

off plume and on plume spectral curves, removing the effects of the small amount of CO_2 and background CH_4 levels. The differences were then added to copies of the background HyTES image to create a set of plume present images with realistic background variation and known methane quantity. The MURI images were then created by applying MURI's spectral response to the HyTES dataset. Additional noise was added to the images by the same method stated above. The final dataset consists of five images derived from the scene depicted in Figure 4. The first image has no enhanced levels of methane present, and the rest of the images have only enhanced levels of methane present across the entire image. Each image has a plume of constant concentration ranging from 1-20 ppm and plume temperature difference of -10 K from ambient atmospheric temperature. This also provides a simple truth map, as a perfect accuracy method would indicate the background image as having no methane present pixels (0 false alarms) and the plume present images as having every pixel be indicated as plume present (hit rate of 1).

3.4 Methane Detection Results

This section presents the results of applying each of the three methods for methane detection described above.

3.4.1 Single Pixel NEdT Study Results

TABLE 3.3: NEdT Single Pixel Study MODTRAN Parameter Settings

Constant	Value
Atmosphere	Midlatitude Summer
Water Vapor Scaling Factor	0.10
Collection Height	4.572km (15000 feet)
Emitting Surface Temperature	328 K
Plume Thickness	20 m
Surface Emissivity	LAMB_SANDY_LOAM
Plume Base Altitude	10 m
Ambient Temperature at Plume Altitude	311 K

For this study, a low altitude plume is considered. Spectral radiances in the CH_4 band were simulated using MODTRAN6, as described in section 3. Table 3.3 contains a list of notable constants and their values which were derived from examining HyTES images, metadata, and the conditions under which the images were recorded [56]. Ambient atmospheric temperature was estimated from Weather Underground which was recorded by the Meadows Field Station in Bakersfield, California on July 8th, 2014 at 11:54 am. Modern estimates of ambient atmospheric CH_4 concentration are at about 1.8 ppm [77], while the lower explosive limit is around 50,000 ppm [15]. For this experiment the CH_4 concentration within the plume was varied from 1 ppm to 50 ppm or 0.1% of the lower explosive limit. The plume temperature was defined by a temperature difference to ambient temperature. The plume for this study varied from - 10 K to +10 K of ambient temperature at the plume height. This is a range of -27 to -7 K to the background surface. Brightness temperature differences between the plume present and background cases were calculated. These differences were compared to the NEdT computed by DRS, which is 0.256 K for band one, or the CH_4 feature band. The results of the low altitude plume model can be seen in Fig. 3.5.

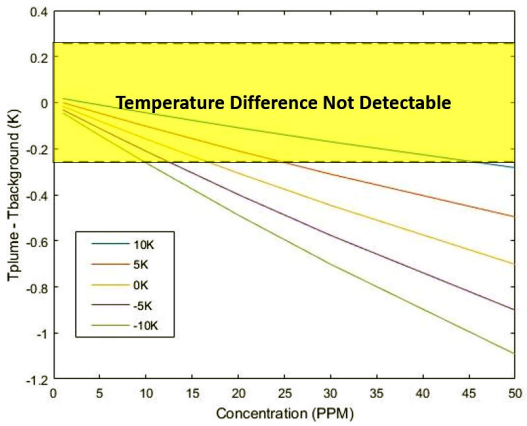

FIGURE 3.5: Low altitude plume model results displaying brightness temperature difference as a function of plume concentration. Figure identifies detectable and undetectable scenarios for MURI's predicted NEdT.

The results here indicate that a plume with a temperature difference as high as +10 K to ambient temperature is absorbing energy, which is consistent with knowledge that the background surface temperature is 17 K higher than the ambient atmospheric temperature. The higher temperature plumes require higher concentrations

to detect, with the hottest in this study requiring more than 45 ppm plume to provide a detectable contrast (about 25 times background levels). At ambient temperature, a plume of about 17 ppm (about 10 times background levels) is required for the temperature difference to have a detectable contrast, and for the coldest plume temperature a concentration of 10 ppm creates a high enough temperature difference to display a detectable contrast. This study gives a baseline for detection for a single band allocated to CH_4 absorption features.

3.4.2 Detection Using Matched Filter

For the purposes of this study, a low temperature plume (-10 K to ambient atmospheric temperature, or -27.6 K from background surface temperature) with various concentrations of CH_4 were simulated in the column and added to the background image containing only background levels of CH_4. Table 3.4 contains a list of notable constants and their values. Ambient atmospheric temperature was retrieved from Weather Underground which was the daily high temperature recorded by the Meadows Field Station in Bakersfield, California on July 8th, 2014. Surface temperature was determined by matching a blackbody to a selection of random pixels from the HyTES imagery. The signal, b in equation 5, was defined as an absorbing CH_4 plume and was extracted from the HITRAN dataset [39][40]. The ROC curves in Fig. 3.6 provide an understanding of how well the system distinguishes CH_4 present pixels and background clutter using a the matched filter approach. The probability of false alarm (P_{fa}) indicates the fraction of background clutter pixels incorrectly categorized as CH_4 present pixels, while the hit probability (P_{hit}) indicates the fraction of pixels correctly identified as CH_4 present pixels. In the perfect detection case, an ideal circumstance, there exists a threshold value where P_{hit} is 1 and P_{fa} is zero. A straight line with a slope of 1 indicates that the detection scheme is performing as well as chance. Otherwise, a high hit rate and low false alarm rate indicate a reliably detectable scenario.

Utilizing the matched filter approach shows HyTES is capable of detecting CH_4 plumes as low as 5ppm with a low false alarm rate. The hyperspectral system is even capable of detecting an additional plume of 1 ppm above background levels with a hit rate of 70% and a false alarm rate of 30%. MURI's matched filter approach shows

TABLE 3.4: Matched Filter and NDMI Dataset MODTRAN Simulation Parameter Settings

Constant	Value
Atmosphere	Midlatitude Summer
Water Vapor Scaling Factor	0.10
Collection Height	4.572km (15000 feet)
Emitting Surface Temperature	333 K
Plume Thickness	20 m
Surface Emissivity	LAMB_SANDY_LOAM
Plume Base Altitude	10 m
Ambient Temperature at Plume Altitude	315.4 K

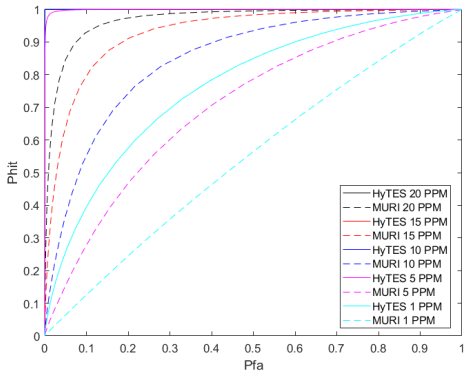

FIGURE 3.6: ROC curves for matched filter detection experiment. Results indicate high detection for most HyTES cases. Performance for MURI is high for 15 and 20 ppm, but low for 1 to 5 ppm.

that an additional plume of 10 ppm can be detected with 80% accuracy and about 24% false alarm rate. Utilizing the matched filter on the two systems reveals that the narrow band hyperspectral system is outperforming the broader band multispectral system.

3.4.3 NDMI Detection Results

The result of applying the normalized differential methane index method for MURI data simulated from HyTES imagery and MODTRAN6 can be seen in Fig. 3.7 and Fig. 3.8.

The results indicate the MURI system performs better using the NDMI using bands 1 and 6 than bands 1 and 2. The NDMI method performed on MURI band 1 and 6 performs as well as the matched filter approach being applied to all MURI

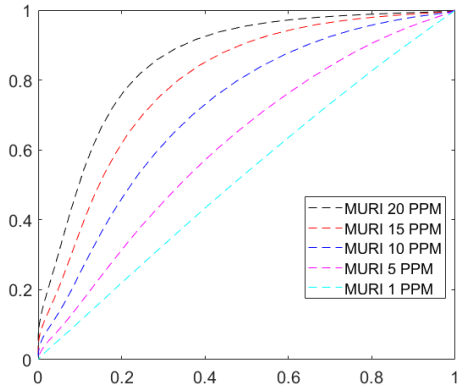

FIGURE 3.7: ROC curve describing the performance of applying the NDMI to the simulated data set using the methane feature band, band 1, and a relatively more transparent band, band 2.

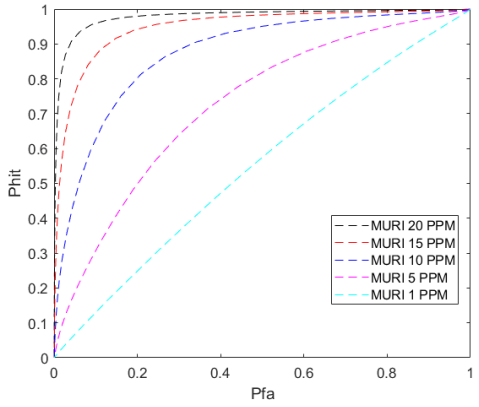

FIGURE 3.8: ROC curve describing the performance of applying the NDMI to the simulated data set using the methane feature band, band 1, and the MURI band with the least powerful methane signature, band 6.

bands, as the NDMI method shows 80% accuracy and about 20% false alarm rate for a scenario with an enhanced CH_4 plume of 10ppm. This provides evidence indicating that given a high enough concentration and temperature contrast, a simple two band approach can be used to detect enhanced levels of atmospheric CH_4 with similar accuracy to a six band approach.

3.5 Conclusions

The studies detailed here predict the ability of an uncooled microbolometer imager to detect enhanced levels of atmospheric CH_4. The single band investigation confirmed that CH_4 plumes with large concentrations and temperature differences compared to background surface temperature lead to detectable contrasts, indicating that detection with a single pixel is possible, given the proper conditions. If a CH_4 plume was large enough to be captured by multiple pixels, detection of plumes with smaller temperature differences and CH_4 concentrations could be possible by averaging over the pixels that collect plume signals. Future work includes examining additional scenarios, including different surface types and atmospheric parameters as well as validation of these results with the MURI system.

Application of the matched filter indicated the higher spectral resolution HyTES system would outperform the multispectral MURI instrument. This study also shows that the NDMI approach provides detection similar to the Matched Filter using the multispectral MURI system. Given a significant quantity and temperature differential of CH_4, the NDMI performs well enough to be useful for a thermal imager with a single channel allocated for CH_4 detection and a second band in a region with little overlap with a CH_4 absorption feature. The results also indicate that the NDMI should be defined using one band that records in a region with a CH_4 absorption feature and a broad channel that records in a region with no CH_4 specific spectral features. Future investigations aim to validate the results of these studies with images collected from test flights of the MURI system.

3.6 Supplemental Materials

This section includes supplemental figures and tables that further describe the results of the studies presented in this chapter. Figure 3.9 describes the results from Figure 3.5 using the temperature difference between plume and the surface. Table 3.5 defines the area under MURI matched Filter ROC curves from Figure 3.6. Tables 3.6 and 3.7 describe the area under the ROC curves for Figures 3.7 and 3.8 respectively.

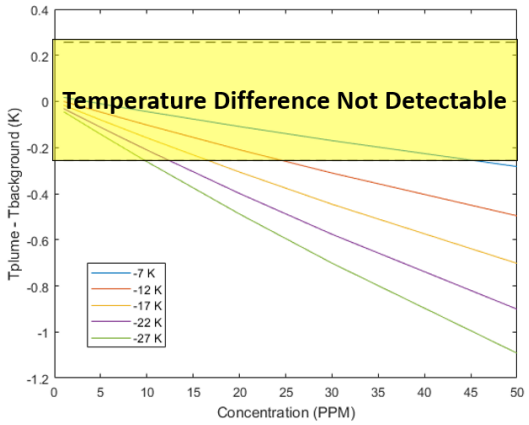

FIGURE 3.9: Recreation of Figure 5. Describes NEdT comparison study using temperature difference between the plume and the surface.

TABLE 3.5: Area Under MURI Matched Filter ROC Curves (Figure 6)

Concentration PPM #	Line Color	Area
20	Black	0.96
15	Red	0.93
10	Blue	0.84
5	Pink	0.70
1	Cyan	0.54

TABLE 3.6: Area Under MURI NDMI Band 1 and 2 ROC Curves (Figure 7)

Concentration PPM #	Line Color	Area
20	Black	0.85
15	Red	0.79
10	Blue	0.71
5	Pink	0.61
1	Cyan	0.52

TABLE 3.7: Area Under MURI NDMI Band 1 and Band 6 ROC Curves (Figure 8)

Concentration PPM #	Line Color	Area
20	Black	0.98
15	Red	0.95
10	Blue	0.87
5	Pink	0.72
1	Cyan	0.55

Chapter 4

An Evaluation of Multispectral Land Surface Temperature Retrieval Methods for Predicting Performance of the Multiband Uncooled Radiometer Imager

4.1 Introduction

This chapter will discuss two temperature retrieval algorithms which will be used to assess MURI's temperature retrieval capabilities: split window and temperature emissivity separation. Utilizing these methods will demonstrate how state of the art approaches can be applied to the novel MURI system. This chapter also includes an evaluation of MURI's spectral filters as-built using simulated data from MODTRAN6. This study was performed to determine the presence of any significant variation between the as built filters and the as specified filters that may affect the system's performance. Additionally, this chapter details a comparison study between MURI's as built filters for band 5 and 6 and the corresponding bands of Landsat 8 TIRS. Maintaining satisfactory performance in temperature retrieval using the split window approach compared to TIRS is a metric of success for MURI. Therefore, this investigation provides insight to how bands 5 and 6 of MURI differ from the TIRS bands. Finally, a discussion and preliminary results of applying

temperature retrieval techniques on DIRSIG simulated imagery is presented.

4.1.1 Land Surface Temperature and Land Surface Temperature Retrieval

Land surface temperature is one of the most significant factors and the direct driving force in the exchange of long-wave infrared radiation at interface between the surface of the Earth and the atmosphere. Accurate land surface temperature retrieval is imperative in environmental science applications such as evapotranspiration, climate change evaluation, hydrological cycle, forest fire monitoring, urban climate and environmental studies, drought evaluation, and vegetation monitoring [3][7][50][53][59][91][92][98][99]. Land surface temperature varies significantly both spatially and temporally and therefore it would be incredibly difficult to monitor any substantial area with ground based measurements. Remote sensing images provide the unique capability to monitor large sections of the Earth's surface rapidly [59]. The application of land surface temperature retrieval is particularly suitable for thermal infrared remote sensing instruments. Thermal infrared imagers record incident energy in the region of the electromagnetic radiation spectrum from 7 to 14 um. This region covers the peak emission curves for warm objects on Earth's surface, and in this region the atmosphere is highly transparent[25][41][87].

Although this region of the electromagnetic spectrum is particularly suitable for land surface temperature retrieval, the challenge of getting accurate land surface temperature estimates is not trivial. Values for at sensor radiance for Earth remote sensing imagers are directly related to land surface temperature, but are also affected by surface emissivity, reflected downwelling irradiance, and atmospheric attenuation and upwelling. Chapter 2 details the thermal contributions to sensor reaching radiance. As shown in equation 2.11, estimating land surface temperature from sensor reaching radiance requires corrections for surface emissivity and atmospheric effects. Note that for studies presented here, Path D, or energy emitted from an off target surface that is refect off the target surface and up to the sensor, is not considered. Therefore, the equation relating sensor reaching radiance to these components can be written:

$$L_{sr} = L_A + L_B + L_C \tag{4.1}$$

The complete equation is written as:

$$L_{sr} = \epsilon(\lambda)B(\lambda, T)\tau(\lambda) + L_u(\lambda) + [1 - \epsilon(\lambda)]L_d(\lambda)\tau(\lambda) \tag{4.2}$$

4.2 Temperature Retrieval Method Descriptions

In this section, a pair of multichannel land surface temperature retrieval methods will be discussed: split window and temperature emissivity separation. This section will also compare the methods. The section on split window will include a discussion on apparent/brightness temperature.

4.2.1 Split Window Algorithm for TIRS and MURI

The split window algorithm is a temperature retrieval method that has been successfully applied to remote sensing data sets such as NOAA-11 AVHRR, MODIS, and Landsat 8 TIRS [8][24][33][52][83][94]. This technique is advantageous in that it does not require atmospheric profiles of temperature or water vapor to correct for the atmosphere. The method corrects for atmospheric effects using the differential absorption between the two bands. This makes the method less sensitive to uncertainties in the transmissivity of the column than a method that relies on atmospheric transmission within the spectral range of a single bandpass. There are several variations of this method. The version of the Split Window method presented here includes a quadratic term defined by Wan 2014 and has seen successful application to Landsat TIRS data [24][33][94].

The split window algorithm is able to take as an input the brightness temperature of the two chosen thermal bands as well as emissivities of the surface within those two bands, and produce estimates for land surface temperature without additional inputs or knowledge of the atmosphere. Brightness temperature, also referred to as apparent temperature, is defined as the temperature that a blackbody emitter must be at to produce the effective at sensor reaching radiance of a particular band. Brightness temperature can be found by inverting Planck's equation for blackbody radiation. Equating the at sensor radiance to Planck's black body radiation equation:

$$L_{effective} = \frac{2hc^2}{\lambda^5} \frac{1}{e^{\frac{hc}{\lambda k T_{brightness}}} - 1} \tag{4.3}$$

where h is Planck's constant, c is the speed of light, λ is the center wavelength for each bandpass, and k is the Boltzmann constant. Rearranging the equation to solve for the temperature that would produce the bandpass specific at sensor radiance:

$$T_{brightness} = \frac{hc}{\lambda k_b \log \frac{hc}{L_{effective}\lambda}} \tag{4.4}$$

The first step in the split window is to calculate brightness temperature for the two split window bands. For Landsat, the split window bands are the two TIRS bands, for MURI the split window bands are bands 5 and 6. After calculating brightness temperature, the surface emissivity for each band must be determined, either through direct measurement or by using an emissivity database. A general form of the split window algorithm can be written:

$$LST = b_0 + (b_1 + b_2\frac{1-\epsilon}{\epsilon} + b_3\frac{\Delta\epsilon}{\epsilon^2})\frac{T_i + T_j}{2} + (b_4 + b_5\frac{1-\epsilon}{\epsilon} + b_6\frac{\Delta\epsilon}{\epsilon^2})\frac{T_i - T_j}{2} + b_7(T_i - T_j)^2 \tag{4.5}$$

T_i is the brightness temperature calculated for the first of the two channels (TIRS band 1, MURI band 5), and T_j is the brightness temperature calculated for the second of the two channels (TIRS band 2, MURI band 6). ϵ is the average emissivity between the two bands ($\frac{\epsilon_i + \epsilon_j}{2}$) and $\Delta\epsilon$ is the difference between the emissivity of the bands ($\Delta\epsilon = \epsilon_i - \epsilon_j$).

The coefficients b_{1-7} are derived using approach described in Figure 4.1. The method involves data from a combination of databases. The first is the Thermodynamic Initial Guess Retrieval (TIGR) atmospheric profiles, which is a set of world wide atmospheric situations constructed by Laboratoire de Meteorologic Dynamique. The data set contains 2311 radio soundings, 946 of which are determined to be in non-cloudy conditions[23]. The remaining scenarios, which have humidity above 90%, are not used in the derivation of the coefficients as they represent potentially saturated atmospheric conditions.

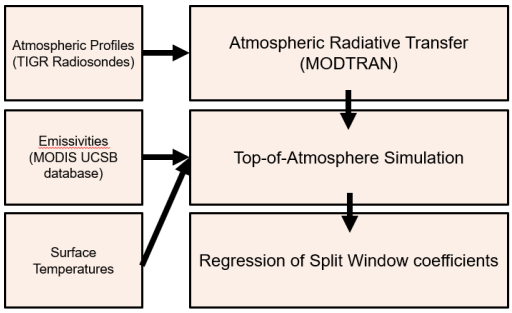

FIGURE 4.1: Flow chart describing the derivation of Split Window coefficients. TIGR radiosonde atmospheric profiles are used to inform radiative transfer models, which are used in combination with surface emissivities and temperatures to calculate brightness temperatures for the two bands. A linear regression is performed using the known surface temperatures and brightness temperatures to calculate TES coeeficients.

The surface is defined using emissivities chosen from the selection of natural surface types from the MODIS UCSB emissivity database. The training set consists of 113 unique spectral emissivities including 74 unique soil and mineral types, 28 types of vegetation, and 11 forms of water, snow, and ice [60]. The surface temperature is defined in reference to the bottom layer of the atmosphere. The temperature difference between the surface and atmospheric temperature at the bottom layer of the atmosphere range from $-20K$ to $+10K$. This is consistent with the assumption that split window is most appropriately used to retrieve surface temperatures when the surface temperature is close to ambient air temperature at the surface level [33][95].

These parameters are used to inform the radiative transfer models of MODTRAN, which produces at-sensor spectral radiance. By applying the system specific bandpasses (TIRS and MURI), band specific effect radiance values are calculated. From band specific effect radiance values, brightness temperatures are calculated for each band using an effective radiance to brightness temperature look up table [24][33].

4.2.2 Temperature Emissivity Separation

The split window technique described above has the advantage of being applied without knowledge of the atmospheric conditions under which the data was recorded, but it does not utilize all the information the MURI system is recording. In addition, the split window method relies on emissivity values being measured by an external

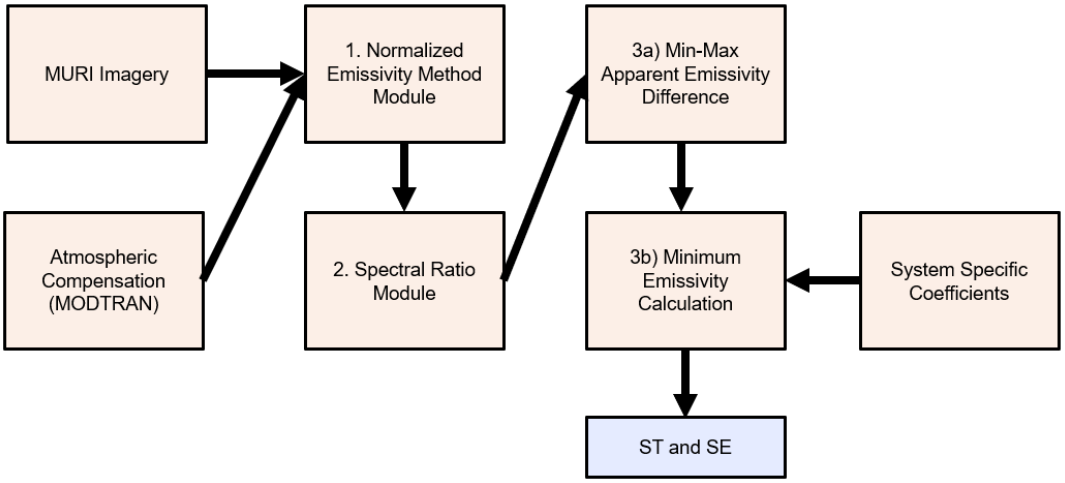

FIGURE 4.2: Flow chart describing the application of the Temperature Emissivity Separation Algorithm. Three inputs: Imagery, Atmospheric Compensation, and system specific coefficients, inform the method. The three modules, NEM, SRM, and MMD, output surface temperature and surface emissivity.

device, or from a database. To determine the extent of the MURI system's capabilities it would be best to assess its performance with a method that makes use of all of the information it records. The Temperature Emissivity Separation (TES) method is a set of modules that are used to separate land surface temperatures from emissivities using atmospherically compensated radiances.

The primary issue in attempting to determine LST and LSE from thermal infrared data is that no matter how many spectral bands are used, the system of equations will always be underdetermined–there will always be more unknowns than data points. For example, an imaging system with N bands will have N data points, but will have N+1 unknowns which includes N LSE values corresponding to each band as well as a surface temperature [51]. TES attempts to reduce the numbers of unknowns by using the relationship between spectral contrast and minimum emissivity.

An overview of this approach can be seen in Figure 4.2. The TES method is performed in three steps, referred to as modules. Before TES can be performed, the radiance values reported from the system must be corrected, or compensated, for the effects of the atmosphere. Atmospheric compensation is described in section 4.3.

The first of the three modules performed after atmospheric compensation is the

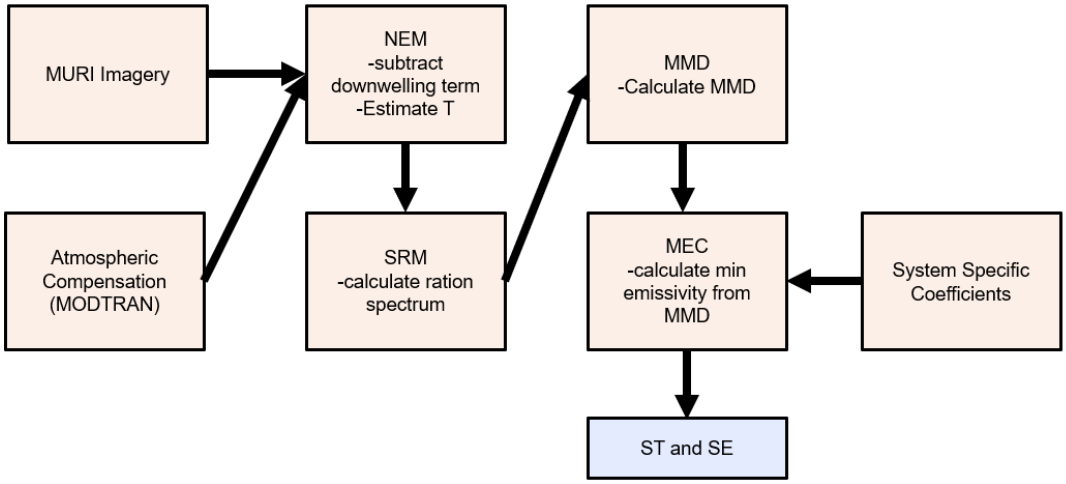

FIGURE 4.3: Flow chart describing the application of the Temperature Emissivity Separation Algorithm and detailing what process occurs in each step of the algorithm.

Normalized Emissivity Method (NEM). NEM is a simultaneous LST and LSE retrieval method that first uses the assumption of constant emissivity in all spectral channels for a single pixel. Using groundleaving radiance received through atmospheric compensation and measured downwelling radiance, land surface temperatures can be calculated for each channel using the inverse of the Planck function:

$$T_n = \frac{hc}{\lambda k_b \log \frac{hc}{\frac{L_{groundleaving} - (1-\epsilon_{constant})L_d}{\epsilon_{constant}} \lambda_{center}}} \tag{4.6}$$

where $L_{groundleaving}$ is the ground leaving radiance from the atmospherically compensated radiance data, L_d is the downwelling atmospheric radiance and $\epsilon_{constant}$ is the assumed constant emissivity value. From this set of N temperatures, the maximum temperature is chosen to serve as the LST from which the remaining normalized emissivities are derived. These emissivities are iteratively used to calculate surface temperature and radiance until the change in radiance between iterations is less than the Noise Equivalent delta Radiance (NEdL) or until the number of iterations exceeds I, which is set to 12.

After estimation of the normalized emissivites and initial surface temperature, the spectral ratio (SR) module is used to determine the ratio of the normalized emissivities to the average:

$$\beta_n = \frac{\epsilon_n}{\frac{1}{N}\sum_{n=1}^{N}\epsilon_n} \tag{4.7}$$

The spectral ratio is capable of describing the shape of the emissivity curve, rather than directly provide the emissivity value for each band. This method has been shown to be able to reproduce the shape of the emissivity curve for rough estimations of LST.

The third and final module is the Maximum-Minimum Apparent Emissivity Difference (MMD) method. This method uses the maximum and minimum emissivities calculated from the SR module to calculate the spectral contrast range:

$$MMD = max(\beta_n) - min(\beta_n) \tag{4.8}$$

The MMD can then be used to determine the minimum emissiviy, using the following relationship:

$$\epsilon_{min} = A_0 + A_1 MMD^{A_2} \tag{4.9}$$

where the coefficients A_0-A_2 are coefficients specific to the remote system with which the data were recorded. These coefficients have been calculated using laboratory reflectance spectra that have been equated to emissivities by Kirchoff's law. The process of calculating these coefficients begins with estimating radiances of a black body of temperature 300 K. Emissivities are applied to the radiances and the β spectra followed by the MMD are calculted. The minimum in-band emissivity, calculated by applying the system's spectral response to the sample emissivity curves, is then regressed the calculated MMD values. While the coefficients are calculated empirically, these coefficients are not dependent on surface temperature.

After calculating the minimum emissivity, the spectral ratio can be used to calculate the emissivities of the remaining bands. After calculating the surface emissivities, calculating surface temperature is a matter of resolving equation 4.6 using the new value for emissivity of the band with the maximum emissivity [35][36][86].

The temperature emissivity separation approach has the advantage of utilizing five of MURI's bands and not relying on emissivity values from a database. (Note,

MURI band 1 was excluded from this study, as the constructed MURI band 1 imagery had low contrast, likely being dominated by water absorption features in that region. Additionally, this made working with unregistered band 1 data difficult).However, this method is heavily reliant on accurate atmospheric compensation and downwelling measurements. This method has seen success with data collected from other multispectral imaging systems such as the Advanced Spaceborne Thermal Emission and Reflection Radiometer (ASTER) [35],[36],[34], the Spinning Enhanced Visible and InfraRed Imager (SEVIRI) [65], and a variation of this method is currently in use for data recorded by the ECOsystem Spaceborne Thermal Radiometer Experiment on Space Station (ECOSTRESS)[46][82][48]. Previous success of this method makes its application a valuable assessment of MURI's temperature and emissivity retrieval capabilities.

4.3 Atmospheric Compensation using MODTRAN4

Land surface temperature and emissivity retrieval using TES requires accurate atmospheric compensation. Compensation is required to quantify and remove the effects of the atmospheric contributions to sensor reaching radiance. The equation that describes the contributions to sensor reaching radiance is:

$$L_{sr} = \epsilon(\lambda)B(\lambda, T)\tau(\lambda) + L_u(\lambda) + [1 - \epsilon(\lambda)]L_d(\lambda)\tau(\lambda) \tag{4.10}$$

In order to compensate for the atmosphere, values for atmospheric transmission (τ), upwelling (L_{up}), and downwelling radiance (L_d) must be measured or calculated. The method must effectively compensate for path B and C and the atmospheric transmission term in Path A of equation 4.2. For this study, a simulated approach was chosen and values for atmospheric transmission, upwelling, and downwelling radiance were simulated using MODTRAN4. The modeling code includes an option to simulate radiances with a user defined atmosphere, allowing for scene specific atmospheric compensation to be performed [11][12]. Simulations were performed for each scene and included atmospheres specific to the day, time, and location of the targets. The atmospheric data for each simulation was retrieved from

the Global Modeling and Assimilation Office's (GMAO) Goddard Earth Observing Satellite Forward Processing (GEOS-FP) data set. The forecast from the GEOS-FP dataset provides values for atmospheric temperature, pressure, and water content [22][64]. The dataset has a spatial resolution of 0.25 degrees latitude and 0.3125 longitudes. For each target location used in the test flights, data from the four closest GEOS-FP points were taken. Then a spatial interpolation is performed to predict the atmosphere at the latitude and longitude of interest. The dataset has a temporal resolution of three hours, therefore a temporal interpolation was also required.

4.4 Evaluation of Real Filter Samples via Brightness Temperature Comparison to As Specified Samples

This section presents a study performed to determine the effect of the difference between MURI's spectral bands as specified by DRS and the transmission of the filters constructed for the MURI instrument. This evaluation was imperative for predicting if the constructed band passes would be capable of performance within an acceptable degree of error to the bands as specified. A selection of filter transmission curves were provided by the manufacturer for each band, save for band one, which only a single filter transmission curve was created. The metric for evaluation of all six bands was the minimum detectable temperature difference provided by DRS Technologies. This section discusses an additional metric for band one, which includes comparing the levels of methane detectable by the constructed filter to the proposed filters.

4.4.1 Description of Bandpass Comparison Study

In order to test the performance of the constructed filters against the theoretical filters, a high spectral resolution at sensor radiance dataset was constructed using MODTRAN 6. These simulated at sensor radiances were created using a Midlatitude summer atmosphere. Varying water vapor concentrations were acheived by scaling the midlatitude summer default value, and two different ground surface temperatures were used. A user defined temperature profile was also entered with the lower layers in the profile being replaced by higher temperatures more common in the

southwestern United States in the summer, where test flights were held. The simulated at sensor radiance values then had both the theoretical and constructed filter functions applied, creating a simulated single pixel for both the proposed and constructed MURI instrument. Figure 4.4 displays the theoretical system with a sample of a filter for each band pass, and Table 4.1 displays key parameters for the MODTRAN simulation.

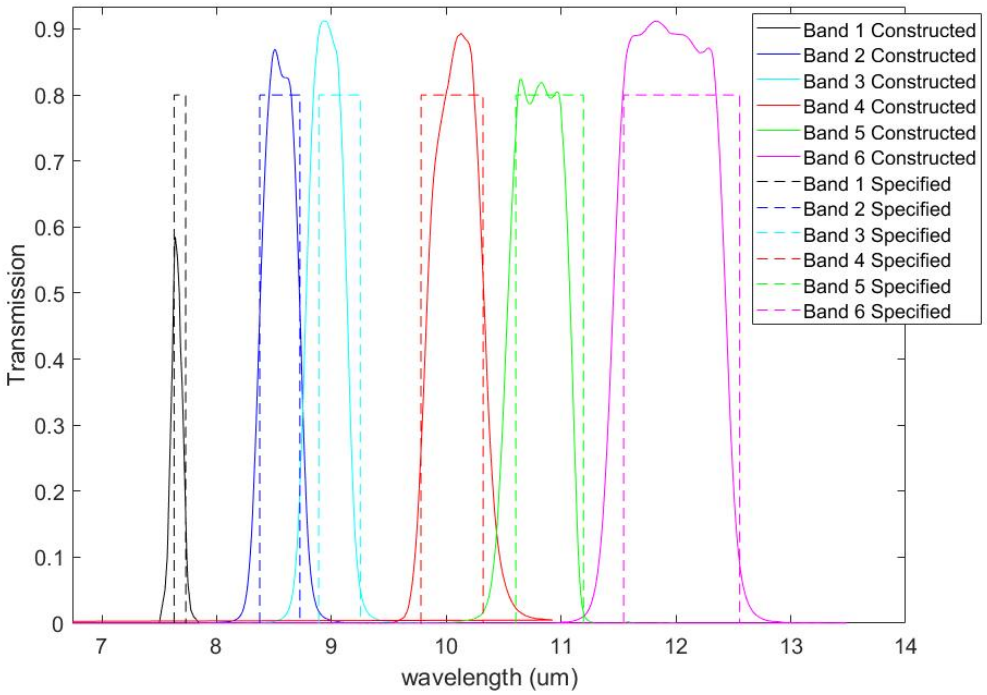

FIGURE 4.4: A comparison plot of the theoretical MURI band filters and a sample of the constructed filters

TABLE 4.1: MODTRAN parameters for creating at sensor radiances for comparing MURI's constructed bands to theoretical MURI bands.

Parameter	Value
Atmosphere	midlatitude summer
Water Vapor Scaling Factor	0.1, 0.5, 1.0
Collection Height	4.572km (15000 feet)
Surface Temperature	270, 320 K
Surface Emission	LAMB_SANDY_LOAM

One metric of comparison for this study was the effective radiance of each band. Effective radiance can be described as the radiance the system senses. It can be

defined as the radiance a system is responsive to normalized by the responsivity curve of the system:

$$L_{eff} = \frac{\int_{\lambda_a}^{\lambda_b} L_{atsensor} R, d\lambda}{\int_{\lambda_a}^{\lambda_b} R, d\lambda} \tag{4.11}$$

where R is the responsivity of the bandpass, or in this case the filter functions, and λ_a and λ_b are the wavelength limits. The second metric used to determine performance was the Noise Equivalent delta Temperature, or the minimum detectable temperature difference for the system. Values for brightness temperature were calculated using the effective radiance for each set of simulated and constructed filter pairs. The difference between the brightness temperatures was then compared to the NEdT to determine if the temperature difference caused by the difference in the filter functions. Values for NEdT were provided by DRS.

Finally, in order to predict MURI's performance compared to TIRS, the spectral response of TIRS was used to determine brightness temperatures for each of the at sensor radiances produced by the MODTRAN radiative transfer models. These brightness temperatures were differenced with MURI's brightness temperatures for band 5 and 6, and compared to MURI's NEdT to determine if the difference was detectable by the MURI system.

4.4.2 Filter Transmission Examination Using Effective Radiance and NEdT

Figures 4.5 and 4.6 show the effective radiance comparisons for the 270 and 320 K surface temperatures respectively. Each figure shows three different scalings of the column water vapor for both the theoretical and constructed MURI band passes. Figure 4.5 shows that as the column water vapor rises, the difference in effective radiance increases between the constructed and theoretical bandpasses, especially for band one. At the highest water vapor content, the difference between the effective radiance of the theoretical to the constructed is a decrease in radiance of around 14%, compared to the decrease in effect radiance of only 7% for the lowest column water vapor content. The second largest change in effective radiance is noted to be for band 6, which at the highest water vapor content actually experiences an increase in effect radiance of approximately 2%, while the lowest water vapor content experiences an

increase of about 1.5%. These results follow what is logically expected to be true, as the constructed band 1 has been shifted to lower wavelengths, and now overlaps more with a set of water absorption lines just below 7.6 um. The shift towards lower wavelengths also shifts the bandpass to a spot that is lower on the Planck curve for blackbody radiation at normal Earth surface temperatures. The small increase in radiance for band 6 can also be accounted for by shifting to a position that is higher on Planck's curve for blackbody radiation. It is also clear from the variation in band 1 that column water vapor scaling has a significant effect on the constructed band.

Figure 4.6 provides further evidence to support the bands' sensitivity to water vapor and temperature. At a surface temperature of 270 K, the differences in effective radiance between constructed and proposed band 6 shrinks for all cases. For band 1, the higher the water content, the greater the difference between the effective radiance values of the proposed and constructed bands, indicating the shift to lower wavelengths for the constructed band overlaps with a collection of water absorption lines.

Table 4.2 describes the NEdT for each band and the temperature differences derived from the effective radiance values from Figures 4.5 and 4.6.

TABLE 4.2: Constructed vs As Specified bandpass temperature differences for different scalings of Midlatitutde summer atmospheric column water vapor. * represents a temperature difference greater than the NEdT.

Band Number	Temperature(K)	NEdT @ 300 K(K)	10% CWV(K)	50% CWV(K)	100% CWV(K)
Band 1	320	0.332	-3.27*	-6.37*	-6.29*
	270		-0.97*	-3.25*	-4.25*
Band 2	320	0.096	0.01	0.10*	0.17*
	270		-0.06	-0.14*	-0.16*
Band 3	320	0.096	-0.08	-0.33*	-0.47*
	270		-0.55*	-0.42*	-0.37*
Band 4	320	0.070	-0.08*	-0.04	-0.02
	270		-0.02	-0.06	-0.05
Band 5	320	0.071	0.39*	0.32*	0.34*
	270		0.19*	0.23*	0.16*
Band 6	320	0.041	1.22*	1.60*	1.79*
	270		-0.03	-0.19*	-0.12*

The results here indicate that the brightness temperature differences in the constructed vs proposed bandpasses is higher than the NEdT of the system, demonstrating the difference is above the noise floor and therefore the system is sensitive

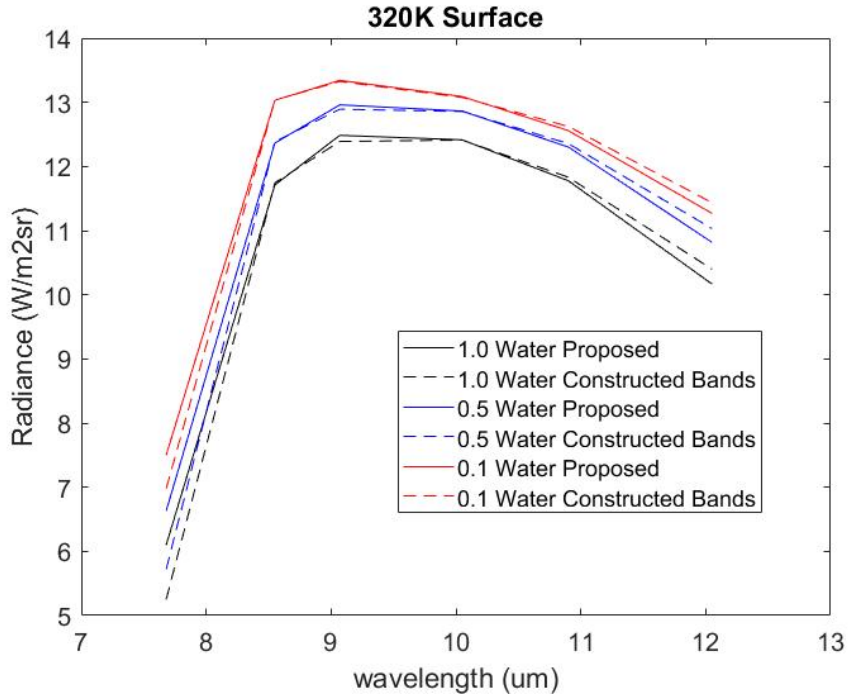

FIGURE 4.5: Effective radiance values calculated for constructed vs proposed MURI bands over a 320 K surface in a Midlatitute Summer atmosphere.

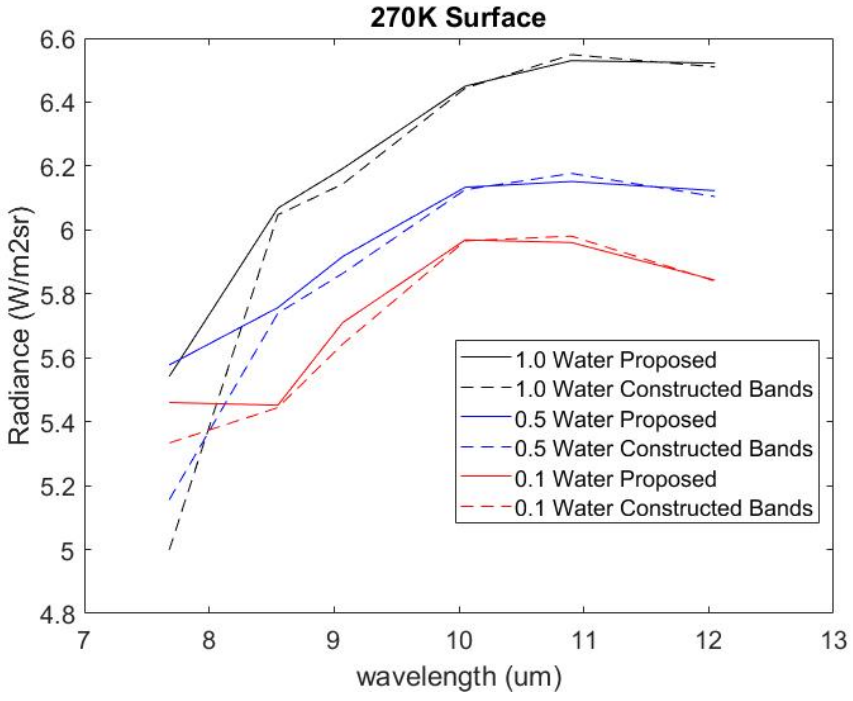

FIGURE 4.6: Effective radiance values calculated for constructed vs proposed MURI bands over a 270 K surface in a Midlatitute Summer atmosphere.

enough to detect it. Most of the differences are very low, in most cases within one order of magnitude of the NEdT. The most drastic change is seen in band 1. This band

is the narrowest band, but it is also located near a collection of methane absorption lines and water absorption lines [39]. As described above, the shifting of the band towards the water feature means the band is much more sensitive to changes in the water content in the atmosphere. Band 6 is shown once again to be mostly affected by the surface temperature difference, while it is less sensitive to changes in the water content.

The shifting of the constructed bands requires defining new band centers for the purpose of determining more accurate brightness temperatures. The new band centers are defined by finding the center wavelength between the half max points used to determine the full width half max value. Table 4.3 describes the temperature differences if the new band centers are considered for the constructed bands in place of the original theoretical band centers.

TABLE 4.3: Considering the shifted band centers, Constructed vs As Specified bandpass temperature differences for different scalings of Midlatitutde summer atmospheric column water vapor. * represents a temperature difference greater than the NEdT.

Band Number	Temperature(K)	NEdT @ 300 K(K)	10% CWV(K)	50% CWV(K)	100% CWV(K)
Band 1	320	0.332	-2.99*	-6.07*	-5.99*
	270		-0.67*	-2.95*	-3.94*
Band 2	320	0.096	-0.00	0.09	0.15*
	270		-0.09	-0.17*	-0.18*
Band 3	320	0.096	-0.04	-0.26*	-0.37*
	270		-0.01	0.10*	0.12*
Band 4	320	0.070	0.05	0.09*	0.09*
	270		-0.09*	-0.12*	-0.10*
Band 5	320	0.071	-0.18*	-0.23*	-0.17*
	270		0.15*	0.17*	0.08*
Band 6	320	0.041	0.31*	0.73*	0.98*
	270		-0.34*	-0.53*	-0.50*

For most cases, the shifting of the band center for the calculations lowers the temperature difference, which makes sense, as shifting the band center would lead to more accurate brightness temperature results. Although many of the cases have the same result, a brightness temperature difference that is detectable by the system, the shifting of the band center leads to more detectable brightness temperature differences. Once again, the same patterns emerge: band 1 is sensitive to changes in the water content and surface temperature. Examining the constructed bands using these two methods provides an idea of how band shifting effects the radiance

and brightness temperature values and helps to describe how identifying new band centers will effect brightness temperature calculations.

The values shown in the tables above, while some may be above the NEdT for their bandpass, are not particularly alarming. As discussed previously, both the split window technique and TES rely on the calculation of sensor specific coefficients to perform LST retrieval. However, the effect of water concentration on constructed MURI band 1 may interfere with methane detection.

4.4.3 Comparison of Constructed Bands to TIRS

A metric of success for the MURI system is maintaining satisfactory performance in the thermal infrared in comparison to Landsat 8 TIRS. Band 5 and 6 are designed to match Landsat 8's TIRs bands. Just as above, the brightness temperature difference is used to evaluate the difference between the two sets of bandpass. Results comparing the as built band 5 and 6, including the shifted band centers, to Landsat 8 TIRS are reported in Table 4.4.

TABLE 4.4: Constructed MURI band 5 and 6 vs TIRS temperature differences for different scaling of Midlatitutde summer atmospheric column water vapor. * represents a temperature difference greater than MURI's NEdT.

Band Number	Temperature	NEdT @ 300 K	10% CWV	50% CWV	100% CWV
Band 5	320	0.071	0.45*	0.52*	0.54*
	270		0.16*	0.09*	0.0046
Band 6	320	0.041	0.71*	0.89*	0.97*
	270		0.02	-0.06*	-0.04

The results indicate that many of the scenarios lead to detectable brightness temperatures and in all scenarios the difference is less than a Kelvin. There is some water vapor concentration dependency, but the brightness temperature difference in both bands appears to more dependent on the surface temperature. While the differences appear to be significant enough to be detectable, the chosen temperature retrieval methods rely upon coefficients derived specifically for each system. The studies presented below will show that the chosen temperature retrieval methods will maintain adequate performance in retrieving LST despite the differences in the bandpasses of MURI and TIRS.

4.5 Applying Temperature Retrieval Approaches to Simulated DIRSIG Imagery

This section will describe the application of the Split Window technique using both MURI and TIRS to simulated data. This section will also discuss the creation of a simulated dataset using MODTRAN6 and the application of TES to that dataset.

4.5.1 DIRSIG Simulated Scene

In preparation for test flights over Los Alamitos Joint Training Base performed in Fall of 2019, a simulated image was created using the Digital Imaging and Remote Sensing Image Generation (DIRSIG) model[37]. This physics based model, designed by the Digital Imaging and Remote Sensing lab at the Rochester Institute of Technology, allows for the simulation of single channel, multi, and hyperspectral imagery from the visible to the thermal infrared regions of the electromagnetic spectrum.

The simulated scene[1] consists of a selection of surfaces of constant emisivities at 4 distinct temperatures and can be seen in Figure 4.7. Initial examinations were performed on the second row of surfaces, which was chosen because it is the only surface with an emissivity of less than 1. However, during examination it was revealed that the emissivity of the surfaces was not constant, causing higher variation in radiances the higher the temperature, and therefore could not provide a way to accurately determine how well the method was performing. Instead the bottom row of surfaces, which have an emissivity of 1, was chosen for the study.

The image has a higher spectral resolution than MURI and TIRS (300 spectral bands in comparison to 6 and 2 respectively), so in order to simulate a data set for MURI and TIRS, the spectral responses for each system was separately applied to the image. The scene does not include any sensor noise, therefore, system specific noise was added to the imagery for each data set. The result is two images: a six channel image with additional noise characteristic of the MURI system and a two channel image with additional noise corresponding to the TIRS system. The scene has also been provided without knowledge of the simulated atmosphere, which does not

[1] DIRSIG scene was constructed by Rolondo Raqueño of University of Rochester

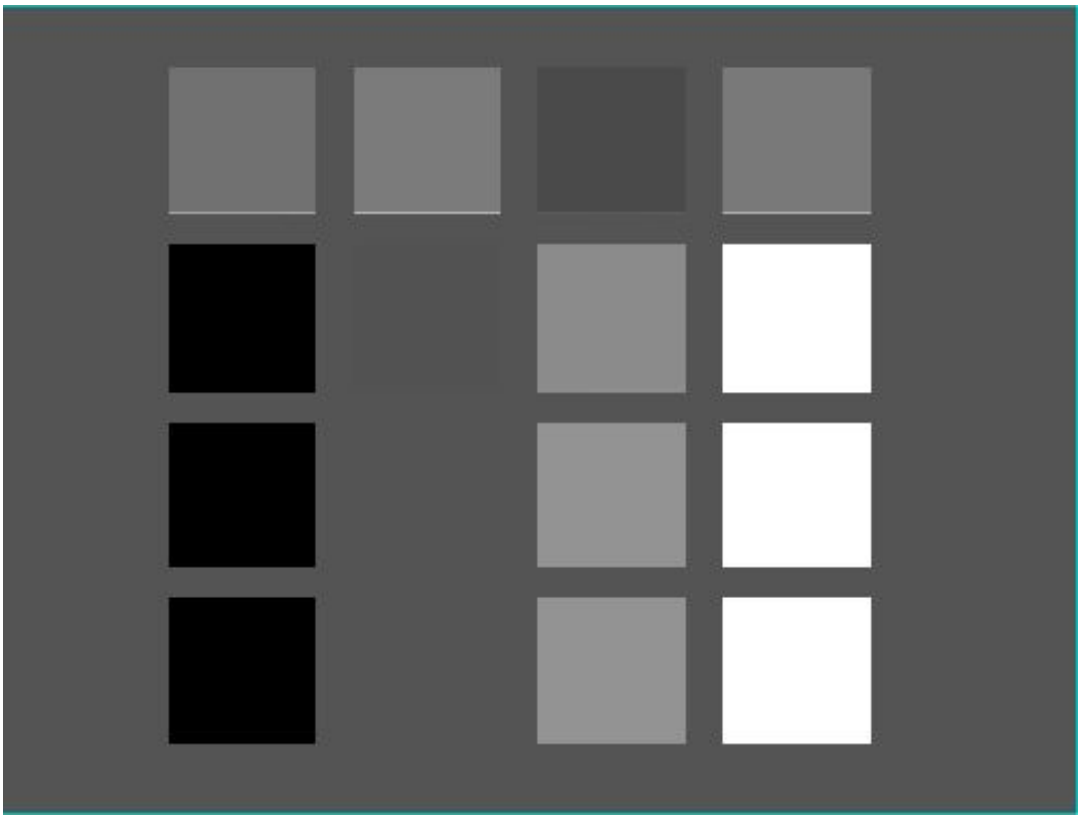

FIGURE 4.7: DIRSIG demo scene to be used for initial testing of the split window technique for MURI and comparison to TIRS.

matter as the split window technique's LST retrieval is independent of the atmospheric conditions under which an image is recorded.

4.5.2 Application of Split Window on DIRSIG Scene

The split window coefficients were calculated for both MURI and TIRS by Dr. Tania Kleynhans, associate scientist for the Chester F. Carlson Center for Imaging Science at Rochester Institute of Technology. The coefficients were calculated for a height of 705 km, the height of the Landsat satellite from Earth and the distance the satellite version of MURI will be from the Earth's surface. Coefficients for MURI at 4.572 km were derived before the testflights scheduled at the end of August 2019, however, the actual testflights were performed at 3.353 km. The use of the satellite based coefficients demonstrates that application of the split window is possible for the MURI system.

Table 4.5 details the results for applying the split window for temperature retrieval for both the MURI and TIRS system. The results are presented in the form of

mean LST retrieved across the surface and root mean squared error (RMSE).

TABLE 4.5: Results of applying split window technique to surfaces from the DIRSIG demonstration thermal scene.

	Surface 1	Surface 2	Surface 3	Surface 4
Temperature (K)	350	320	300	250
Emissivity	1	1	1	1
MURI Mean (K)	348.15	319.07	299.6847	251.17
MURI RMSE (K)	1.85	0.95	0.38	1.23 K
TIRS Mean (K)	349.74	320.05 K	300.18	250.83
TIRS RMSE (K)	0.60	0.96	1.12	1.98

The results above demonstrate that the split window technique applied to simulated MURI dataset performs comparatively to TIRS. In the 300 - 320 K range, both systems are capable of retrieving temperatures across the pixel with about a Kelvin or less of RMSE. Even estimating temperatures within 2 K is promising, yet it is notable that the MURI split window performs considerably less well on the highest surface temperatures, while TIRS maintains a low RMSE. One drawback of having only blackbodies (emissivities of 1) is that this scenario does not test the full split window equation. When performing this examination with a blackbody, the parts of the equation that depend on emissivity difference between the bands disappear. Equation 4.5 becomes:

$$LST = b_0 + (b_1)\frac{T_i + T_j}{2} + (b_4)\frac{T_i - T_j}{2} + b_7(T_i - T_j)^2 \tag{4.12}$$

meaning an equation that relies on eight coefficients is reduced to an equation with only four. While this study demonstrates the systems capability to retrieve temperatures from a blackbody, it would be best to be able to test the full equation. None of the surfaces from Figure 4.5 are defined as having wavelength dependent emissivity values, so there is no way to evaluate a surface using the entire split window equation using this image.

4.5.3 TES Application to MODTRAN dataset

A simulated MURI dataset with known emissivity, temperature, and atmosphere was created to test the implementation of the TES algorithm. The dataset consists

of 4 surfaces of known emissivity: Constant Emissivity (0.9), Sea Water, Igneous Rock, and Distilled Water. The three surfaces without constant emissivity have their emissivities defined using the ECOSTRESS spectral library (formerly known as the ASTER/MODIS spectral library) [5][62]. Surface radiance is calculated by applying the surface emissivity to the radiance value provided Planck's black body function.

The MODTRAN simulation was informed by GEOS-FP data from October 4th of 2019 [22][64]. This simulation was used in characterizing MURI's temperature retrieval capabilities and radiometric error in Chapter 6, and is therefore accepted as a good representation of realistic scene. Atmospheric transmission, downwelling, and upwelling were used to calculate at sensor radiance at a high spectral resolution, then MURI's spectral resolution is applied.

Simulated noise was added to the data to better represent MURI data. This additional noise was calculated from MURI's predicted Noise Equivalent delta Temperature by first calculating Noise Equivalent delta Radiance:

$$NEdL = NEdT * \frac{dB}{dT} \tag{4.13}$$

Where $\frac{dB}{dT}$ is the derivative of Planck's Blackbody function with respect to temperature. The noise was then added to the image by multiplying the NEdLs with a Gaussian random number with mean 0 and standard deviation of 1.

The result is 4 simulated MURI samples of known atmosphere and surface temperature. The atmospheric compensation approach is applied; note this is the ideal case where the exact atmosphere is known. The MMD coefficients calculated for this were derived using a subset of 53 samples from the ECOSTRESS spectral library [5][62] [2]. This subset is the same subset used to train the TES algorithm used by ECOSTRESS and is most representative of naturally occurring geologic endmembers you would observe at remote sensing scales of about 100 m. In addition to each of the samples, each sample is adjusted by a vegetation fraction of 25%, 50%, and 75% using the conifer samples in the collection. This way, the coefficients are trained on a dataset that includes representations of mixed pixels.

[2]subset provided by Dr. Glynn Hulley of the Carbon Cycle and Ecosystems group at the Jet Propulsion Laboratory.

TABLE 4.6: Results of applying TES algorithm to simulated dataset

Variable	RMSE	RMSE %
Temperature	0.74 K	0.25
Band 2 ϵ	0.01	1.41
Band 3 ϵ	0.01	1.05
Band 4 ϵ	0.01	0.79
Band 5 ϵ	0.01	1.29
Band 6 ϵ	0.02	1.62

The results of applying the TES algorithm to the simulated dataset are shown in Table 4.6. The results indicate that, given an ideal atmospheric compensation, we can expect temperature retrievals within a percent of the surface temperature. RMSE of emissivity retrievals are within 2% of the surface emissivity. This examination predicts that the TES approach is viable for temperature and emissivity retrieval for MURI.

Chapter 5

Assessment of a Novel Methane Detection Method

5.1 Introduction

5.1.1 Context for Investigation

This chapter details efforts to assess the range and limitations of the novel CH_4 detection approach, the Normalized Differential Methane Index (NDMI). While the studies performed using the approach thus far have demonstrated the ability of the approach to detect enhanced levels of atmospheric methane using simulated MURI imagery, the extent of the approach's sensitivity to environmental conditions has not been evaluated. Additionally, the approach has not been applied to data collected by the MURI instrument, which would serve to further validate the approach.

This chapter will discuss two planned examinations that would have served to provide real data to test the NDMI method and the reason for their omission. The chapter then details two simulated studies performed in place of the real data studies.

Finally, a novel system referred to as MURI + is presented here. This novel instrument was designed to improve detection of atmospheric methane while taking advantage of additional bands that overlap with methane absorption lines. To assess the performance of this novel system, the Matched Filter approach is used.

5.2 Controlled Concentration Experiment

This section describes an experiment designed to evaluate the novel approach for detecting CH_4, the Normalized Differential Methane Index (described in Chapter 3 and Webber and Kerekes 2020 [96]). This experiment would have provided an opportunity to collect real data on a known quantity of CH_4. The experiment was scheduled to be performed in April of 2020. The arrival of the 2020 pandemic lead to the cancellation of this experiment.

5.2.1 Description of Controlled Release Experiment

In order to validate the CH_4 study performed on simulated data, an experiment was designed to test the methods of remote detection of enhanced atmospheric CH_4 with a known quantity of CH_4 present in the scene. The study was designed to be performed on the campus of the Rochester Institute of Technology without the MURI instrument. A higher spectral resolution thermal detector was to be used to collect radiance values. An apparatus that is highly transmissive in the thermal was designed to contain the CH_4.

The apparatus, a diagram of which can be seen in Figure 5.1 described above is a box made of a wood frame covered with polyethylene sheets. As CH_4 is less dense than air [21], the box is designed to have CH_4 pumped into the top of the container through an ALICAT mass flow controller MC-500SCCM-D/5M, Gas:CH4 [80]. A vent at the bottom of the box, which can be opened or closed, allows the comparatively higher density air to escape, ensuring that the pressure within the box remains constant. The ALICAT mass flow controller, shown in Figure 5.2, ensures we can both control and measure volumetric flow of the gas from a pressurized tank into the box. Knowing the flow rate and controlling the amount of time that the gas is allowed to flow allows us to control the amount of CH_4 within the box. Once the desired amount of CH_4 is pumped into the box, the open side of the box will be closed, trapping the CH_4 at the desired amount.

This apparatus with known CH_4 concentration would be placed between the sensor and a blackbody. For this experiment, the Model 102 Hand Portable FT-IR

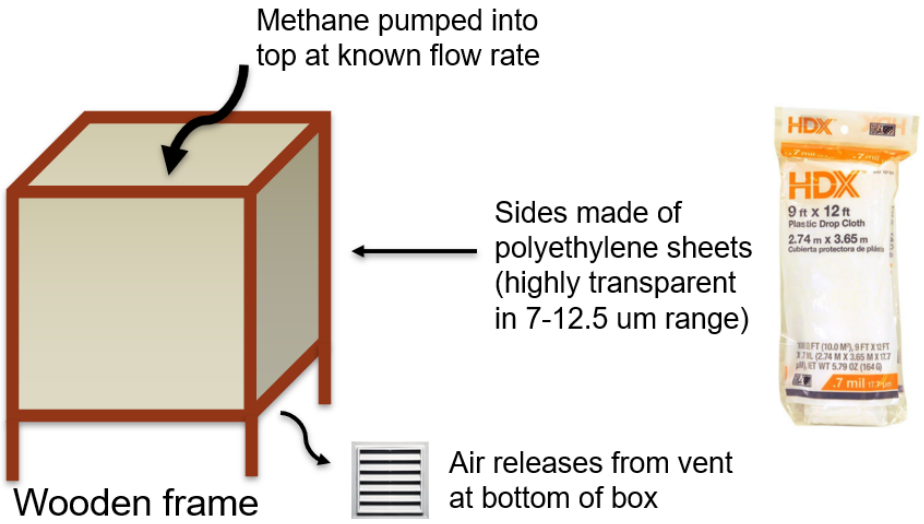

FIGURE 5.1: Overview of apparatus designed for controlled release CH_4 experiments.

FIGURE 5.2: Alicat Mass Flow Controller for use in the CH_4 controlled release experiment.

Spectrometer from D&P Instruments was the chosen sensor [2] [43][63]. This spectrometer has a spectral range between and 2 and 16 um and a spectral resolution of 4 wavenumbers. The range of this instrument covers the entire range of the MURI instrument and is therefore a suitable substitute to test CH_4 detection methods with. This also allows us to examine the absorption features of CH_4 in a controlled and realistic scenario. The goal of the collect would be to record radiance values of the blackbody at several temperatures with different amounts of CH_4 present in the apparatus. Following the collect, MURI's spectral response and additional noise would

be applied to the data to assess the system's CH_4 detection capabilities. Additionally, a series of atmospheric simulations performed using MODTRAN would provide us the ability to calculate at sensor radiance for MURI at operational height, allowing us to assess performance of the MURI airborne demonstration instrument with a controlled concentration of CH_4.

5.2.2 Determination of Transmission of Polyethylene Sheets

The experiment required the apparatus to have sides with high transmission in the thermal infrared. A large polyethylene drop cloth sample was tested to ensure the material was suitable for the experiment. Figure 5.3 shows how the material was assessed in a laboratory using the Model 102 Hand Portable FT-IR Spectrometer. Two radiance measurements were recorded of a blackbody at approximately 350 K, once with and once without the polyethylene sheet present. Calculating the transmissivity of the sheet was then accomplished by taking the ratio of the latter measurement to the former.

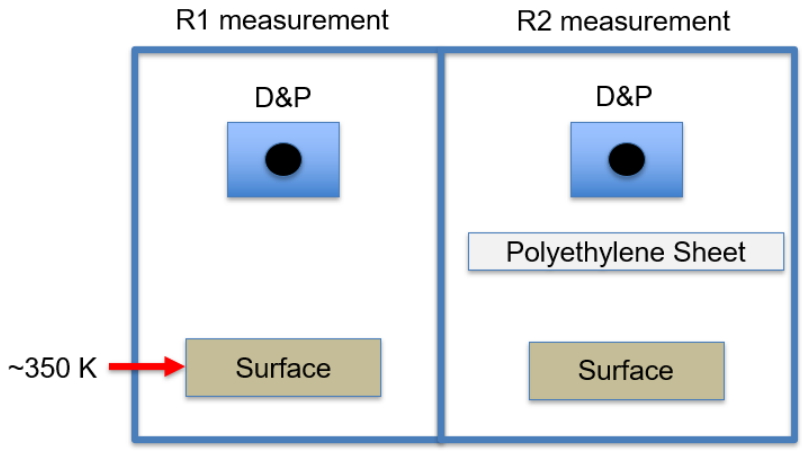

FIGURE 5.3: Diagram of polyethylene transmissivity measurement data collection. Calculating the ratio (R2/R1) provides transmissivity of target polyethylene sheet.

Figure 5.4 shows the transmissivity of the polyethylene sheet compared to both the normalized as-specified and normalized as-built MURI bandpasses. The sheet demonstrates a transmissivity of above 0.9 for bands 3, 4, 5 and 6. For band 2 the sheet shows nearly 0.9 and for band 1, which is important for NDMI, the sheet shows transmissivity of about 0.8. The transmissivity of the sheet remains relatively high

through this region of the thermal infrared and is therefore suitable for use in this examination. Characterization of the transmissivity curve is important to characterizing the absorption or emissivity of the CH_4 plume, and therefore this analysis should be performed on the entire constructed apparatus before data collection occurs.

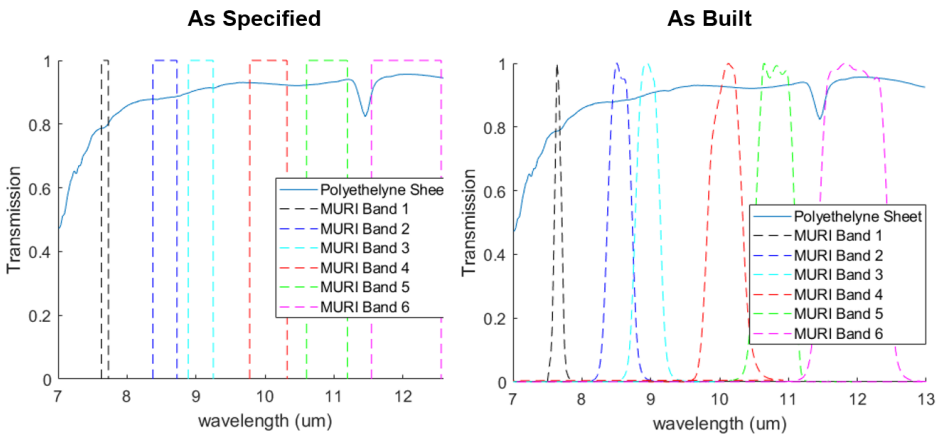

FIGURE 5.4: Diagram of polyethylene transmissivity measurement data collection. Calculating the ratio (R2/R1) provides transmissivty of target polyethylene sheet.

5.3 Test Flight Validation Over Known Emission Site

The simulated results predicted detectable scenarios; the controlled concentration experiment was intended to provide validation for those predictions. However, the best metric for evaluating MURI's CH_4 leak detection capability is to apply the chosen methods to real data collected with MURI's airborne demonstration instrument. Test flights for MURI were performed in August and September of 2019. During these test flights the MURI airborne demonstration instrument was flown over La Brea in Los Angeles, California, a known CH_4 emission location.

5.3.1 Test Flight Location: Hancock Park and Page Museum

The La Brea Tar Pits are located in Hancock Park, which resides in the Miracle Mile section of Mid-Wilshire, a neighborhood within the City of Los Angeles. The Tar Pits, and the surrounding area, have experienced both anthropogenic and natural CH_4 leaks due to the plentiful petroleum fields and tectonic activity beneath the city. The

approximately $0.1km^2$ area around the tar pits museum is home to approximately 100 visible gas seeps, though new seeps continue to form as existing seeps cease emitting. This location is known to have the highest measured natural gas flux for an onshore seepage zone in the United States. The emitting gas is primarily composed of CH_4, being about 80% CH_4 [30][97]. The high number of CH_4 leaks in a cluttered urban environment makes the La Brea pits scene a fitting test for the CH_4 detection methods for the MURI system.

Previously, studies have been performed to characterize the gas emissions from this area [30][97], where it was determined the magnitude of emissions from the park is comparable with emissions from mud volcanoes and large gas seeps in Europe and Asia. The scene was also used to demonstrate the ability of the Hyperspectral Thermal Emission Spectrometer (HyTES) to determine the spatial structure of CH_4 plumes and identify priority sources for follow up measurements [47].

FIGURE 5.5: Chosen flight path for MURI airborne demonstration instrument over La Brea Tar Pits at the Page Museum in Los Angeles, California. Testflight performed in August of 2019

The planned flight line for the MURI test flights performed at the end of August can be seen in Figure 5.5. The park is open to the public and was accessed by the ground team from RIT for ground based measurements. The ground based measurements consist of surface temperatures of nearby water bodies and ground

covers, emissivity measurements recorded using the Model 102 Hand Portable FT-IR Spectrometer produced by D&P Instruments. During the ground collection data, CH_4 values were recorded with a hand held CH_4 detector, which displayed values of 1% the lower explosive limit of CH_4, or approximately 500 ppm. As CH_4 is not visible it was not possible to determine the scale of the plume, therefore only point measurements were recorded.

5.3.2 MURI image data recorded over La Brea

An example of the data recorded over La Brea can be seen in Figure 5.6. This data was unfortunately recorded before the system was thermally stable, and therefore absolute brightness temperature will differ from the radiometry of the scene. This is not an issue for the NDMI approach, as the method utilizes relative radiance between each band, not absolute. However, there are two factors that caused this data to be non-ideal for assessment of the method. First, the shift in the as-constructed band 1, as described in Chapter 4, led to the contrast in band 1 being low, likely being dominated by water absorption features present in that region. Secondly, at the time of analysis, there was no method of stitching MURI band 1 imagery due to the low contrast of the images. As NDMI needs to be performed on pixels in both band 1 and band 6 recorded over the same target area, application to the unregistered data was not possible. Additionally, the unstable platform caused a considerable amount of image blur. This combination of factors thwarted the attempts at utilizing NDMI on this dataset.

As temperature retrieval was the primary focus on the first two MURI testflights, no additional CH_4 targets were added to the flight plan.

5.4 Application of Methane Detection Methods on HyTES Scenes With MURI's Spectral Response

While initial testflights of the MURI system did not produce imagery suitable for evaluation of our CH_4 detection approaches, testflight imagery of other thermal imagers can be utilized for this purpose. By applying the MURI spectral response to image data recorded in-flight by the HyTES instrument, a six-channel image with

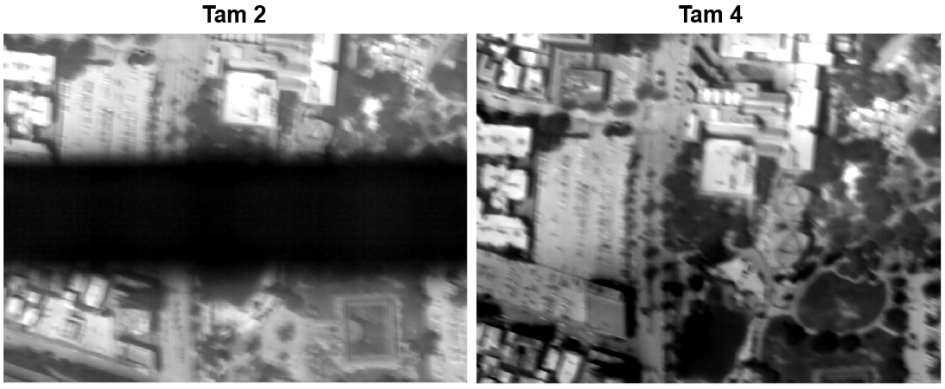

FIGURE 5.6: MURI images recorded over La Brea on August 30^{th}, 2019. The image on the left is from Tam 2, the top band is MURI band 5, the middle band is band 1, and bottom is band 3. The right image was recorded on Tam 4, the top band is MURI band 4, the middle is band 2, and the bottom is band 6.

MURI's spectral channels was created. This section describes a demonstration of the NDMI and Matched Filter as it is applied to this dataset.

5.4.1 Examination Description and Dataset Creation

In order to demonstrate the ability of both the MURI system and the NDMI approach to predict likely locations of enhanced atmospheric CH_4 in airborne remote sensing data, a MURI image was produced using imagery recorded in-flight by the Hyperspectral Thermal Emission Spectrometer (HyTES). As described in Chapter 3, HyTES is a hyperspectral imager with 256 thermal infrared spectral channels covering about the same range as MURI [42][47]. By applying MURI spectral response to the finer spectral resolution data, a MURI image was produced. To ensure the image best represented a MURI image, additional noise was simulated and added to the image using the method described in Chapter 3 section 3.3.2.

The selected images were recorded over Kern River Oil fields, a known location for anthropogenic CH_4 emissions[55][58]. The chosen scenes are identified in Figures 5.7 and 5.8. These Figures are gray scale images overlaid with HyTES Matched Filter predicted CH_4 plumes locations[47]. It is important to note that the flagged imagery provided by the HyTES team is produced using a combination of the Matched Filter approach and a plume dilation algorithm. Due to the use of the plume dilation algorithm, direct comparison between the flagged imagery and MURI predictions of

likely locations of enhanced CH_4 levels will not provide meaningful results. Instead, this examination provides a visual demonstration of how NDMI and Matched Filter applied to MURI data will produce intensity images that predict the locations of enhanced levels of CH_4 similar to the flagged images provided by HyTES.

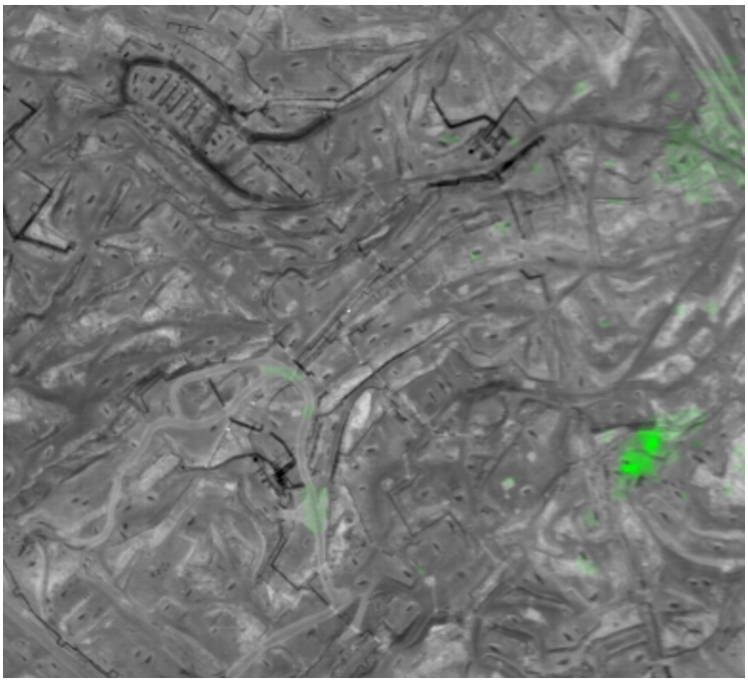

FIGURE 5.7: HyTES CH_4 flagged image; green indicates likely locations of enhanced levels of atmospheric methane. Image data recorded on 8 July 2014 over Kern County California.

5.4.2 Visualization of NDMI and HyTES Application to MURI Data Synthesized from HyTES In-flight Data

Figure 5.9 shows the results of applying the methods to both images. Both the NDMI and Matched Filter intensity images clearly identify similar plumes when applied to the selected scenes. The high density plume present near the center of the 5 February image is noted to lead to high intensity in both the NDMI and Matched Filter intensity images. The NDMI intensity image remains relatively high where the less dense plume exists, however there is little contrast with the background, or plume not present, pixels. The extent of the plume is clearer in the Matched Filter produced intensity image.

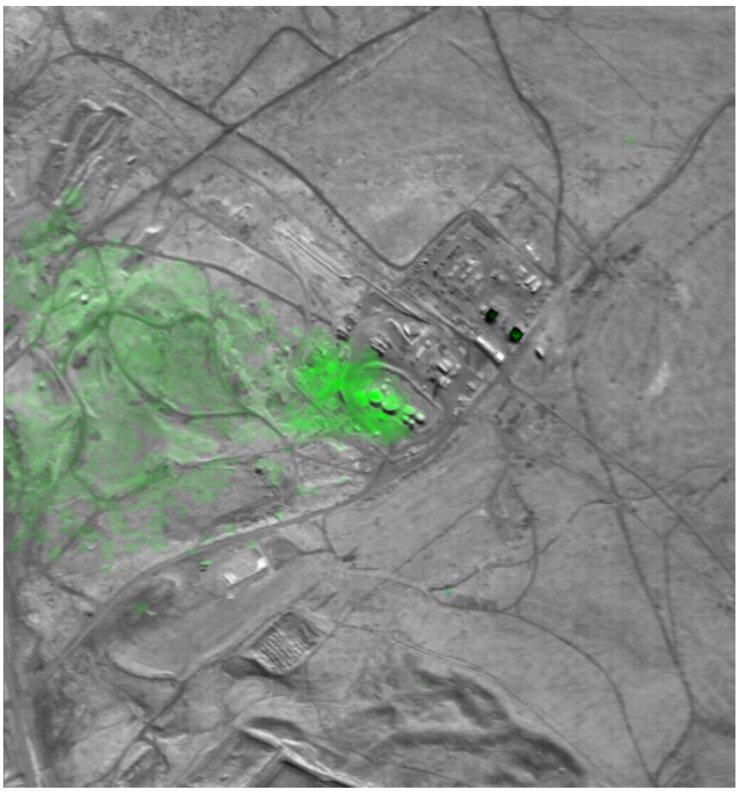

FIGURE 5.8: HyTES CH_4 flagged image; green indicates likely locations of enhanced levels of atmospheric methane. Image data recorded on 5 February 2015 over Kern County California.

On the right of 5.9, it is again noted that the NDMI approach is able to predict similar plumes to both MURI Matched Filter and HyTES Matched Filter. Both approaches show high intensity around the plume in the lower right of the image. Neither approaches show high intensity around the plume HyTES has identified in upper right corner of the image, though the Matched Filter does show a slight increase in intensity in that area. Overall, while the Matched Filter intensity image more closely resembles the prediction made by HyTES, the NDMI approach is still capable of identifying similar plumes while utilizing only two thermal bands. Additionally, this demonstration shows that MURI, a six band instrument with a single band allocated to methane absorption features, is capable of identifying enhanced quantities of atmospheric methane using the Matched Filter similarly to the HyTES Matched Filter, which utilizes 256 spectral bands.

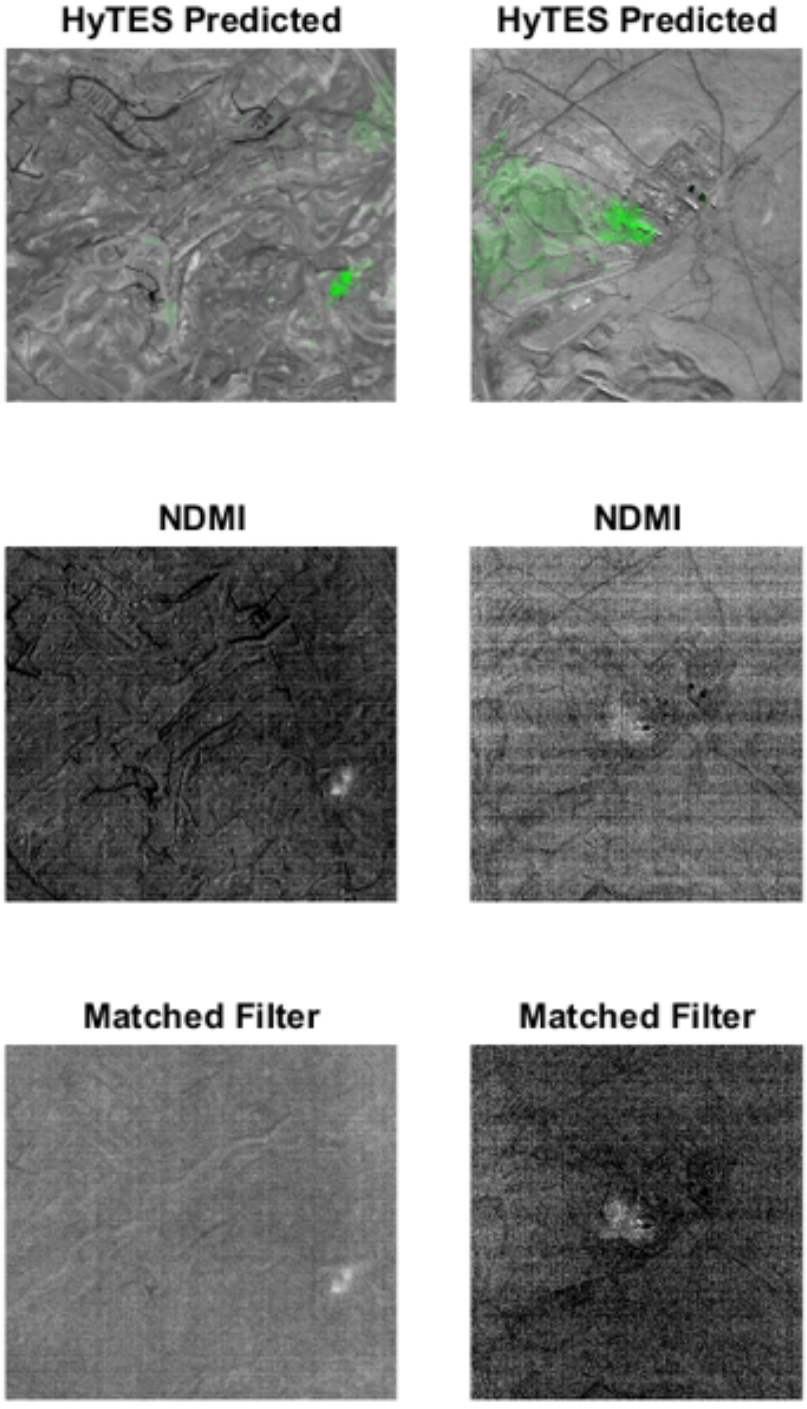

FIGURE 5.9: NDMI and Matched Filter intensity images for MURI image synthesized from HyTES images recorded over Kern County California. Left Column: 8 July 2014 image, Right Column: 5 February 2015.

5.5 Simulated Controlled Quantity Methane Experiment

This section describes an alternative controlled quantity CH_4 experiment. Similar to the controlled release experiment, the goal of this experiment is to validate the results shown in Chapter 3 and provide a more extensive examination of the capabilities of the NDMI method.

5.5.1 Validation of Methane Models Using Spectral Calc

In order to ensure the models used to evaluate the CH_4 detection methods in this section are a reasonable approximation of reality, a validation approach using Spectral Calc and MODTRAN6 was devised. Spectral Calc is a subscription based online high spectral resolution spectral modeling calculator [38][85]. This browser program allows users to calculate transmittance, absorption, and emission/radiance of a gas cell of user specified length, temperature, and pressure. The program allows users to choose between a selection of gasses, including CH_4, from a list of line databases. For this examination the HITRAN2016 was the chosen line list [39].

Figure 5.10 shows the setup for the first validation method performed with Spectral Calc. This simulated data represents a blackbody emitting through a CH_4 plume with no additional atmospheric gasses present. The two contributors to at-sensor radiance, described as path A and B, are described in Eqn. 5.2 and 5.3.

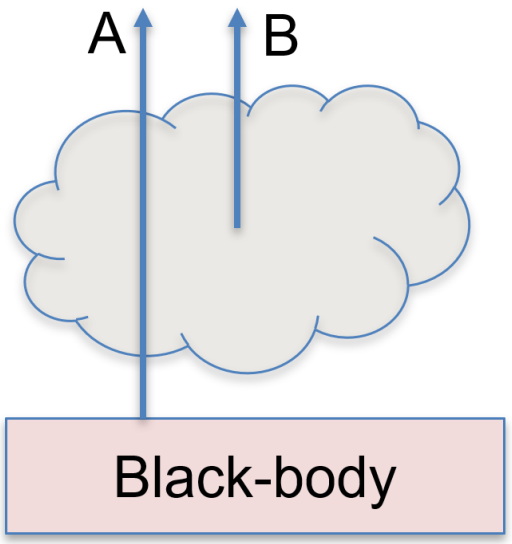

FIGURE 5.10: Spectral Calc/MODTRAN6 simulation setup for first analysis.

$$L_{atsensor} = L_A + L_B \tag{5.1}$$

$$L_A = \tau_{plume} L_{blackbody}(T_{surface}) \tag{5.2}$$

$$L_B = L_{plume} = \epsilon_{plume} L_{blackbody}(T_{plume}) \tag{5.3}$$

τ_{plume} is the transmissivity of the plume and $L_{blackbody}$ is the radiance emitted by a blackbody, which is a function of temperature. L_{plume} is the radiance emitted by the plume, modeled as the radiance emitted from the plume as a function of temperature multiplied by the emissivity of the plume ϵ_{plume}. Spectral Calc provides the transmission and emitted radiance of the CH_4 plume while the blackbody surface emission if provided by Planck's function and is calculated in MATLAB. The local chemical plume model of MODTRAN6 directly provides at-sensor radiance. Values for the inputs for MODTRAN simulations are shown in Table 5.1 while values for the inputs for the Spectral Calc simulations are shown in Table 5.2.

TABLE 5.1: MODTRAN at-sensor radiance simulation user defined atmosphere input values. Simulation was performed to compare to Spectral Calc for validation

MODTRAN Input	Value
Ambient temperature at surface	311 K
Ambient temperature at top of plume	311 K
Plume/Ambient temperature difference	-10 K
Surface temperature	328 K
Atmospheric gas scaling factor	0.0 %
Ground altitude	0.315 km
Sensor altitude	0.3351 km
Plume base/top	0.3151/0.3351 km
Plume concentration	5 to 70 ppm

While the MODTRAN simulations are performed with the assumption of an atmosphere, Spectral Calc calculations are performed with an assumption of taking place in a vacuum. This will cause a small shift in absorption/emission features. In order to compare the two sensor-reaching radiance calculations, this shift must be accounted for. This is done by dividing the wavelength in a vacuum by the index

TABLE 5.2: Spectral Calc inputs for comparison with MODTRAN simulation.

Spectral Calc Input	Value
Plume temperature	301 K
Plume length	20 m
Concentration	5 to 70 ppm

of refraction of air, which is assumed for the thermal infrared to be 1.00022. Spectral Calc can perform a calculation line-by-line or by applying a system function; the calculations performed here used Spectral Calc's line-by-line batch file option, with a Gaussian function being applied independently. Note the MODTRAN 6 simulations were performed using MODTRAN's built in Gaussian function.

Figure 5.11 shows the comparison between the MODTRAN and Spectral Calc at-sensor radiance calculations for a high concentration plume. There is high agreement between the two methods. Figure 5.12 shows the RMSE between the two datasets. The error in the case shown in Figure 5.11 is the highest for the cases examined, with the RMSE rising as concentration rises. As demonstrated in Webber and Kerekes 2020, the matched filter and NDMI detection methods for MURI are sensitive to much lower concentrations at this temperature difference.

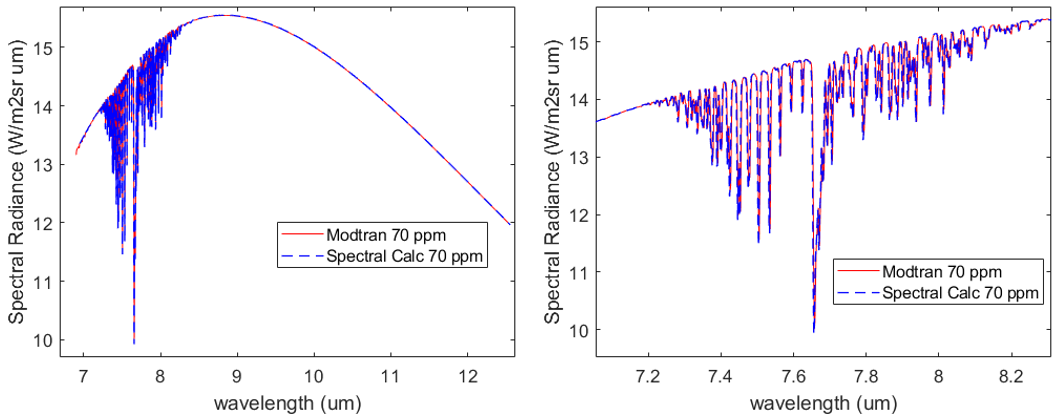

FIGURE 5.11: Spectral Calc and MODTRAN6 calculated at sensor radiance for a plume of 70 ppm and 301 K

From these calculations, radiance for each of MURI's six spectral channels was calculated, which can be seen in Figure 5.13. The calculated RMSE of band 1 between the two methods was 0.0263 $\frac{W}{m^2 \mu m sr}$ or 0.19 % of the mean MODTRAN value for

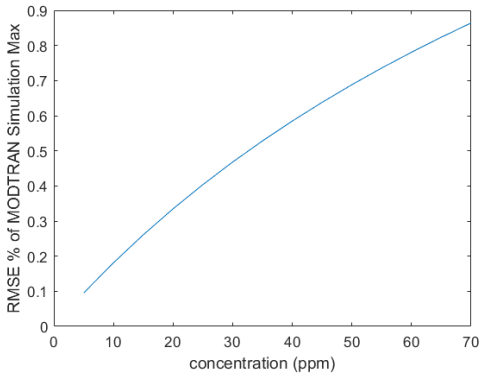

FIGURE 5.12: RMSE as a function of plume concentration from Spectral Calc and MODTRAN6 calculated at sensor radiance.

band 1. When converted to brightness temperature, the RMSE was 0.11 K, or 0.03 % of the mean band 1 brightness temperature. This examination demonstrated that MODTRAN and Spectral Calc have high agreement, and therefore simulating MURI data with either program would be appropriate for our analysis.

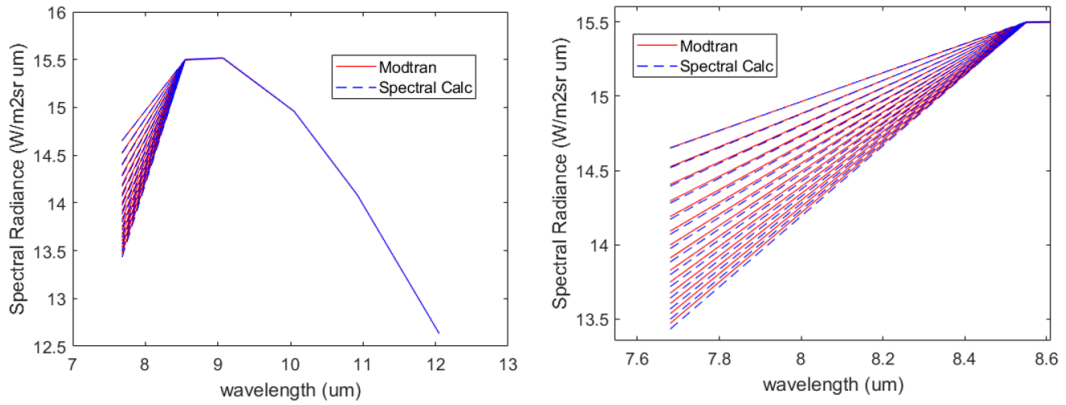

FIGURE 5.13: Spectral Calc and MODTRAN6 calculations for at sensor radiance for each MURI band for plumes of 5 to 70 ppm.

An additional comparison was performed using the two models. For this comparison, we attempted to recreate Figure 3.5 by replacing the local chemical plume model computed layers with the plume from Spectral Calc. A diagram for the setup for this analysis is displayed in Figure 5.14. For this arrangement, a MODTRAN simulation provides the surface leaving radiance up to the base of the plume. A second MODTRAN simulation is run from the base of the plume to the sensor. Spectral Calc provides the plume transmission and emission. This method assumes that the plume's effect on the thermal scattering above the plume is negligible. It should

be noted that this approach performed nearly identically to having the MODTRAN simulations not overlap with the Spectral Calc plume and instead having those layers only contain the CH_4 from Spectral Calc.

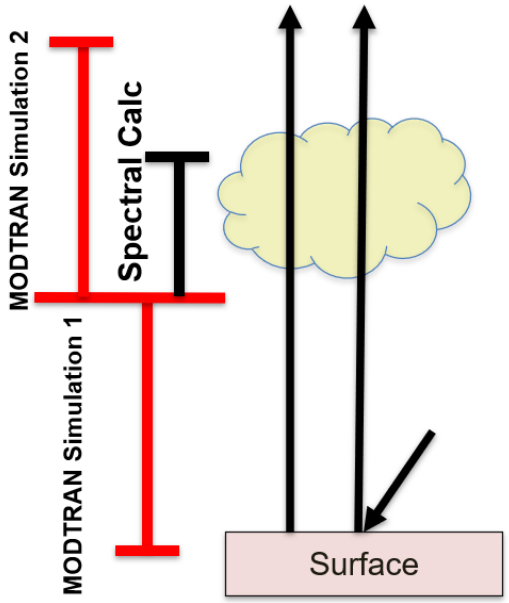

FIGURE 5.14: Diagram describing process of validating CH_4 experiments from Chapter 3. MODTRAN simulations run from the surface to the base of the plume, then from the base of the plume to the top of the atmosphere. Spectral Calc provides the transmission and emission of the plume.

Figure 5.15 shows the results of the simulated validation study side by side with the MODTRAN results from Chapter 3. As the figure shows, the detectable cases between the two approaches are very similar. However, the approach utilizing Spectral Calc shows slightly higher concentrations are required to have brightness temperature differences detectable by MURI. For example, both approaches show that a plume of temperature -10 K from ambient is detectable with a concentration of slightly more that 10 ppm. However, at ambient plume temperature, a plume of about 17 ppm has a detectable brightness temperature difference when using only MODTRAN. When including the Spectral Calc plume, a plume of concentration of about 20 ppm has a brightness temperature difference higher than MURI's NEdT. This is not a negligible difference, but the similar curve shapes in Figure 5.15 and the similar difference between detectable cases for each plume temperature does indicate some agreement.

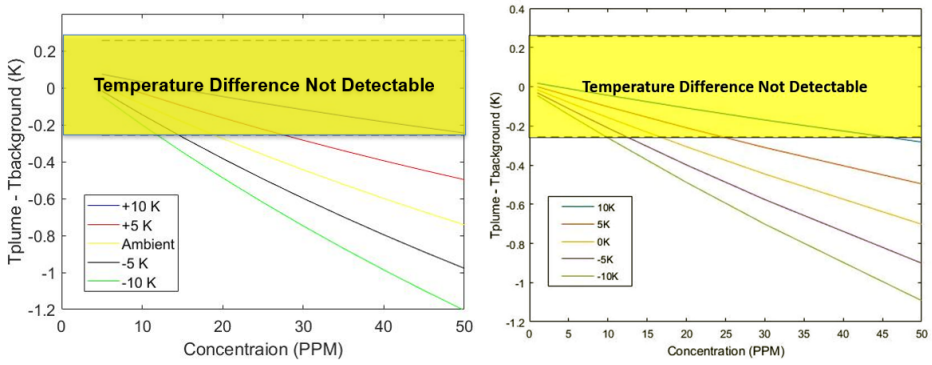

FIGURE 5.15: Left: Band 1 brightness temperature difference calculated from method shown above Right: Band 1 brightness temperature difference calculated from MODTRAN study performed in Chapter 3. Results indicate similar detectable cases.

From these examinations, it appears that the simulated at-sensor radiances that have been produced in MODTRAN6 are an acceptable representation of CH_4 plumes.

5.6 Simulated Controlled Concentration Experiment

This section will discuss the simulated controlled concentration experiments performed due to the cancellation of the experiments described in Section 5.2.

5.6.1 Description of Experiment

The goal of this experiment is to examine cases where the NDMI approach, described in Chapter 3, is viable for prediciting likely locations of enhanced levels of atmospheric CH_4. In pursuit of this goal, we also aim to discover the limits of the method, and therefore understand the extent of the abilities of a method that utilizes only two thermal bands to detect enhanced levels of atmospheric CH_4.

For this approach, MODTRAN6 was chosen to produce simulations of plumes at surface level. This approach uses the local chemical plume model discussed in Chapter 3 to simulate at sensor spectral radiances for both the on and off plume scenarios[13][10]. In order to ensure a reasonable atmosphere was being considered, and no longer being constrained by the physical location of the experiment, the simulated sensor reaching radiance can be defined using any reasonable scenario.

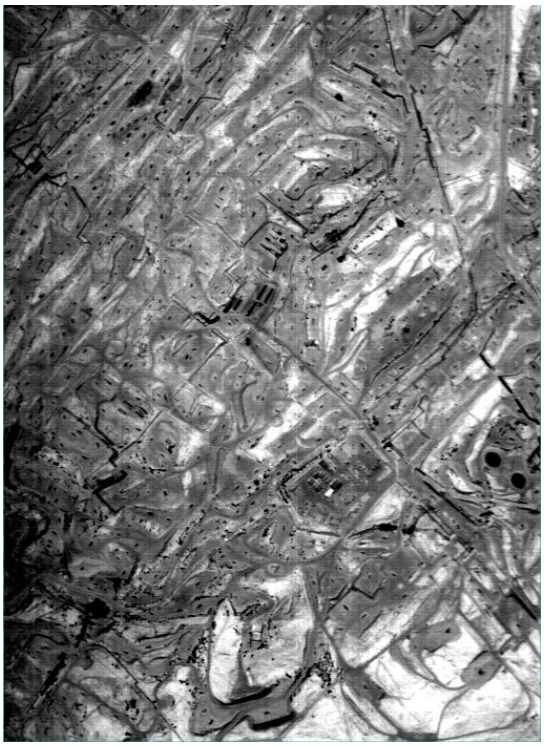

FIGURE 5.16: Single band view of HyTES image subset from July 8th, 2014. Parameters consistent with subset was used to produce the simulated dataset.

Chapter 3 includes a discussion of the ability of the model to reproduce real data similar to that seen in Figure 5.16.

MURI's spectral response is then applied to the spectral radiances produced by MODTRAN6. An off plume and an on plume simulated MURI image is constructed by repeating the radiance values for the on and off plume MODTRAN outputs over 1000 pixels then adding additional random noise corresponding to each MURI band. The NDMI method is then applied using MURI band 1 and MURI band 6, as described in Eqn. 5.4. This produces intensity images indicating likely locations of enhanced levels of atmospheric CH_4. Receiver Operating Characteristic curves (ROC) are created by applying a varying threshold to the NDMI images and determining where the method successfully differentiates between on and off plume pixels. The area under the ROC curve is then calculated, which is the selected metric for determining the success of the method for this experiment. Thousands of situations were considered for the coarse examination.

$$NDMI = \frac{SB2 - SB1}{SB2 + SB1} \tag{5.4}$$

5.6.2 Dataset Description

The dataset for this investigation is placed into two categories: coarsely sampled and finely sampled. The coarsely sampled data was used to describe the capabilities of the NDMI approach across a wide range of circumstance, while the finely sampled data was used to assess the approach in greater detail in specific circumstances.

The considered scenario for the coarse evaluation is based on a scene used in the study presented in Chapter 3. The scene can be seen in Figure 5.16 and is an example of a known location where the matched filter approach was able to predict likely location of CH_4 plumes from HyTES data[47][56]. The image was recorded in July of 2014 over Kern River Oil Fields, just North of Bakersfield, California, a region that has seen enhanced levels of atmospheric CH_4 greater than 30 ppm and regularly experiences levels around 10 ppm[58]. Table 5.5 describes select parameters of consideration for the MODTRAN simulation that were held constant across the examination, and Table 5.6 describes the parameters that were adjusted during the dataset creation.

As described in Chapter 2, surface temperature to plume temperature differential is likely to have the greatest effect on plume detectability. Water vapor scaling factor is expected to have an effect on plume detectibility, as the presence of strong water absorption features could mask a CH_4 plume's absorption or emission features. Plume concentration and thickness will determine the strength of the CH_4 absorption or emission features. While the user-defined atmosphere being used defines the temperature profile and the characteristics of the plume, the baseline atmosphere variable controls other aspects of the atmosphere. This includes the concentration of atmospheric gases. For example, MIDLAT WINTER contains about 30% of the column water vapor of MIDLAT SUMMER while containing about 1% higher methane. The CH_4 scaling factor controls the background CH_4 quantity by directly scaling the CH_4 at each layer of the modeled atmosphere. During the dataset reconstruction, a scaling factor of 0.4 was determined to match the background methane features in the HyTES scene. Table 5.3 details the MODTRAN model atmosphere vertical

molecular column amounts in atm-cm for water, while 5.4 describes the same for CH_4, as well as sample values after scaling. The NDMI approach should behave similarly across surfaces with differing emissivity, therefore changing the surface emissivity between images is not expected to affect the method. However, changes in surface emissivity within an image is likely to affect the method, which is discussed further in this section.

TABLE 5.3: Scaled MODTRAN model atmosphere vertical molecular column amounts in atm-cm for H_2O

	0.1	0.5	1.0
MIDLAT SUMMER	363.6 atm-cm	1818.0 atm-cm	3635.9 atm-cm
MIDLAT WINTER	105.97 atm-cm	529.85 atm-cm	1059.7 atm-cm

TABLE 5.4: Scaled MODTRAN model atmosphere vertical molecular column amounts in atm-cm for CH_4

	0.4	1.0
MIDLAT SUMMER	0.5074 atm-cm	1.2684 atm-cm
MIDLAT WINTER	0.5122 atm-cm	1.2806 atm-cm

In addition to the environmental considerations, the method will also be sensitive to instrument parameters, specifically the system's noise. In order to demonstrate the NDMI sensitivity to system noise and further describe the method's sensitivity to environmental parameters, the image noise was varied by applying a simple noise scaling factor to MURI's system noise, as defined in Chapter 3 Table 3.1.

TABLE 5.5: MODTRAN parameters held constant for coarse evaluation

Parameter	Value
Collection Height	4.572km (15000 feet)
Ambient Temperature at Plume Altitude	311 K
Plume Distance from Surface	0 m

The coarse evaluation provided information on circumstances that would be interesting to examine more finely. The parameters kept constant for the fine analysis are displayed in Table 5.7, while the parameters treated as variable are displayed in Table 5.8.

TABLE 5.6: MODTRAN parameters and the respective values used in the coarse evaluation.

Model Input	Value
Atmosphere	MIDLAT SUMMER, MIDLAT WINTER
Water Vapor Scaling Factor	0.1 - 1.0
CH_4 Scaling Factor	0.4, 1
Surface Temperature	273.15 - 333.15
Surface Emissivity	SANDY_LOAM/GRASS/URBAN
Plume Thickness	10 m, 20 m
Plume Concentration	7, 10, 20, 25, 27, 30 ppm
Plume/Ambient Temperature Difference	-10, 0, +10 K
Noise Scaling Factor	0.1, 1.0

TABLE 5.7: MODTRAN parameters held constant for fine evaluation

Parameter	Value
Collection Height	4.572km (15000 feet)
Ambient Temperature at Plume Altitude	311 K
Plume Distance from Surface	0 m

TABLE 5.8: MODTRAN parameters and the respective values used in the fine evaluation.

Model Input	Value
Atmosphere	MIDLAT SUMMER, MIDLAT WINTER
Water Vapor Scaling Factor	0.1 - 1.0
CH_4 Scaling Factor	0.4, 1
Surface Temperature	283.15 - 333.15
Surface Emissivity	SANDY_LOAM/GRASS/URBAN
Plume Concentration	10, 20, 30, 32 ppm
Plume Thickness	10, 20 m
Noise Scaling Factor	0.1, 1.0

5.6.3 Multi-Surface Examination Dataset

A selection of multi-surface examinations were performed using a subset of the simulations described above. These examinations were designed to determine the NDMI method's sensitivity to surface temperature and emissivity changes within a scene. Table 5.10 describes the selected simulated circumstances and Table 5.9 details the parameters held constant for this examination. For this examination, the

results are compared to the Matched Filter approach, as described in Chapter 3. Recall that, unlike the NDMI approach, the Matched Filter approach makes use of all six of MURI's spectral bands. Each of the scenarios were selected by identifying cases where CH_4 detection was highly accurate. This allows us to determine the effect, if any, of adding additional surface types to the images.

TABLE 5.9: MODTRAN parameters held constant for NDMI and Matched Filter multi-surface application evaluation.

Parameter	Value
Collection Height	4.572km (15000 feet)
Ambient Temperature at Plume Altitude	311 K
Plume Temperature Difference to Ambient	-10 K
Plume Concentration	10 ppm
Plume Thickness	10 m
Atmosphere	MIDLAT SUMMER
Water Vapor Scaling Factor	0.1
CH_4 Scaling Factor	0.4
Noise Scaling Factor	0.1

TABLE 5.10: Simulated image surface definitions for NDMI and Matched Filter multi-surface application evaluation.

Examination #	Description	Surfaces	Temperature Range
1	Identical surface, small temperature difference	Sand	323/328 K
2	Identical surface, large temperature difference	Sand	310/325 K
3	Different surfaces, same temperature	Sand/Urban	325 K
4	Different surfaces, small temperature difference	Sand/Urban	325/320 K
5	Different surfaces, large temperature difference	Sand/Grass	325/300 K

For the examinations number 1 and 2, four different surface configurations were considered. For examinations 3, 4, and 5, three surface configurations were considered. These configurations are labelled S1-S5 and are detailed in Table 5.11. S1 evaluates the approach on an image where 10 % of the pixels are defined using the surface of lower temperature. S2 uses an image where the pixels are split evenly between the two surface types/temperatures. S3 defines 50% of the pixels as the higher temperature surface and defines the other 50 % as having equal number of pixels with each whole value surface temperature in Kelvin between the low and high temperature chosen for each case. S4 evaluates the approach on a simulated image with an equal number of pixels for each whole value temperature in Kelvin

between the low and the high temperature. S5 is similar to S3, but is used when evaluating surfaces with differing emissivities as well. Therefore S5 is applying the approaches to a simulated image where 50% of the pixels are the surface emissivity of one type and the other 50% of pixels are defined as the second surface type with temperatures ranging from the low temperature to the high temperature.

TABLE 5.11: Description of simulated image construction for multi-surface NDMI and Matched Filter evaluation.

Label #	Surface Configuration Description
S1	10/90 % pixel split between surface 1 and surface 2
S2	50/50 % pixel split between surface 1 and surface 2
S3	50 % high temperature surface, 50% gradient from low to high temperature
S4	Equal number of pixels for temperatures between low and high temperature
S5	50 % surface 1, high temperature, 50% surface 2, gradient from low to high temperature

5.6.4 Coarse Examination Results

A selection of the results from the coarse sampling are presented here. As there are a large number of results, a select few heat maps are presented here to describe the detection approaches behavior across the simulated data. Figure 5.17 shows a scenario where a 20 m plume of 27 ppm above background level at -10 K from ambient temperature (301K) can be detected against a background case with 0.4 background methane scaling factor. A successful case for this examination has an area under the ROC curve of 0.8 or greater. For the heat maps presented here, blocks marked red have higher ROC curve areas and blue have lower. Using this scenario, it should be noted that surface emissivity between images does not significantly impact the effectiveness of the method, as expected. The factor with greatest effect demonstrated here is surface temperature, as it determines the plume/surface temperature difference. In this scenario, the approach leads to high detectability when the surface to plume temperature difference is greater than 20 K. Water column vapor has a significant effect as well, especially using the Summer atmosphere which has significantly more water in the column. The range of detectable cases increases with the decrease of water column vapor.

Reducing the image noise shows similar patterns in the results. Figure 5.18

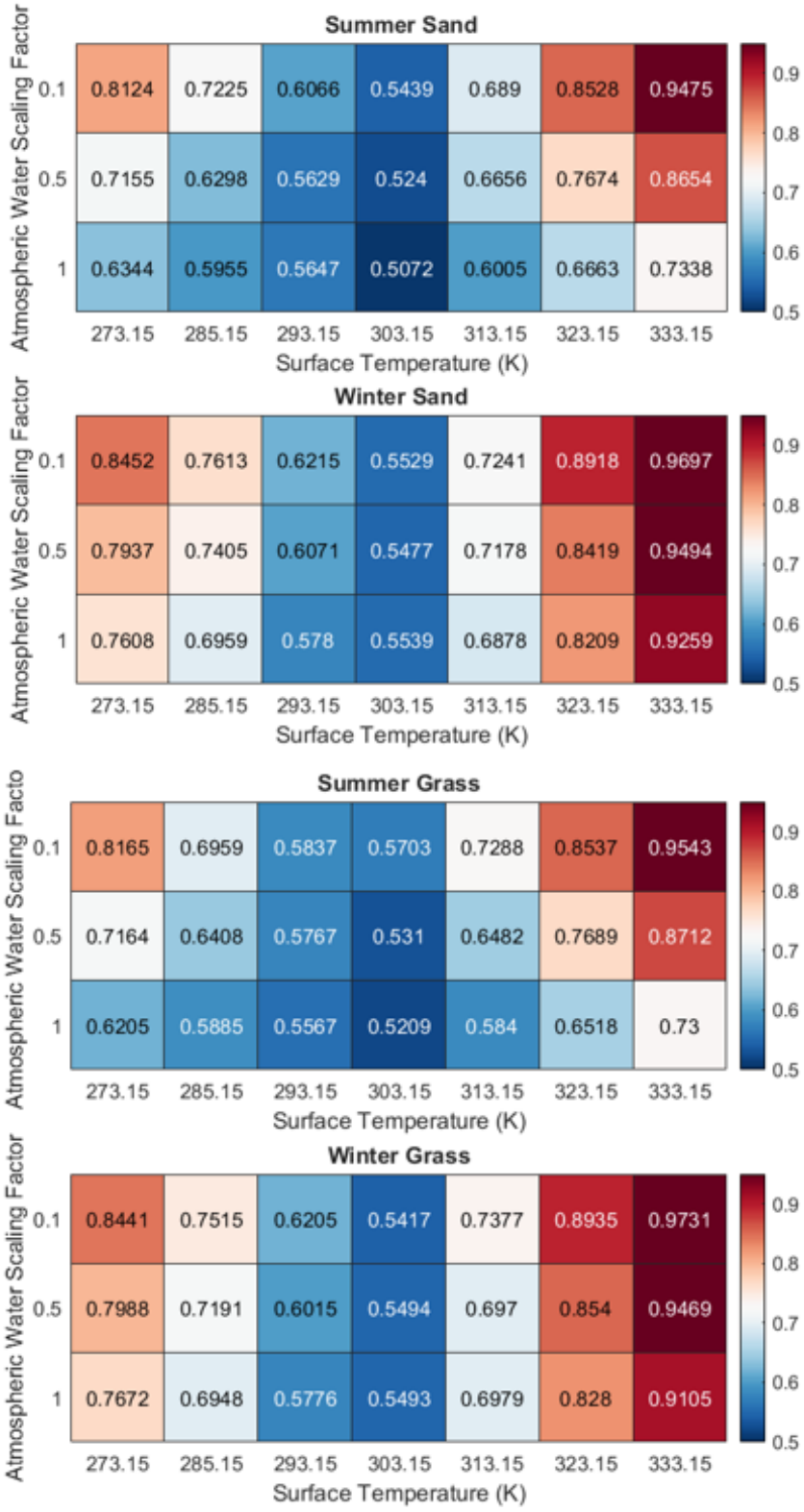

FIGURE 5.17: Heat map describing area under ROC curve for NDMI identified enhanced concentration methane plumes pixels. Simulation used: 27ppm plume, -10 K plume ambient temperature difference (301 K), 20 meter plume thickness, 1.0 noise scaling factor.

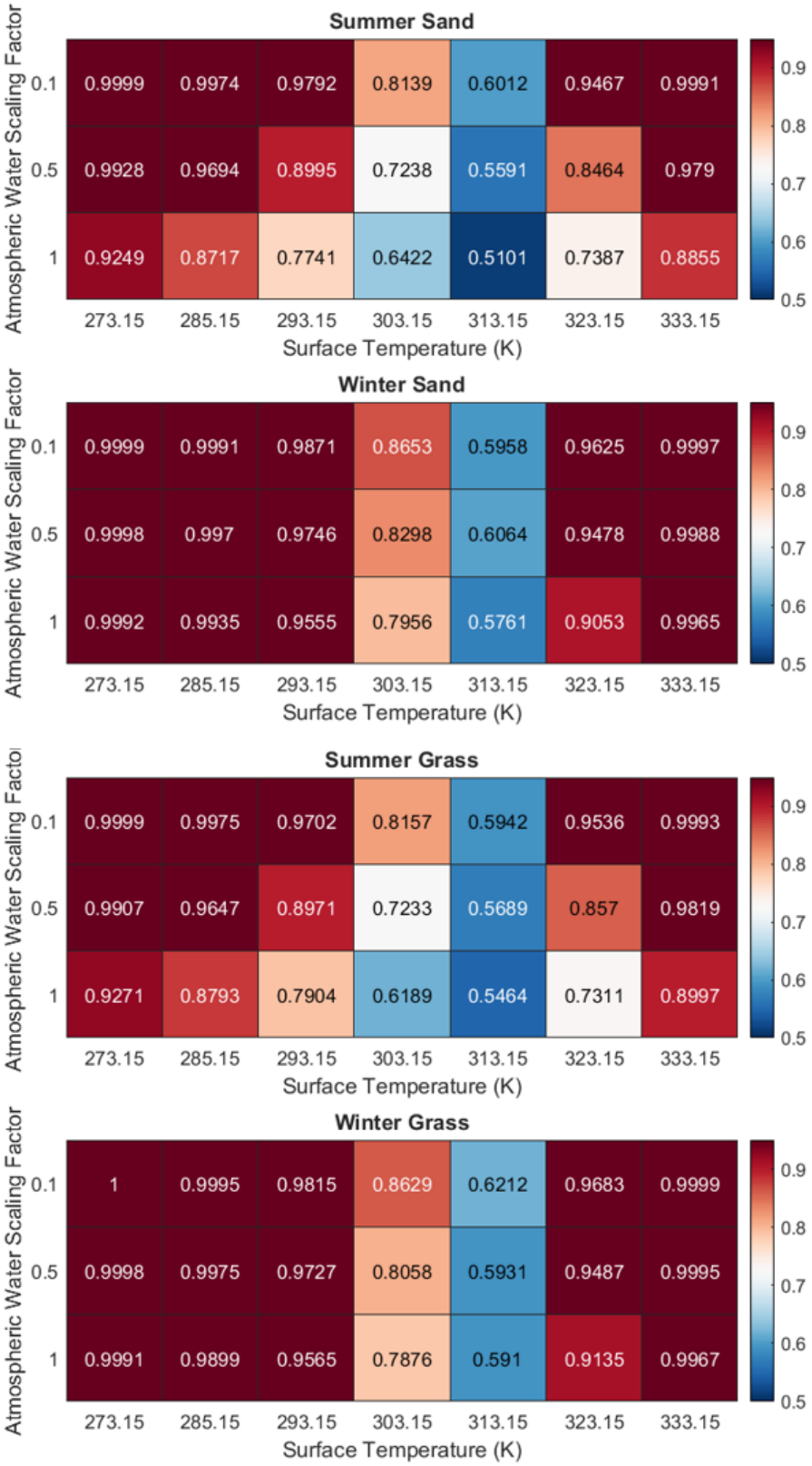

FIGURE 5.18: Heat map describing area under ROC curve for NDMI identified enhanced concentration methane plumes pixels. Simulation used: 7ppm plume, ambient temperature (311 K), 20 meter plume thickness, 0.1 Noise scaling factor.

shows a scenario where a 20 m plume of 7 ppm above background level at ambient temperature can be detected against a background case with 0.4 background methane scaling factor with an image noise scaling factor of 0.1. Again it is noted that surface emissivity between images does not significantly impact the effectiveness of the method. this figure futher demonstrates that surface to plume temperature difference is a a key factor in the detectability of the plume; note that the plume is at ambient temperature, 311 K. In this scenario, the approach leads to high detectability when the surface to plume temperature difference is $\pm 10K$. The water column vapor effect is easily viewed here, especially using the Summer atmosphere which has significantly more water in the column. The range of detectable cases increases with the decrease of water column vapor, showing detectable scenarios where the temperature difference is greater than -10 K but less than 0. This shows that the required temperature difference even for relatively lower concentration plumes in drier environments, while considerable, is relatively small. Comparing Figure 5.18 to Figure 5.17 reveals how impactful the system noise is on the method, as reducing the noise has allowed the detection of a plume with a concentration four times lower than that of 5.17.

Figure 5.19 shows a similar scene, but the plume width is reduced to 10 m. The results are condensed to a single surface type here, for as with results shown in Figure 5.18, the type of surface in each scene did not significantly alter the results. The result, as expected, is that the plume is detectable in fewer scenarios. The method's dependency on column water vapor is still obvious when examining these results. In the case using the Mid Latitude Summer atmosphere with a water column scaling factor of 1.0, the plume presence is significantly masked even when the surface/plume temperature difference is around 40 K. In this example, the system is still considerably better at identifying plumes than by chance, but it does not meet the 0.8 threshold.

Figure 5.20 shows the results of applying NDMI to a slightly different scene. The background CH_4 scaling factor is raised from 0.4 to 1, meaning the simulation is now using the standard values for MODTRAN Mid Latitude atmospheres. The concentration of the plume is increased to 10 ppm and the thickness is kept to 10 m. Once again, the surface temperature and water column vapor have the same effect. Note

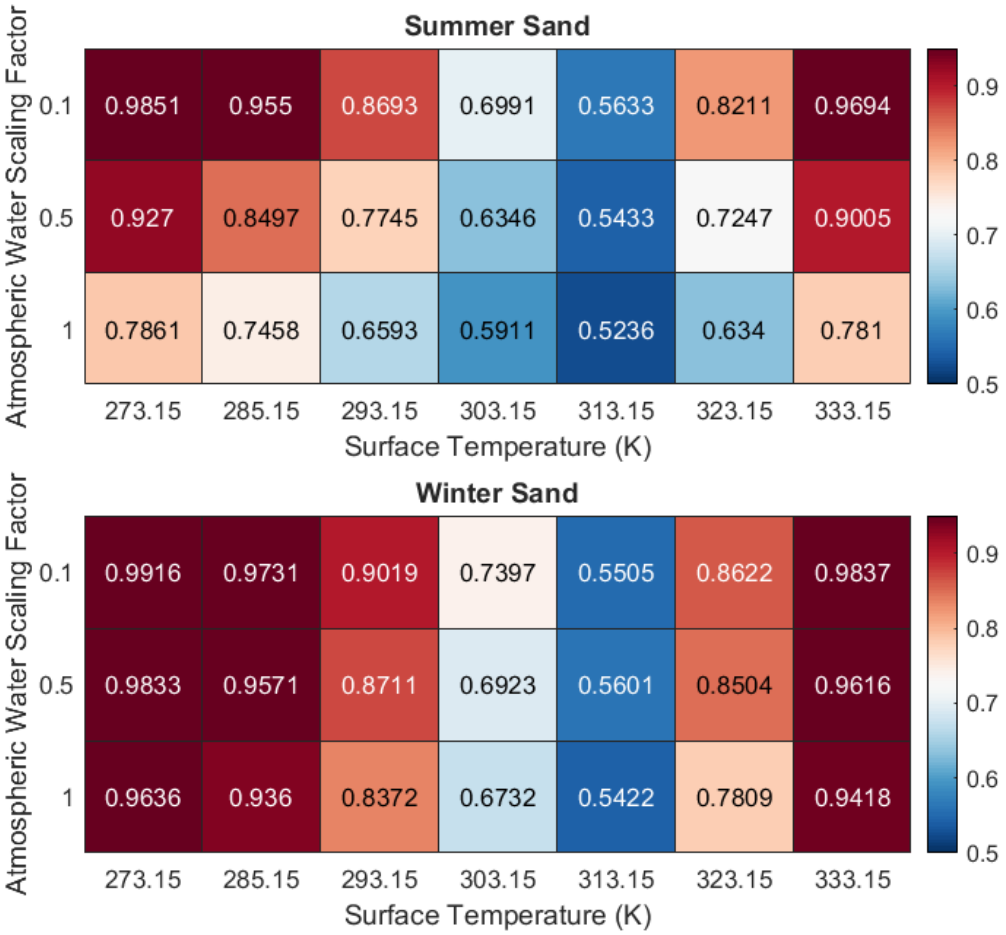

FIGURE 5.19: Heat map describing area under ROC curve for NDMI identified enhanced concentration methane plumes pixels. Simulation used: 7ppm plume, ambient temperature (311 K), 10 meter plume thickness, 0.1 noise scaling factor.

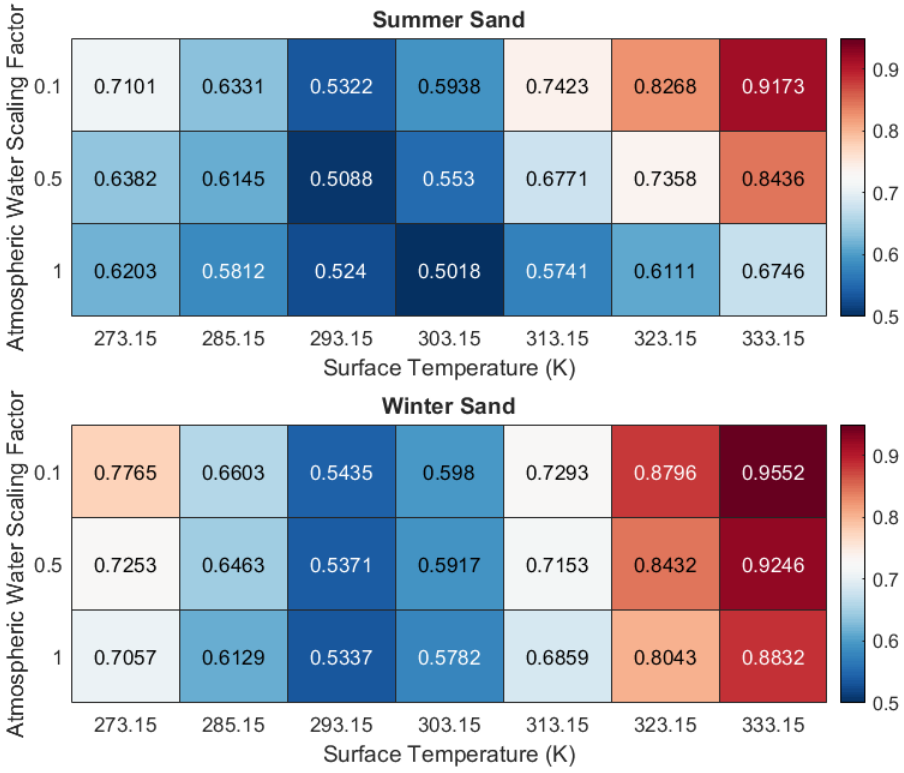

FIGURE 5.20: Heat map describing area under ROC curve for NDMI identified enhanced concentration methane plumes pixels. Simulation used: 10ppm plume, -10 K to ambient temperature, 10 meter plume thickness, 0.1 noise scaling factor.

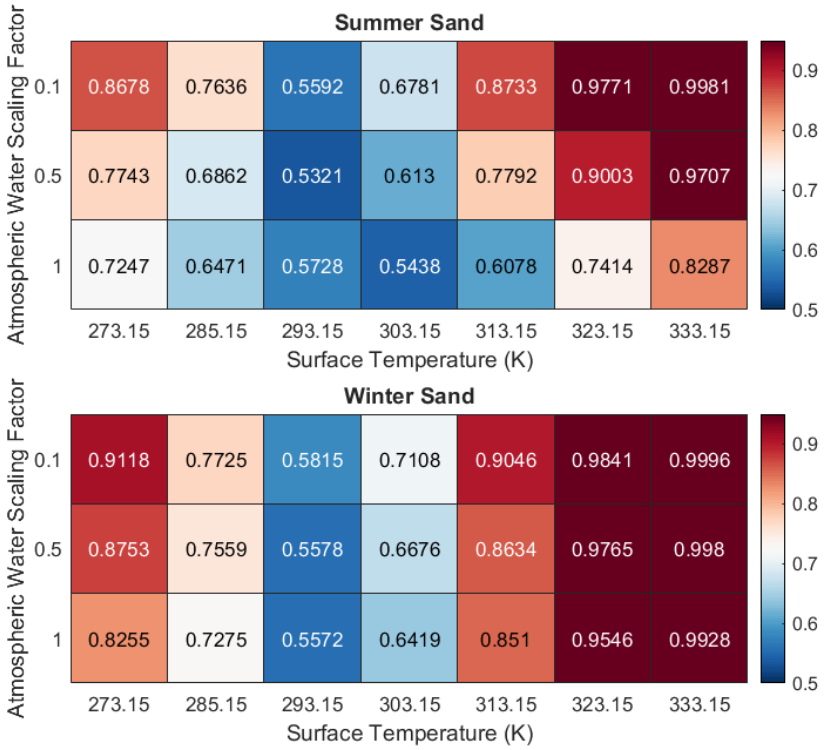

FIGURE 5.21: Heat map describing area under ROC curve for NDMI identified enhanced concentration methane plumes pixels. Simulation used: 10ppm plume, -10 K to ambient temperature (301 K), 20 meter plume thickness, 0.1 noise scaling factor.

that the plume is now at 301 K, meaning the plume surface temperature difference is lowest at 303.15 K. The increase in background CH_4 masks the presence of the plume, save for when the surface/plume temperature difference is greater than +20 K. When the surface is cooler than the plume, the NDMI approach is unable to reach the 0.8 threshold even for the case where the surface/plume temperature difference is about -30 K. Although, it should be noted that the scenario this experiment was based on features a hot dry scene, where surface temperatures with temperatures higher than 330 K are possible.

Doubling the thickness of the plume increases the number of cases above the 0.8 threshold, as shown in Figure 5.21. The increase in plume thickness is not always enough to overcome the masking caused by water absorption features. In scenarios with lower column water vapor, the increase in plume thickness had a greater effect. The thicker plume, with a CH_4 scaling factor of 1, requires a surface/plume temperature difference around +10 to 20 K depending on the atmospheric water content. When the surface is cooler, the approach is capable of detecting plumes when the surface/plume temperature difference is about -30 K.

These patterns can be further exemplified with the cases containing higher noise. Figure 5.22 shows a 20 m plume of 25 ppm at ambient temperature with a CH_4 scaling factor of 0.4 and a noise scaling factor of 1.0. This scene leads to detectable scenarios primarily when the water column vapor is low. The heatmap in Figure 5.23 was created using a simlar scene, yet the plume concentration was increased to 30 ppm and the plume width was reduced to 10 m. Between these two cases, the lower concentration plume is detectable in many cases, while the thinner, higher concentration plume is detectable in a single case: Winter, 0.1 water scaling, and a plume/surface temperature contrast of around 40 K. This exemplifies how impactful both the width of the plume and the system noise can be on the detectability of the CH_4 plume.

5.6.5 Fine Examination Results

For the fine analysis, a simulation similar to the plume used to demonstrate NDMI in Chapter 3 was used. A plume of 10 ppm above ambient at -10 K from ambient (301 K) was chosen. This simulation differs from the simulation in Chapter 3 as the plume

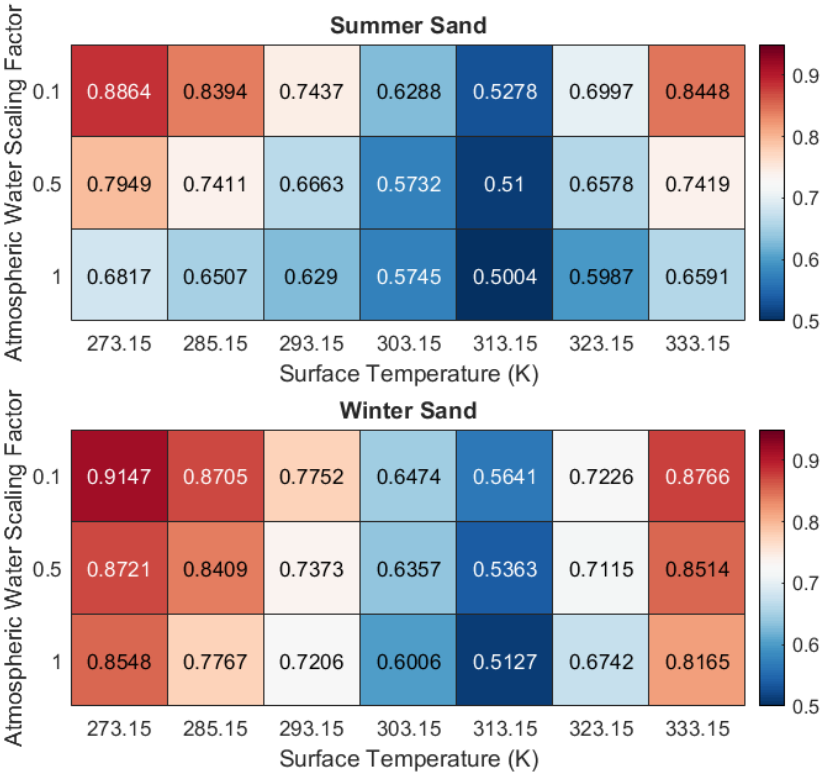

FIGURE 5.22: Heat map describing area under ROC curve for NDMI identified enhanced concentration methane plumes pixels. Simulation used: 25ppm plume, ambient temperature (311 K), 20 meter plume thickness, 1.0 noise scaling factor.

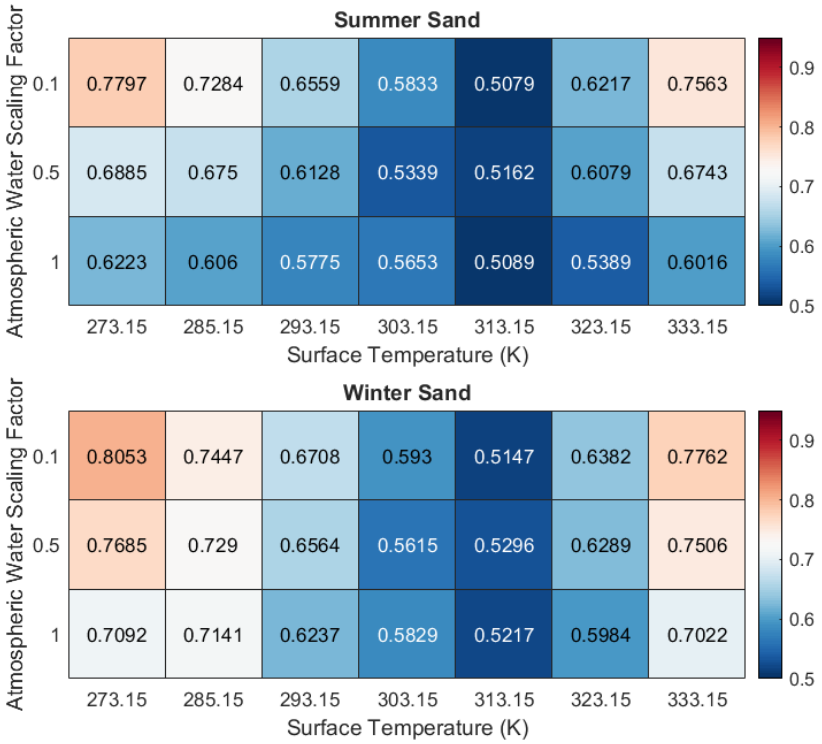

FIGURE 5.23: Heat map describing area under ROC curve for NDMI identified enhanced concentration methane plumes pixels. Simulation used: 25ppm plume, ambient temperature (311 K), 10 meter plume thickness, 1.0 noise scaling factor.

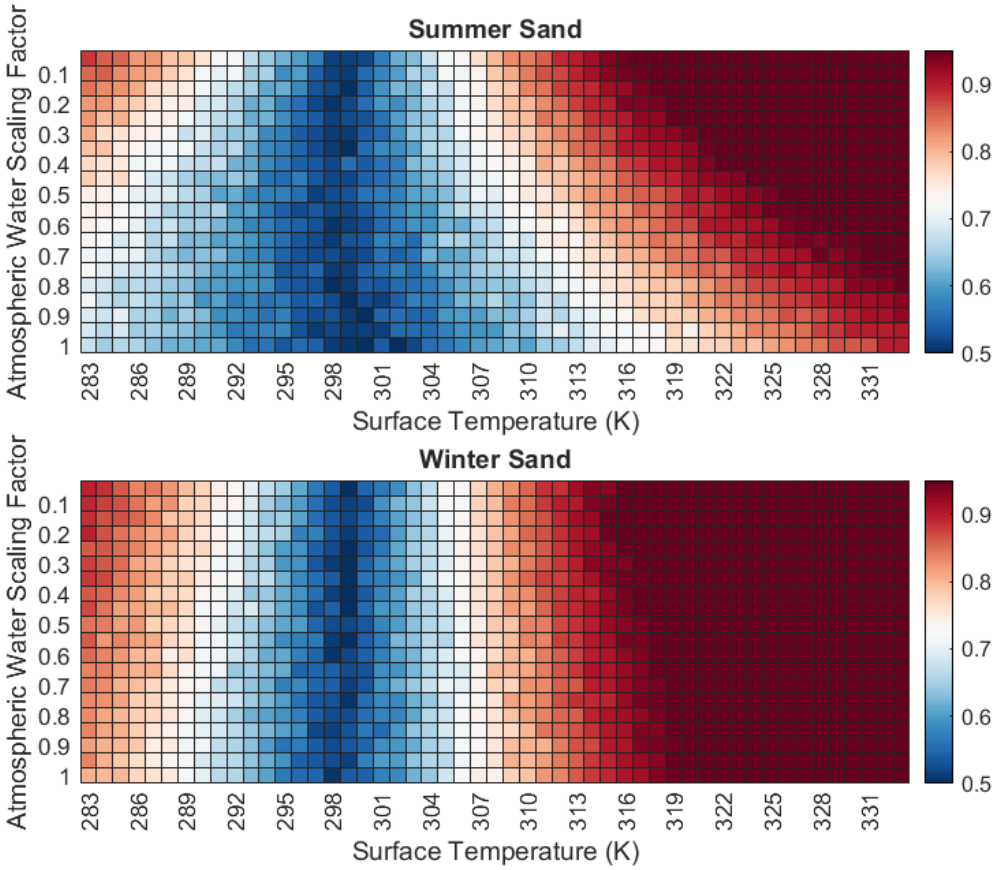

FIGURE 5.24: Fine scaled heat map describing area under ROC curve for NDMI identified enhanced concentration methane plumes pixels. Simulation used: Kern Valley recreation, 10ppm plume, -10 K to ambient temperature (301 K), 10 meter plume thickness, 0.1 noise scaling factor.

has a thickness of 10 m rather than the 20 m used previously. Figure 5.24 shows the results of applying the NDMI approach to the simulated radiances. The fine results allow us to better visualize the effects of water vapor and surface temperature on the detectability of the plume with NDMI. From this heat map, it is evident that increasing the water column vapor from 0.1 to 1.0 can change the necessary surface temperature for detection by almost 20 K. As this scene is based on a desert scene, a low column water vapor is expected. When the surface is significantly cooler than the plume, the plume is detectable in cases with comparably lower column water vapor. In these cases, a surface with a temperature difference of less than -15 K to the plume temperature is detectable.

Additionally, a simulation with a plume of 10 ppm that is 20 m thick and -10 K from ambient (301 K) was produced, similar to the plume used to demonstrate NDMI in Chapter 3 but with the background methane scaling factor set to 1.0. Figure 5.25 shows the results of applying the NDMI approach to the simulated radiances. In this heat map, it is evident that increasing the water column vapor from 0.1 to 1.0 can change the necessary surface temperature for detection by almost 10 K. As this scene is based on a desert scene, a low column water vapor is expected. For the Mid Lat Winter Atmosphere, which with column water vapor scaling factor of 1.0 has about 30% of the water in the Mid Lat Summer, a surface/plume temperature difference of about +8 to 10 K is needed to reliably identify plume present pixels. Surface temperatures of greater than +10 K reliably detect methane pixels over all surfaces. However, for high column water vapor, a surface temperature nearly 20 K higher than the plume is needed to reliably identify plume present pixels. The most noticeable change is the loss of detectability in lower temperature plumes. Only simulations where the surface/plume temperature difference was large and the column water vapor was less than 50% in the Winter baseline atmosphere and 10% in the summer atmosphere was the plume detectable. Overall, it appears the effect of increasing the background levels of CH_4 is more significant than doubling the thickness of the plume.

Figure 5.26 is a demonstration of a high noise case. This scenario includes a 20 meter plume of 30 ppm with a CH_4 of 0.4 and a 1.0 noise scaling factor. Again a higher plume concentration is required for detection when compared to the lower

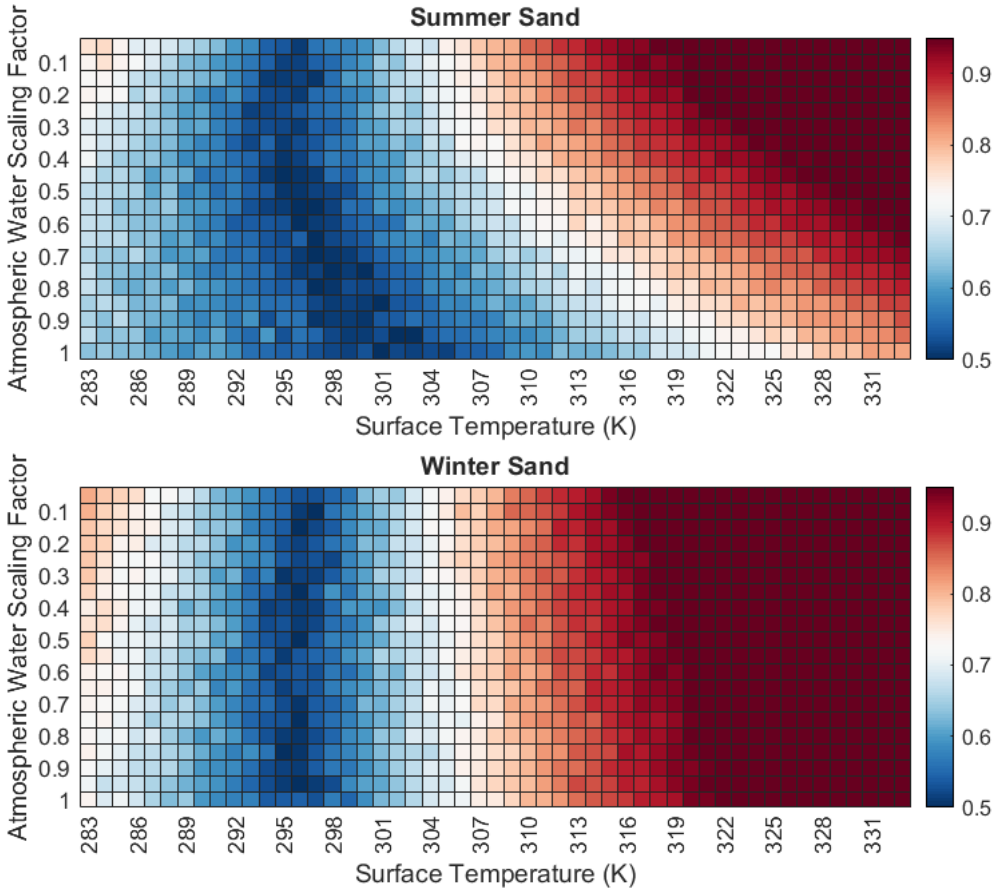

FIGURE 5.25: Fine scaled heat map describing area under ROC curve for NDMI identified enhanced concentration methane plumes pixels. Simulation used: 10ppm plume, -10 K to ambient temperature (301 K), 20 meter plume thickness, 0.1 noise scaling factor.

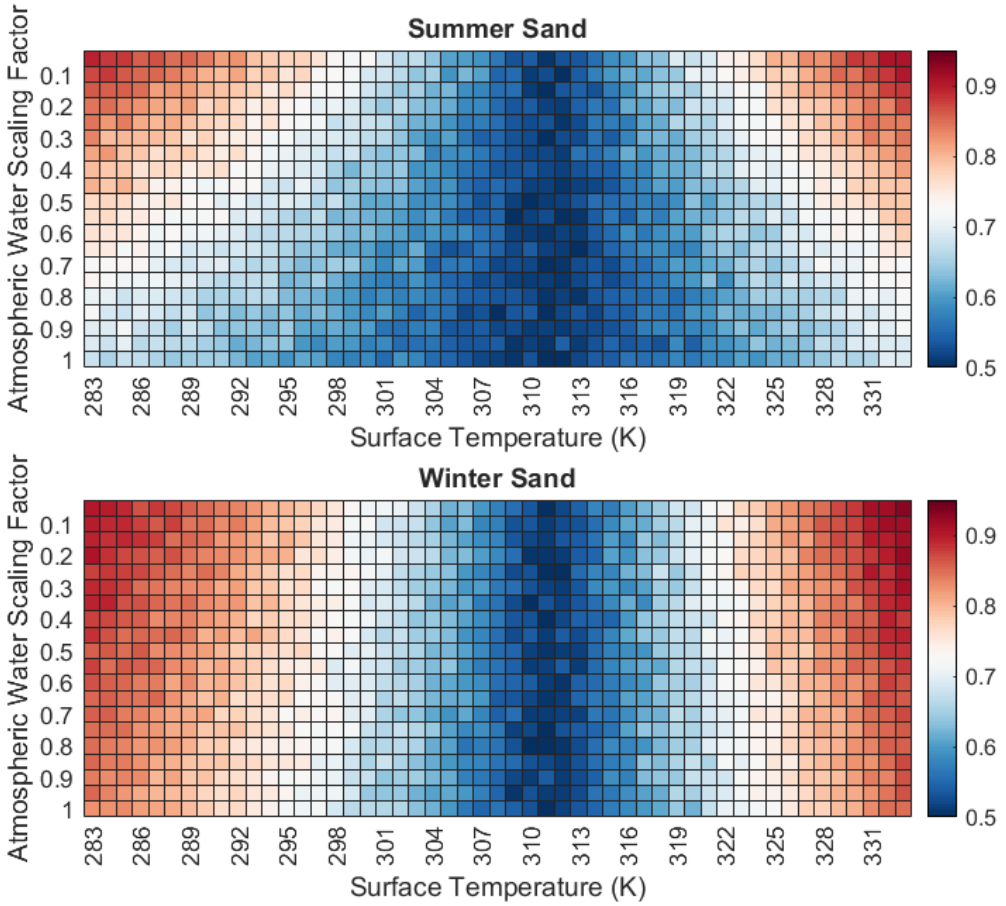

FIGURE 5.26: Fine scaled heat map describing area under ROC curve for NDMI identified enhanced concentration methane plumes pixels. Simulation used: 30ppm plume, ambient temperature (311 K), 20 meter plume thickness, 1.0 noise scaling factor.

noise case. Here we see when the column water vapor is lower than 50% in the summer cases, the method can reliably detect enhanced levels of CH_4 when the plume/surface temperatue contrast is less than about -20 K and greater than +15 K. When using the Winter atmosphere, which contains less column water vapor, the temperature difference required for detection varies from -13 to -20 K and +10 to + 15 K for detection.

In addition to expanding the simulations used in Chapter 3, another scenario was simulated in MODTRAN 6 to test the NDMI approach. This scenario is designed to represent a summer day in Rochester, New York. The simulation uses a user defined atmosphere with the temperature profile replaced with a GEOS-FP temperature profile [22][64] for September 9th, 2019 near the Rochester Institute of Technology, with

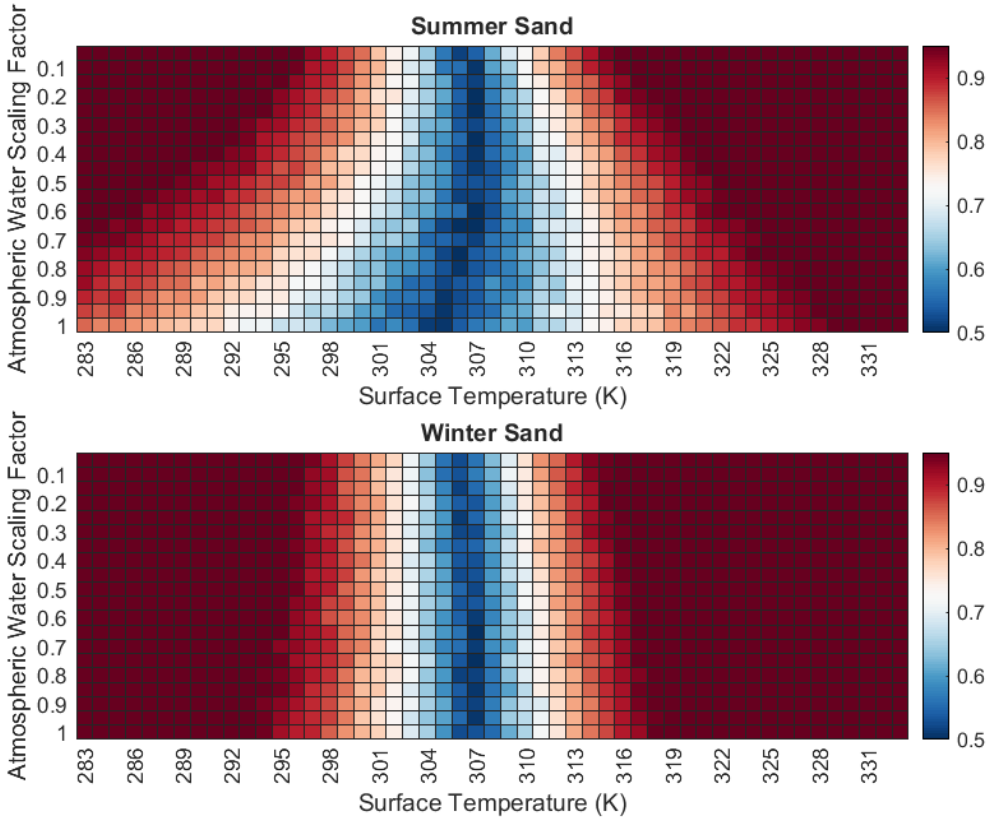

FIGURE 5.27: Fine scaled heat map describing area under ROC curve for NDMI identified enhanced concentration methane plumes pixels. Simulation used: Rochester Temperature Profile, 10ppm plume, +10 K to ambient temperature (306 K), 20 meter plume thickness, 0.4 noise scaling factor.

the bottom layer being replaced with air temperature measurements provided by Weather Underground (https://www.wunderground.com/). The plume is 20 m thick, has a +10 temperature differential with ambient (306.48 K plume to 296.48 ambient temperature at plume height) and is placed at the lowest level of an atmosphere with a CH_4 scaling factor of 0.4. Note, this configuration differs from the others as the plume temperature is higher than ambient temperature at plume altitude. Figure 5.27 shows the results of applying NDMI to this simulated scene.

The heat map again shows the performance of the method is highly dependent on surface temperature and water vapor content. In this scenario, a surface/plume temperature difference of about $\pm$ 6 K leads to a detectable plume when the water vapor content is low. When water vapor content is is high, surface/plume temperature differences of +10 and -15 lead to detectable plumes. While this represents a set

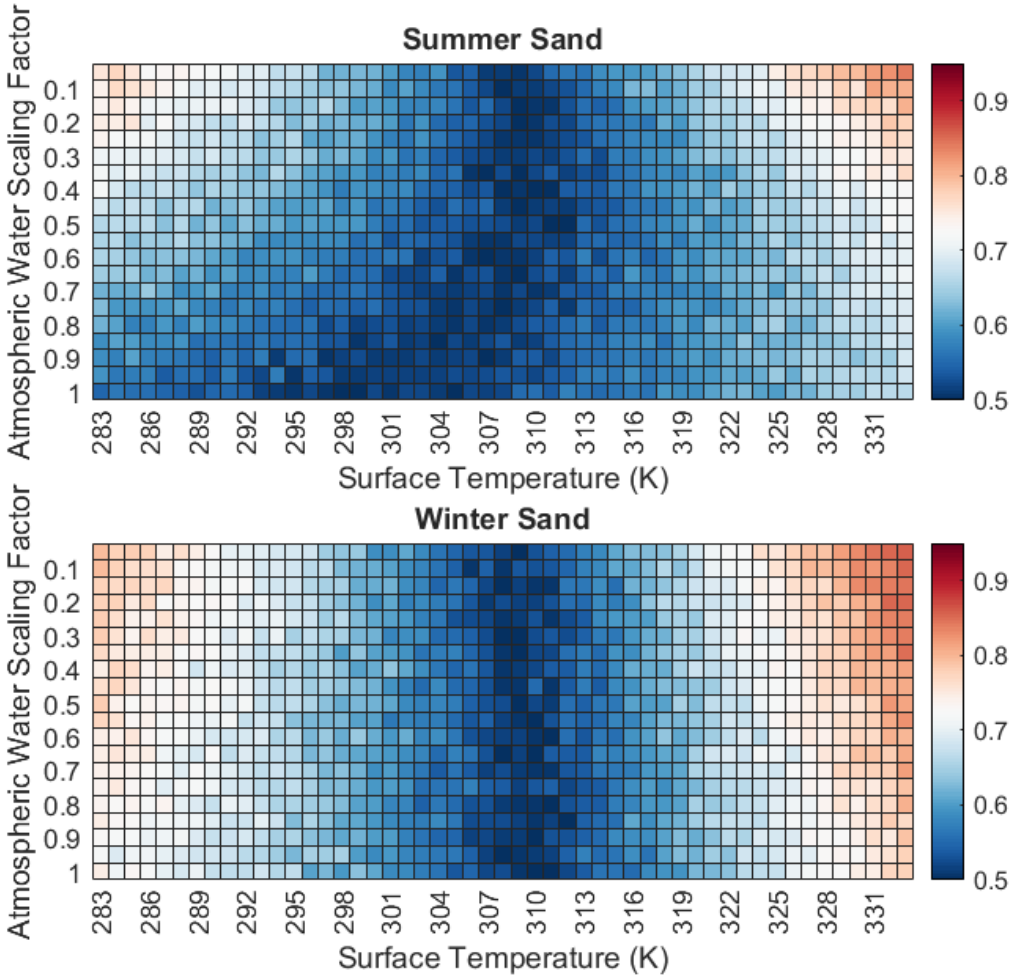

FIGURE 5.28: Fine scaled heat map describing area under ROC curve for NDMI identified enhanced concentration methane plumes pixels. Simulation used: Rochester Temperature Profile, 10ppm plume, +10 K to ambient temperature (306 K), 10 meter plume thickness, 0.4 noise scaling factor.

of cases where detection is possible, Figure 5.28 demonstrates a less than ideal case. In this case, the CH_4 scaling factor has been increased to 1.0 and the plume thickness has been reduced to 10 m.

The increase in background CH_4 and reduction in plume thickness leads to a large decrease in the number of cases where the plume is detectable. Even when the water vapor content is low, a surface temperature difference greater than ± 20 K is needed to identify plume present pixels. When water vapor content is high, no surface temperatures in the range of the dataset provided enough at-sensor radiance difference that makes the NDMI capable of meeting the 0.8 threshold. While

the other configurations serve to identify the capabilities of the method, this configuration helps to highlight the limitations, especially limitations due to column water vapor, surface temperature, and ambient CH_4.

Finally, Figure 5.29 demonstrates a high noise case using the Rochester Temperature Profile. This heatmaps describes the NDMI being applied to a 20 m thick plume of 32 ppm at ambient temperature (296 K) with a CH_4 scaling factor of 0.4 and a noise scaling factor of 1.0. Increasing the noise again requires an increased concentration to detect. From this heatmap we see the high concentration plume is reliably detect when the temperature difference is greater than +15 K, even when the water vapor content is low. When the water vapor content is high, plume/surface temperature differences of greater than +20 K are required for the plume to be reliably detected. While the method has demonstrated the ability to be viable for methane detection, it is demonstrably dependant on system noise.

5.6.6 Multi-Surface Examination

The ROC curves describing the results of the first simulated multi-surface examination can be seen in Figure 5.30. The areas under these curves are recorded in Table 5.12. These results describe the application of NDMI and Matched Filter to a scene with one surface type, sand, that varies slightly in temperature, from 323 K to 328K. From these results, it is clear that the NDMI is highly sensitive to moderate changes in temperature (-5 K between min and max). The NDMI approach is still able to identify enhanced atmospheric CH_4 pixels with satisfactory accuracy in all cases, save for the case where the image is comprised of 50% pixels with surface temperature equal to 328 K and 50% pixels with surface temperature equal to 323 K. In this case, application of the NDMI approach leads to an intensity image where the higher temperature surface results in higher intensity than the lower temperature surface. This means that there is a threshold value that separates the two surfaces, leading to a step in the ROC curve. These results demonstrate that large cool surfaces in an image could cause the NDMI to perform poorly, such as in the case of a thermal shadow. However, application to images created using method S3 and S4 show that the method will still be viable in scenarios where the surface temperature varies, as

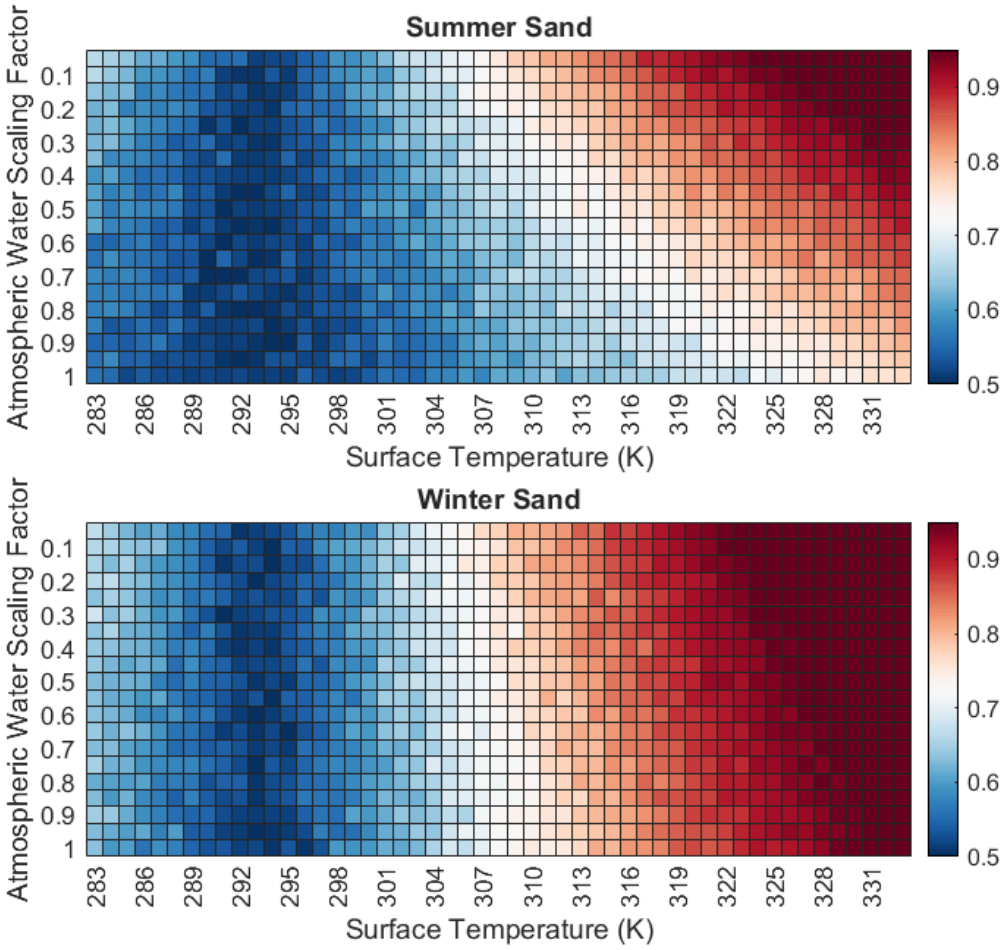

FIGURE 5.29: Fine scaled heat map describing area under ROC curve for NDMI identified enhanced concentration methane plumes pixels. Simulation used: Rochester Temperature Profile, 32ppm plume, ambient temperature (296 K), 20 meter plume thickness, 1.0 noise scaling factor.

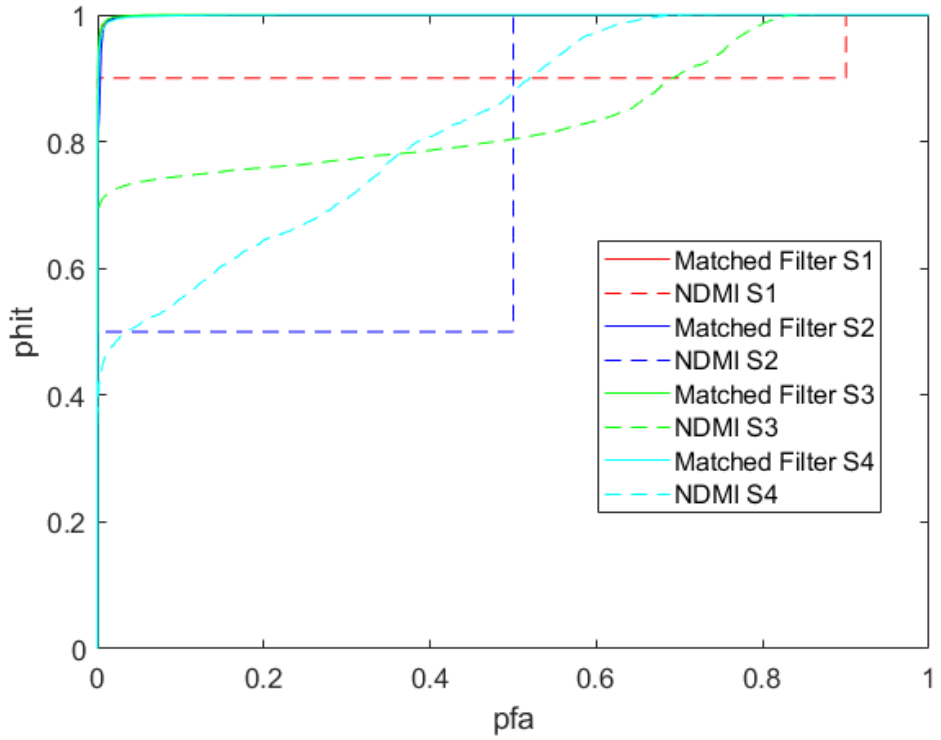

FIGURE 5.30: ROC curves describing performance of NDMI and Matched Filter on multisurface simulated imagery: Sand temperature range: 323-328 K

is likely in real world scenarios. The Matched Filter approach, however, does not experience great loss due to the change in surface temperature.

Figure 5.31 shows the results of applying NDMI and Matched Filter to a scene with one surface type, sand, that varies in temperature, 15K. The area under each of the ROC curves is described in Table 5.13. Again we see that the NDMI is highly sensitive to temperature, to the point that the approach is unable to meet the 0.8 area under the ROC curve standard. Clearly, large variations in surface temperature are

TABLE 5.12: Area under the ROC curves shown in 5.30 describing NDMI and Matched Filter performance when applied to an image with one surface type but varying surface temperature.

Label #	NDMI	Matched Filter
S1	0.910	0.993
S2	0.750	0.999
S3	0.845	1.000
S4	0.830	0.999

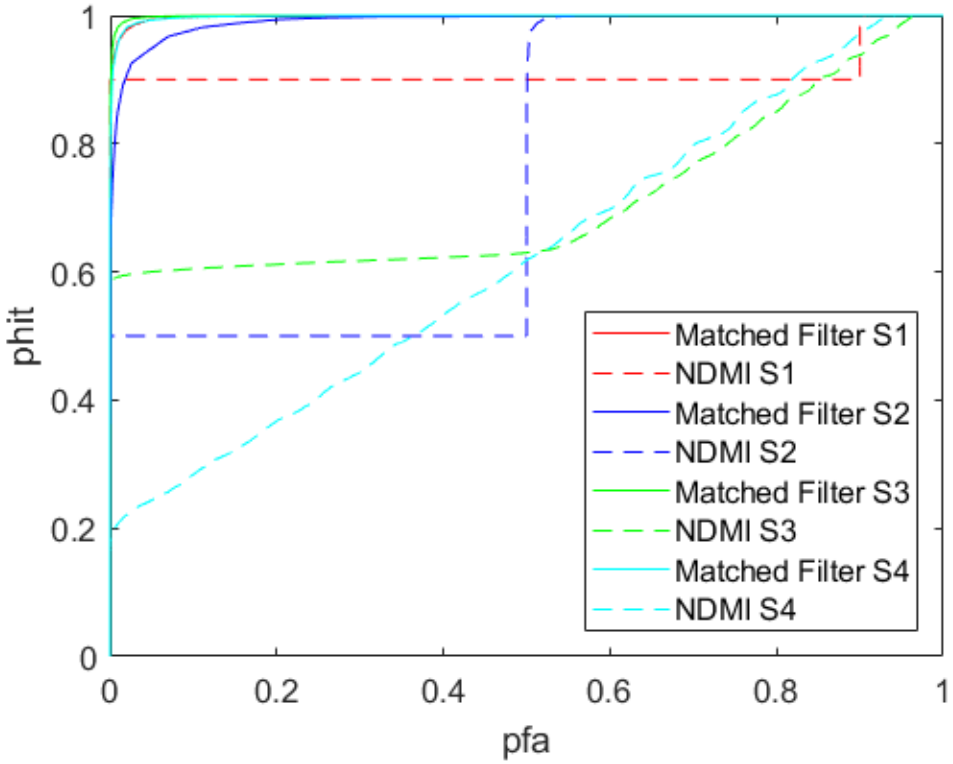

FIGURE 5.31: ROC curves describing performance of NDMI and Matched Filter performance when applied to an image with one surface type but varying surface temperature. Sand temperature range: 315-330 K

likely to mask the plume when using the NDMI approach. However, when the large changes in temperature only correspond to 10 % of the image, they have a marginal effect on the success of the approach. Again, the Matched Filter approach does not experience much loss due to change in surface temperature.

Figure 5.32 shows the application of the NDMI and Matched filter on a dataset that utilizes two different surface emissivities. For this examination, the first surface is defined as sand and the second is defined as an urban pixel. Both surfaces are set to be 325 K. The areas under the ROC curves are detailed in Table 5.14. We see in this instance that the NDMI approach is sensitive to changes in surface emissivity. If the surface emissivity changes are limited to 10% of the image, it has little effect on the success of the approach, but it will fail to identify plume present pixels in the area with different emissivity. The Matched Filter approach shows little change due to the change in surface emissivity.

Figure 5.33 shows the ROC curves that describe the performance of applying the

TABLE 5.13: Area under the ROC curves shown in 5.31 describing NDMI and Matched Filter performance when applied to an image with one surface type but varying surface temperature.

Label #	NDMI	Matched Filter
S1	0.910	0.998
S2	0.749	0.986
S3	0.712	0.999
S4	0.620	0.998

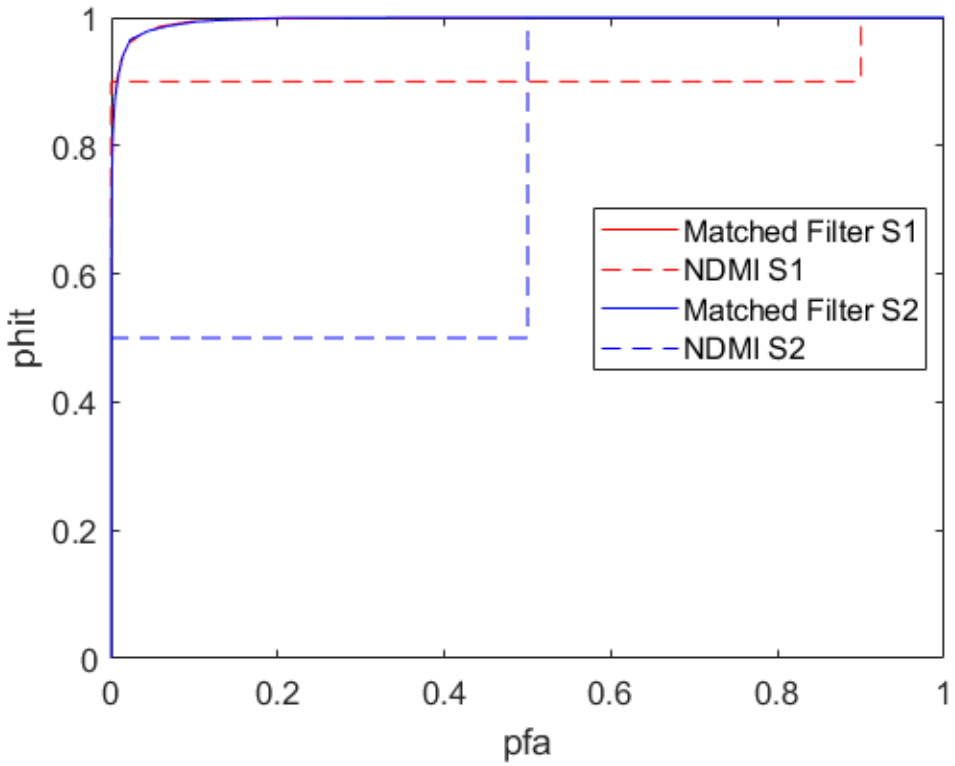

FIGURE 5.32: ROC curves describing performance of NDMI and Matched Filter performance when applied to an image with two different surface types (sand and urban) at the same temperature (325 K)

TABLE 5.14: Area under the ROC curves shown in 5.32 describing NDMI and Matched Filter performance when applied to an image two different surface types (sand and urban) at the same temperature (325 K)

Label #	NDMI	Matched Filter
S1	0.910	0.996
S2	0.750	0.996

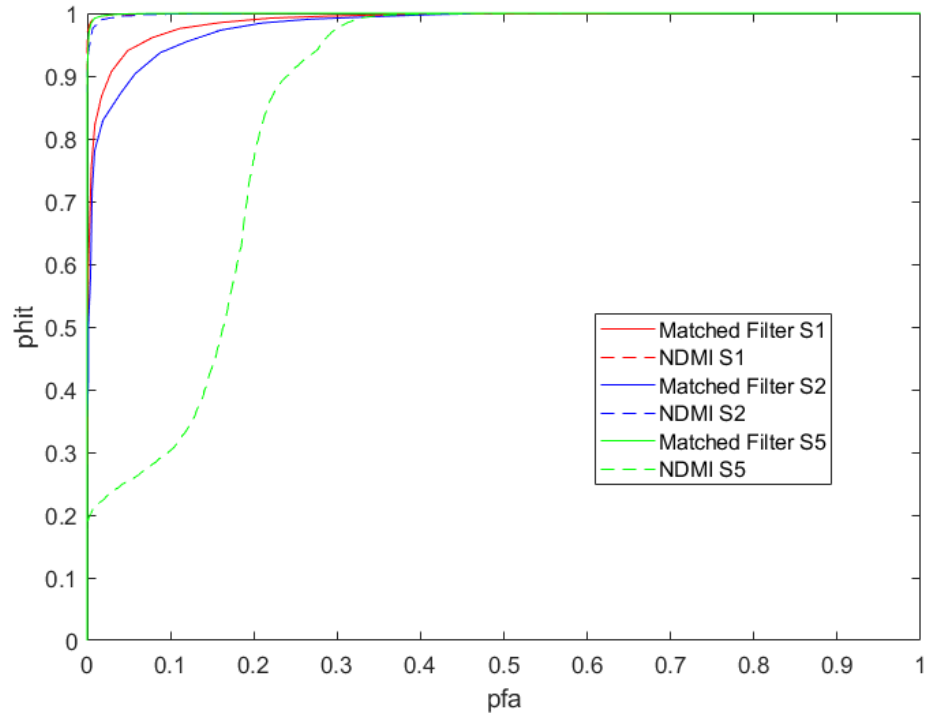

FIGURE 5.33: ROC curves describing performance of NDMI and Matched Filter performance when applied to a simulated image with two different surface types (sand and urban) at varying temperatures (320-325K)

NDMI and Matched Fitler to a simulated image that includes sand and urban pixels, where the urban pixels vary in temperature from 320 - 325 K. Table 5.15 details the area under the ROC curves. In this case, the NDMI approach is not sensitive to the change in surface temperature and emissivity. This is likely due to the relatively lower emissivity value of sand compared to the MODTRAN defined urban pixel. The Matched Filter approach does see a slight dip in performance when applied to S1 and S2 images, but the approach still performs above the 0.8 area under the ROC curve threshold.

Finally, Figure 5.34 displays the results of applying NDMI and Matched Filter to a simulated image with two surface types, sand and grass, where the grass pixels vary in temperature from 300 K to 325 K. Table 5.16 details the area under each of the ROC curves shown in Figure 5.34. Results here show a situation in which NDMI is likely to fail: different surface emissivities and high surface temperature variation. While the Matched Filter does see a drop in performance, the drop does not cause

TABLE 5.15: Area under the ROC curves shown in 5.33 describing NDMI and Matched Filter performance when applied to an image two different surface types (sand and urban) at varying temperatures (320-325K)

Label #	NDMI	Matched Filter
S1	1.0	0.987
S2	0.999	0.984
S5	0.8628	1.000

TABLE 5.16: Area under the ROC curves shown in 5.34 describing NDMI and Matched Filter performance when applied to an image two different surface types (sand and grass) at varying temperatures (300-325K)

Label #	NDMI	Matched Filter
S1	0.906	0.982
S2	0.646	0.856
S5	0.671	0.976

the approach to fall below the 0.8 area under the ROC curve threshold.

From this investigation, it is clear the matched filter is likely to outperform the NDMI method in most scenarios involving large surface variations in emissivity and temperature. However, given cases with relatively homogeneous surface type, such as the Kern Valley image shown in Figure 5.16, the NDMI approach is a viable method for identifying likely locations of enhanced levels of atmospheric CH_4.

5.7 Improving Detection of Enhanced Levels of Atmospheric CH_4: MURI+

While the MURI system has demonstrated the ability to identify the location of enhanced levels of atmospheric CH_4 with a single band allocated to CH_4 absorption features, the inclusion of additional bands would serve to improve detection. This section describes the definition of a novel system, based upon MURI's design, that would show improved performance in CH_4 detection.

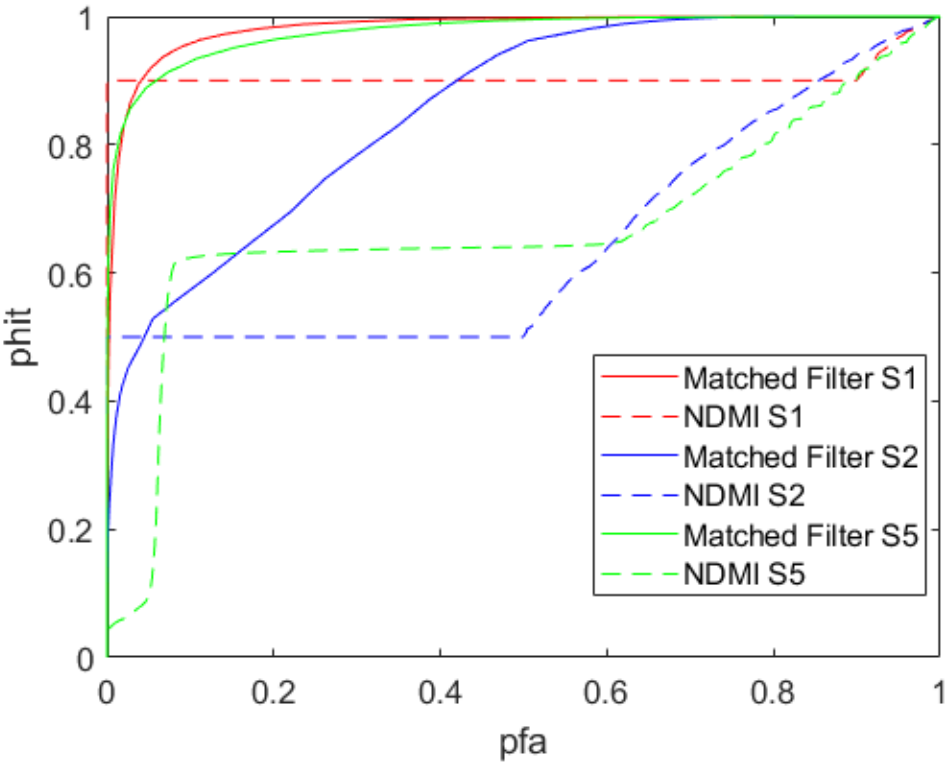

FIGURE 5.34: ROC curves describing performance of NDMI and Matched Filter performance when applied to a simulated image with two different surface types (sand and grass) at varying temperatures (300-325K)

5.7.1 MURI+ Design

A novel system, referred to here as MURI+, was designed to improve detection of enhanced atmospheric CH_4 using more than one band allocated to CH_4 absorption features. MURI+ was designed using the same focal plane array and optics as the MURI airborned demonstration instrument, but with additional bands overlapping with CH_4 absorption features. The band allocations for MURI+ are described in Table 5.17.

TABLE 5.17: MURI+ Band Allocations and Predicted Noise Equivalent delta Temperature

Band #	Center Wavelength	Band Width	Predicted NEdT
B1	7.46μm	0.18μm	0.167K
B2	7.68μm	0.05 μm	0.338K
B3	7.83μm	0.10μm	0.256K
B4	8.55μm	0.35μm	0.076K
B5	9.07μm	0.36μm	0.078K
B6	10.05μm	0.54μm	0.059K
B7	10.90μm	0.59μm	0.061K
B8	12.05μm	1.01μm	0.036K

MURI+ bands 4 through 8 match the band allocation of bands 2 through 6 of the MURI instrument. MURI+ band 2 shares a band center with MURI band 1, however the bandwidth is narrowed to 0.05 μm to increase contrast between on and off CH_4 plume pixels. MURI+ bands 1 and 3 are allocated to overlap with a collection of CH_4 absorption features around 7.46 and 7.83 μm respectively.

As shown throughout this chapter, there are multiple factors that determine if an enhanced level of atmospheric methane is detectable by a system. In order to determine that MURI+ was outperforming MURI in CH_4 detection, MURI+ had to demonstrate the ability to detect CH_4 in scenarios where MURI was not able to. In order to meet the definition of improving upon MURI's CH_4 detection, MURI+ had to meet at least one of the following criteria: 1. MURI+ is capable of detecting lower levels of atmospheric CH_4 than MURI, 2. detection using MURI+ is less sensitive to column water vapor, 3. the required temperature contrast between surface and plume for successful detection of a CH_4 plume is lower for MURI+ compared to MURI.

A combination of approaches were selected to demonstrate the performance of MURI+ compared to MURI. First, a single pixel NEdT examination was performed to investigate the brightness temperature contrast between an off and on plume pixel for each of the MURI+ methane bands. Second, a coarse controlled concentration experiment was performed using the same methods described in section 5.6. However, in this examination a match filter was used in place of the NDMI, as the clutter matched filter will utilize the new MURI+ bands while the NDMI is by definition a two band approach.

5.7.2 Single Pixel NEdT Examination Description

The first study presented here on MURI+ investigates the potential contrast for each of the thermal infrared spectral bands centered on their respective CH_4 absorption features. Similar to the study presented in Chapter 3, the goal of the study is to determine under what scenarios each band is capable of detecting the temperature difference indicative of an enhanced level of atmospheric CH_4. The dataset used for this investigation is the same as the dataset described in Chapter 3 Section 3 Subsection 1. Table 5.18 describes the MODTRAN parameters used in creating the simulated dataset. As described in Chapter 3, these parameters were derived from examining HyTES images, metadata, and the conditions under which the images were recorded [56]. Ambient atmospheric temperature was estimated from Weather Underground which was recorded by the Meadows Field Station in Bakersfield, California on July 8th, 2014 at 11:54 am.

TABLE 5.18: NEdT Single Pixel Study MODTRAN Parameter Settings

Constant	Value
Atmosphere	Midlatitude Summer
Water Vapor Scaling Factor	0.10
Collection Height	4.572km (15000 feet)
Emitting Surface Temperature	328 K
Plume Thickness	20 m
Surface Emissivity	LAMB_SANDY_LOAM
Plume Base Altitude	10 m
Ambient Temperature at Plume Altitude	311 K

5.7.3 Single Pixel NEdT Study Results

Figure 5.35 shows the comparison of brightness temperature difference to NEdT for each of the MURI+ methane bands. The plume for this study varied from - 10 K to +10 K of ambient temperature at the plume height. This is a range of -27 to -7 K to the background surface. This figure demonstrates where the brightness temperature contrast between an on plume and off plume case is high enough to be detectable by each band. For MURI+ band 2, which is allocated around the same methane absorption feature as MURI, a plume at ambient temperature at plume height of less than 10 ppm will lead to a detectable brightness temperature contrast. MURI+ band 1 results are similar, with a plume of about 10 ppm above background levels at ambeint temperature creating a detectable contrast. MURI+ band 3 shows less brightness temperature contrast, with a plume at ambient temperature requiring a concentration of about 15 ppm to be detectable. Both MURI+ band 1 and 2 can detect lower concentrations of enhanced atmospheric methane compared to MURI band 1, while MURI+ band 3 has detectable scenarios similar to MURI band 1.

5.7.4 Matched Filter Methane Detection with MURI+ vs MURI Dataset Description

The data for this examination was produced using the same approaches described in 5.6.2. A description of the parameters held constant for this investigation can be seen in Table 5.19, while a description of the parameters which were varied is detailed in Table 5.20. The considered scenario is based on the scene described in Chapter 3,section 5.6.2, and shown in Figure 5.16.

TABLE 5.19: MODTRAN parameters held constant for the MURI+ matched filter evaluation

Parameter	Value
Collection Height	4.572km (15000 feet)
Ambient Temperature at Plume Altitude	311 K
Plume Distance from Surface	0 m
Plume Thickness	20 m
Plume/Ambient Temperature Difference	0
CH_4 Scaling Factor	0.4
Surface Emissivity	SANDY_LOAM

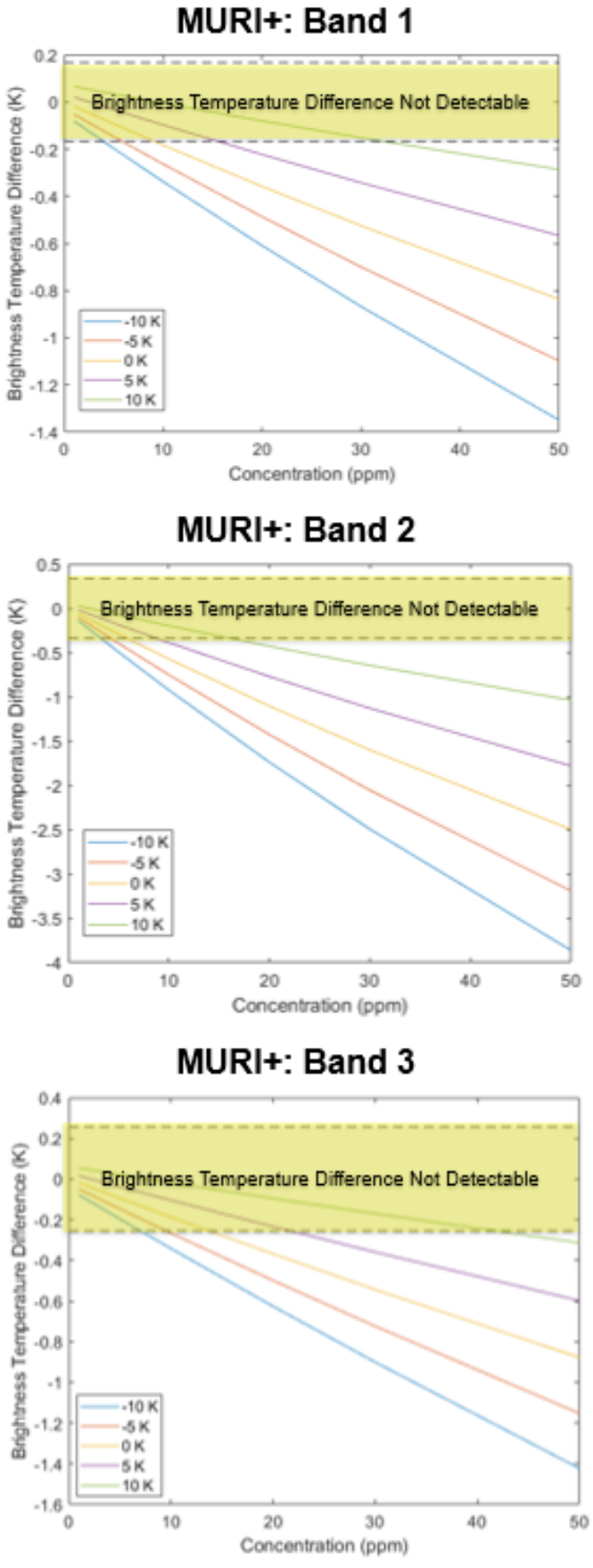

FIGURE 5.35: Low altitude plume model results displaying brightness temperature as a function of plume concentration for MURI+ three methane bands. Figure identifies detectable and undetectable scenarios for MURI's predicted NEdT.

TABLE 5.20: MODTRAN parameters and the respective values used in the MURI+ matched filter evaluation.

Model Input	Value
Atmosphere	MIDLAT SUMMER, MIDLAT WINTER
Water Vapor Scaling Factor	0.1 - 1.0
Surface Temperature	273.15 - 333.15
Plume Concentration	15, 20 ppm
Noise Scaling Factor	0.8, 1.0

The matched filter for each system was calculated as described in Chapter 3 and applied to the dataset described above to produce heatmaps similar to the heatmaps described in section 5.6. Again, the threshold for successful detection is defined as an area beneath the ROC curve of 0.8 or higher.

5.7.5 Matched Filter Methane Detection with MURI+ vs MURI Results

Figure 5.36 shows a comparison between the MURI and MURI+ systems when applied to an identical dataset. The selected scene is a 20 ppm plume at ambient temperature, with a noise scaling factor of 1. The heatmaps show that the MURI+ system improves detection across both surface temperature and column water vapor when compared to MURI's matched filter performance. While MURI's detection range is limited, utilizing MURI+'s band allocation, with no change in MURI's noise characteristics, leads to a 60% increase in detectable cases for this set of heatmaps.

The same scenario is demonstrated again in Figure 5.37, this time however, the noise is reduced for each system by 20%. Again we see the MURI+ system outperforming MURI, and the reduction in noise means additional cases are detectable. With just a 20% reduction in noise, MURI+ is capable of detecting a 20ppm with a temperature difference as low as about 10 K, given a low amount of column water vapor.

Finally, Figure 5.38 and 5.39 show the same scene, but with a plume of concentration 15 ppm with a noise scaling factor of 1 and 0.8 respectively. When the noise scaling factor is equal to 1, the MURI system does not meet the 0.8 area under the ROC curve threshold for any cases, though it comes close with the most extreme cases. In contrast, MURI+ is capable of detecting the 15 ppm in 7 of the 41 cases.

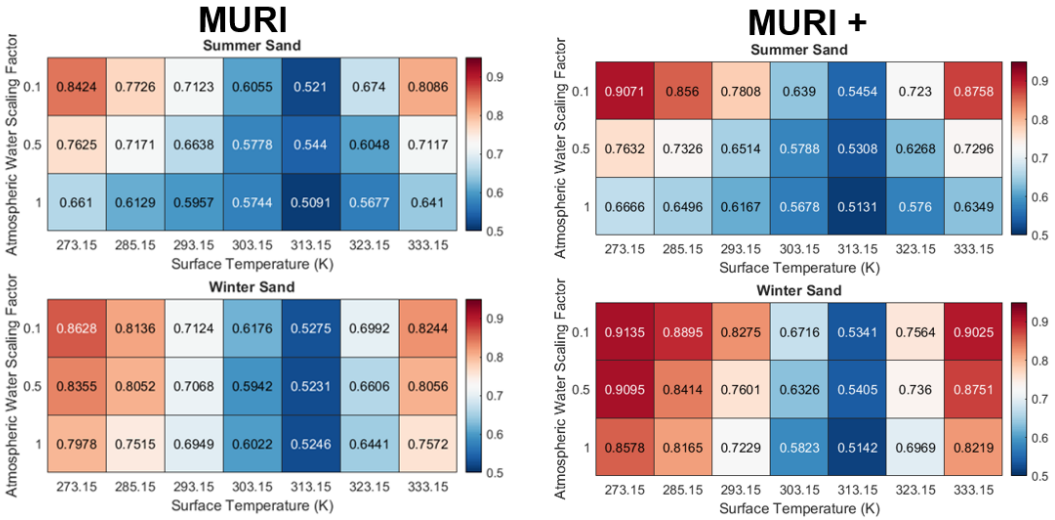

FIGURE 5.36: Heat map describing area under ROC curve for MURI+ and MURI matched filter identified enhanced concentration methane plumes pixels. Simulation used: 20ppm plume, ambient temperature (311 K), 20 meter plume thickness, noise scaling factor: 1.

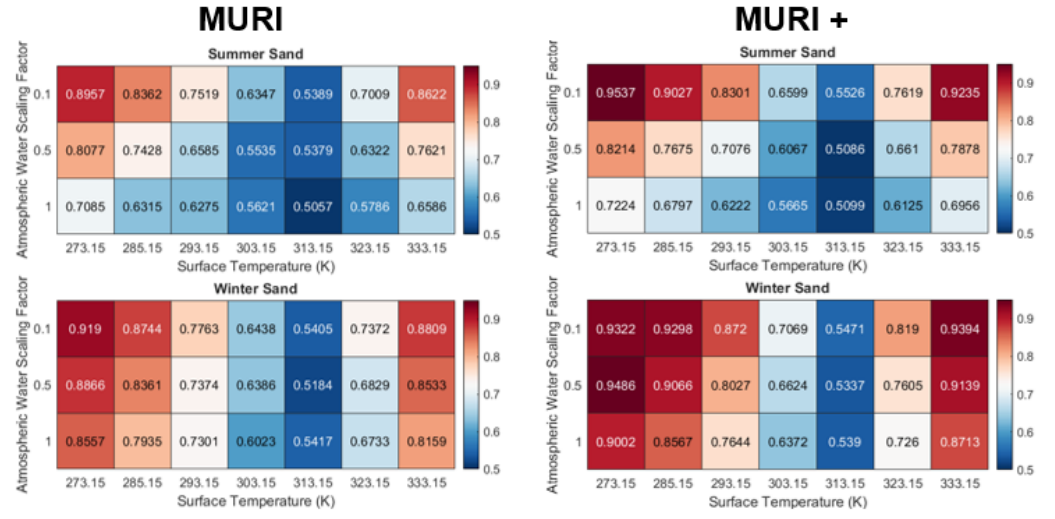

FIGURE 5.37: Heat map describing area under ROC curve for MURI+ and MURI matched filter identified enhanced concentration methane plumes pixels. Simulation used: 20ppm plume, ambient temperature (311 K), 20 meter plume thickness, noise scaling factor: 0.8.

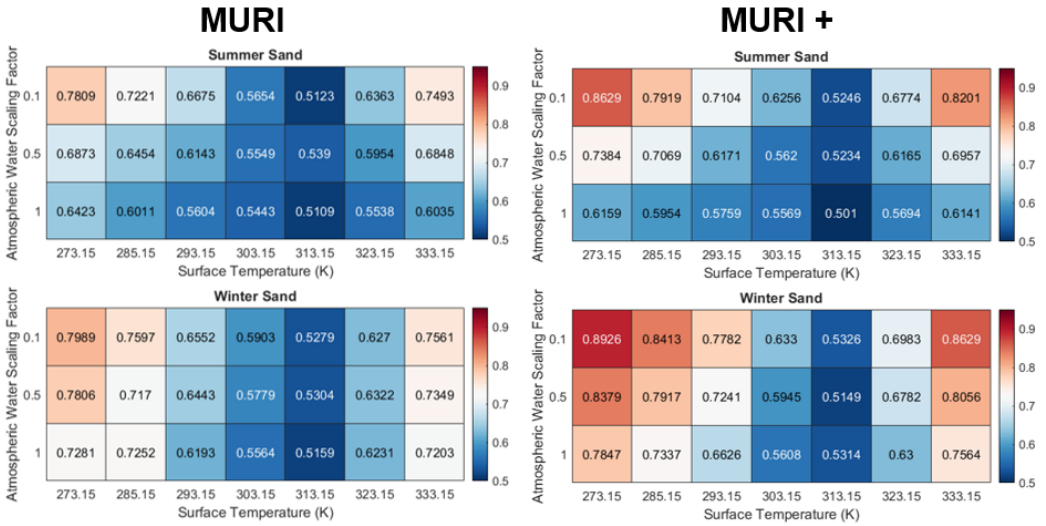

FIGURE 5.38: Heat map describing area under ROC curve for MURI+ and MURI matched filter identified enhanced concentration methane plumes pixels. Simulation used: 15ppm plume, ambient temperature (311 K), 20 meter plume thickness, noise scaling factor: 1.0.

When the noise scaling factor is reduced to 0.8, both systems see an increase in the number of detectable cases. However, MURI+ is now able to successfully identify pixels with enhanced levels of atmospheric methane in twice the number of cases as MURI. From this, it is clear that MURI+ is capable of successfully identifying pixels with lower concentration plumes of methane present when compared to MURI.

5.8 Conclusions

Several approaches to validating the MURI system and the NDMI approach were discussed. Application of the Matched Filter approach and NDMI to MURI imagery synthesized from HyTES data demonstrated the viability of the approaches in detecting enhanced levels of atmospheric methane in multispectal airborne instrument data. The comparison study between data simulated with MODTRAN6 and Spectral Calc served to validate the models being produced for this investigation, in lieu of data collected with MURI or a higher spectral resolution instrument. Results show that the models are in high agreement, especially when the concentration of the plume is low. The models created similar brightness temperature differences after MURI's spectral response was applied, further validating the models which were

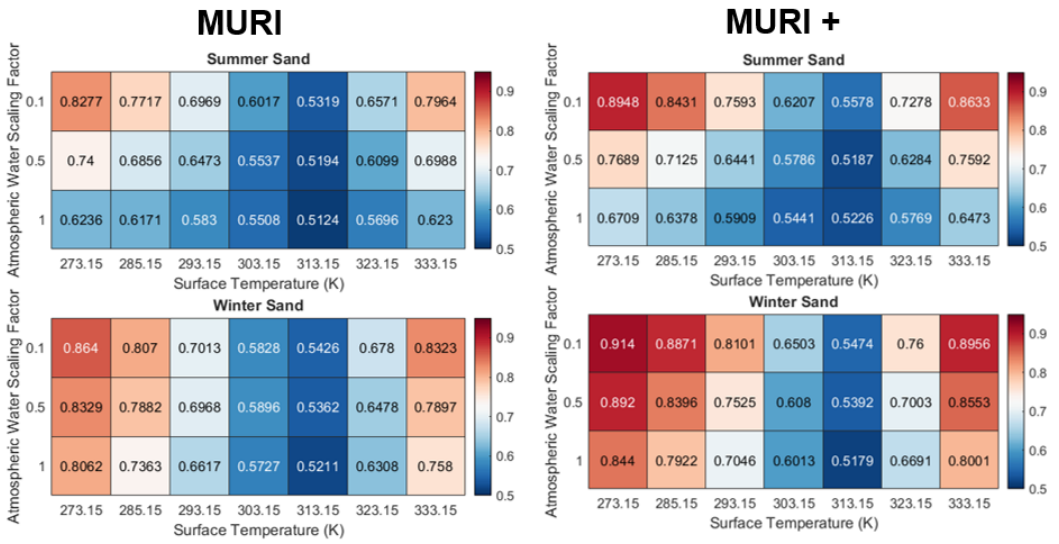

FIGURE 5.39: Heat map describing area under ROC curve for MURI+ and MURI matched filter identified enhanced concentration methane plumes pixels. Simulation used: 15ppm plume, ambient temperature (311 K), 20 meter plume thickness, noise scaling factor: 0.8.

used to test the extent of the NDMI approach.

The simulated controlled concentration experiment described the extent and limitations of the NDMI approach. Results demonstrate the sensitivity of the approach to surface temperature, column water vapor, and ambient methane quantity. The study demonstrated that the method is consistent across a selection of different surface types. Through the coarse evaluation we demonstrated scenarios where a relatively low concentration plume (7 ppm above ambient) at ambient temperature are highly detectable over surfaces that are 10 K hotter than ambient when system noise is low. We also detailed scenarios where a plume of 10 ppm above ambient and -10 K to ambient is not detectable above a surface that is 30 K cooler than the plume. Furthermore, the Matched Filter demonstrated stable performance over surfaces of varying emissivity and temperature, while the NDMI method demonstrated high sensitivity to emissivity and temperature. However, the NDMI approach remains a viable option for detection of enhanced levels of atmospheric CH_4 utilizing only two spectral bands. The high performance of the Matched Filter and the moderate performance of the NDMI provides evidence that methane detection with a system with only one spectral channel dedicated to CH_4 features is viable.

Finally, the matched filter study demonstrated that the proposed novel system

MURI+ outperforms MURI in identifying pixels with enhanced levels of atmospheric methane. The MURI+ system demonstrated the ability to detect lower concentrations of CH_4 and scenarios where the plume/surface temperature contrast was smaller. While the MURI+ matched filter approach is still sensitive to column water vapor, the system was capable of identifying enhanced CH_4 plumes in cases where the MURI system was thwarted by column water vapor. While the MURI system has demonstrated viability in detecting CH_4 plumes with only a single spectral channel allocated to CH_4 features, MURI+ demonstrates the value additional bands bring to the application.

Chapter 6

Inflight Performance of the Multiband Uncooled Radiometer Imager Instrument.

6.1 Introduction

6.1.1 Context for Inflight Performance Assessment

From August to October of 2019, test flights of the MURI instrument were performed to validate the MURI instrument's data collection capability as well as its ability to retrieve surface temperature. The first set of test flights took place from August 28^{th} to September 4^{th} in Southern California, and the second set were performed from October 2^{nd} to October 7^{th} around Southern California as well as the Bay Area. These flights were designed to overlap with passovers from Landsat 8, in order to examine MURI's system performance compared to an established system.

The MURI instrument was mounted aboard a Twin Otter aircraft which departed from Los Alamitos Joint Forces Training Base in Los Alamitos, California. During flights, ground teams set up targets and collected surface temperatures and emissivities for reference. Additional measurements were retrieved from buoys positioned off the coast of Southern California and deployed in both Sultan Sea and Lake Tahoe. Post flight, edge targets were identified in order to determine MURI's inflight spatial performance.

6.2 Validation Experimental Setup

6.2.1 Testflight Surface Targets

Four different target types were chosen for this validation: water, sand, rubber, roof, and pavement. Natural water targets were chosen based off measurement accessibility and included two stretches of ocean that coincided with Landsat overpasses and the location of NOAA nearshore temperature monitoring buoys. Additionally, temperature measurements were recorded from buoys in Lake Tahoe and Salton Sea [6][19][44][79]. It is important to note that the temperatures reported from the buoys and used in this investigation were defined as Bulk temperatures, not skin temperatures. This could lead to some error when used in comparison with MURI's temperature retrieval, as Bulk temperatures are not necessarily identical to the surface or skin temperature. For example, the buoys at Lake Tahoe have demonstrated daytime skin temperatures 0.5 K higher than reported bulk temperature on average, and this difference changes based on downwelling radiance, time of day, and wind speed [101].

The last of the natural water body measurements were recorded over the ponds El Dorado East Regional Park in Long Beach, California. Reference temperature measurements were recorded from the El Dorado Park ponds using the DIRS Boat for Land Assisted Surveying of Temperature or DIRS BLAST. The BLAST was created by attaching a Hobo TidBit temperature logger to a Traxxis remote controlled boat [68]. The BLAST allowed the ground research team the ability to measure water temperature from the interior of the lake without having to leave the shore.

Five man made water targets were chosen within the vicinity of Los Alamitos Joint Forces Training Base. The first of these targets was the Olympic sized swimming pool of the Aquatics Training Center (ATC) located on the Joint Forces Training Base. The pools size, temperature regulation, accessibility, and location within the flightline was ideal for the validation. The ATC pool, as well as the pool and hot tub located at the Residence Inn by Marriott Cypress Los Alamitos were monitored using TidBit temperature loggers during the flights [68]. Finally, two inflatable swimming pools with 10 foot diameters were setup in the parking lot of DRS Leonardo. One pool, shown in Figure 6.1 below, had ice added before the flight to

FIGURE 6.1: Diagram of experimental setup for DRS scene for August/September 2019 test flights.

reduce temperature. The second pool, designated as the warm pool, had buckets of water that were heated added before the flight to raise temperature. Erecting the cool and warm pool in the same vicinity allows for a temperature differential in the same image. For the El Dorado ponds and the man made targets, there was an attempt to measure the temperature as close to the surface as possible, however all measurements were made at a depth to ensure the tidbits were fully submerged. As the skin layer of water is less than a millimeter thick [101], these reference measurements may also experience error similar to the bulk temperatures provided from the buoy data.

Additional targets were setup within flight lines in order to differentiate surface types within the same image. A sand target was setup in the same parking lot as the two pools, and a section of the parking lot was marked off to serve as a pavement target. A rubber target was deployed on the roof of the DRS Leonardo building and a section of the roof was marked off to serve as a roof material target. The emissivities of the other surfaces were calculated from measurements recorded on site on August 28^{th}, 2019 using the Model 102 Hand Portable FT-IR Spectrometer from D&P Instruments [2] [43][63] [75][76]. In order to locate additional targets, highly reflective emergency blankets were deployed a meter away from each of the targets. These emergency blankets are easily spotted in the imagery, appearing as cold or dark objects. A diagram of the DRS scene is shown in Fig. 6.1.

FIGURE 6.2: Location of proposed location for 2019 target assessment and deployment. This experiment was cancelled when the team was not granted access to the base.

Unfortunately, during the first testflights the system did not stabilize before images were recorded over the DRS parking lot targets. In an attempt to ensure a non-water target was still in a usable scene, an additional rubber mat target was deployed near the large pond at El Dorado East Regional Park. During the second round of test flights, performed in October of 2019, a rubber mat, a cold water pool, and a pavement patch were deployed near the large pond at El Dorado East regional park. Unfortunately, the cold water pool and the rubber mat were obscured during the flight. This imagery was still used in water body temperature retrieval.

The original version of this experiment was designed to take place at the Los Alamitos Joint Forces Training Base. Targets were to be deployed on the West side of the airstrip parking area, which can be seen in Figure 6.2. Measurements of surface emissivities of local targets were to be recorded with the Model 102 Hand Portable FT-IR Spectrometer from D&P Instruments including the emissivity of the concrete. However, during the 2019 testflights the team was not granted approval to perform their experiments on the base. This experiment was performed during 2020 testflights, the evaluation of which is beyond the scope of this thesis.

The examinations presented here will focus on the temperature and emissivity retrieval of the waterbody datasets. Water is an ideal target for surface temperature

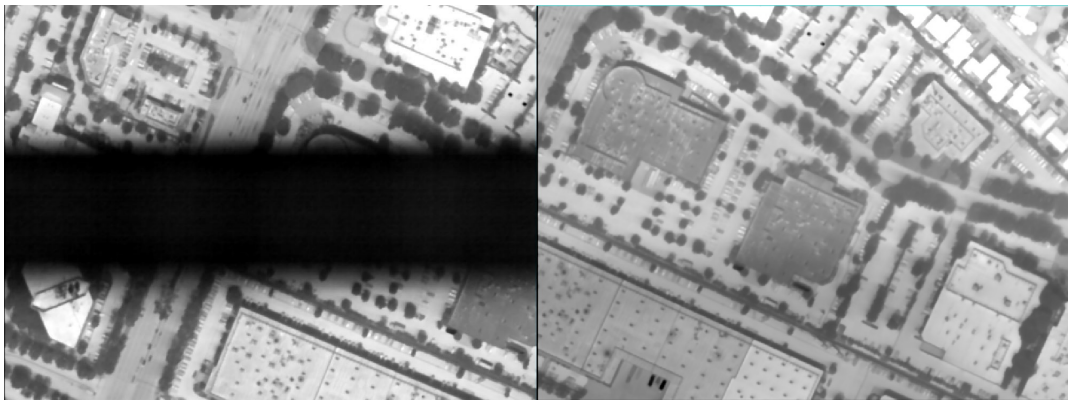

FIGURE 6.3: Two images recorded using the MURI instrument over DRS Leonardo building on August 29^{th}, 2019. The image on the left is from Tam 2, the top band is MURI band 5, the middle band is band 1, and bottom is band 3. The right image was recorded on Tam 4, the top band is MURI band 4, the middle is band 2, and the bottom is band 6.

validation due to its spectrally stable emissivity and high thermal inertia [61].

6.2.2 MURI Testflight Waterbody Dataset Description

Data from a selection of targets were provided by DRS in 14 frame stacks of digital counts. The data, an example of which can be seen in Fig. 6.3, is a direct stack of digital counts from the output of the system and is therefore still separated into three strips corresponding to the three bands on each Tam. DRS also provided a black body temperature to digital conversion file, which was used to derive a set of equations to calculate brightness temperature from digital counts for each band on each Tam.

Additionally, DRS provided brightness temperatures for select targets from the three testflight locations: Cypress, CA, Sulton Sea, CA, and Lake Tahoe, CA. The targets are listed in Table 6.1 and shown in Fig. 6.4 and Fig. 6.5. Overlapping Landsat8 TIRS dates are also described in Table 6.1.

Finally, DRS provided two stitched images recorded over Cypress/Los Alamitos on October 4^{th}, 2019. These data were recorded over the Los Alamitos Joint Forces Training Base pool and the large pond in El Dorado East Regional Park. Subsets of these images can be seen in Figure 6.6. This dataset consists of unregistered images of MURI bands 2 - 5 in digital counts. Target measurements were converted from digital counts to brightness temperature by taking a region of interest over the

FIGURE 6.4: In-land water body targets from the 2019 testflights performed in September and October of 2019. Left: Target locations from around Cypress/Los Alamitos California including El Dorado park ponds, Joint Forces Training Base Pool, Residence Inn by Marriott Pool and Spa. Top Right: Lake Tahoe. Bottom Right: Salton Sea.

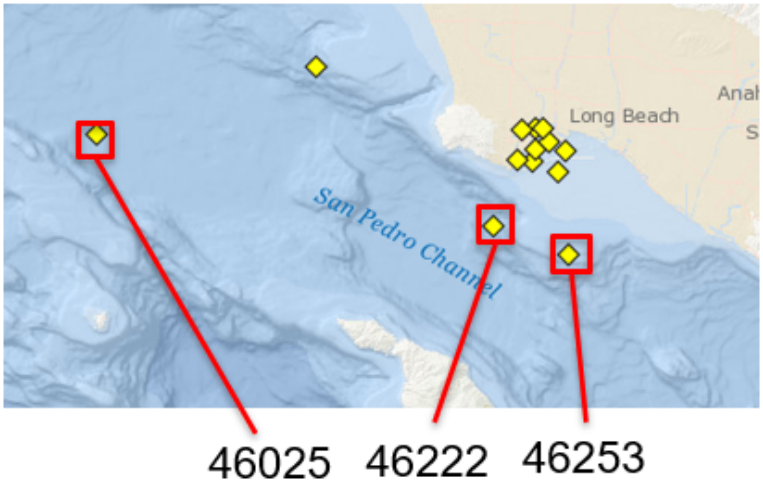

FIGURE 6.5: NOAA nearshore buoy targets near Long Beach, CA used to retrieve reference temperature measurements. Map image retrieved from National Buoy Center website [19]

TABLE 6.1: 2019 testflight data description. Landsat8 TIRS target overlaps identified for use in Split Window comparison.

Date	MURI Targets	Landsat TIRS Targets
9/3	Buoy 46253	Buoy 46253
9/4	Buoy 46222, Res. Inn, JFTB, El Dorado	-
9/5	Salton Sea	Salton Sea
10/3	Lake Tahoe	Lake Tahoe
10/4	Buoy 46253	-
10/5	Buoy 46025, 46222	Buoy 46025, 46222
10/7	Salton Sea	Salton Sea

target and applying the calibration curves provided by DRS. As the images are unregistered, the ROIs for each band had to be independently defined. The ROI for the JFTB pool was identified by picking pixels away from the edge of the pool. The ROI for the El Dorado image was identified by picking pixels from the center of the pond, around the area where the DIRS BLAST was deployed to record the water temperature. The number of pixels per ROI for each band are listed in Table 6.2.

TABLE 6.2: ROI pixel counts for each unregistered MURI image from the October 4^{th}, 2019 dataset.

MURI Band	El Dorado Pixel Count	JFTB Pool Pixel Count
2	25551	2457
3	25584	1979
4	22218	2198
5	23680	1985
6	30728	2182

6.3 MURI Instrument Validation Approach

A simple approach to validating the data collected by MURI during the first test flight was adopted. This approach utilizes atmospheric modeling and emissivity measurements to determine ground temperature from the MURI data. The results of this method are compared to recorded ground reference measurements to determine MURI's measurement accuracy.

The approach utilizes the radiometric equation that describes the primary contributors for sensor reaching radiance in the thermal infrared:

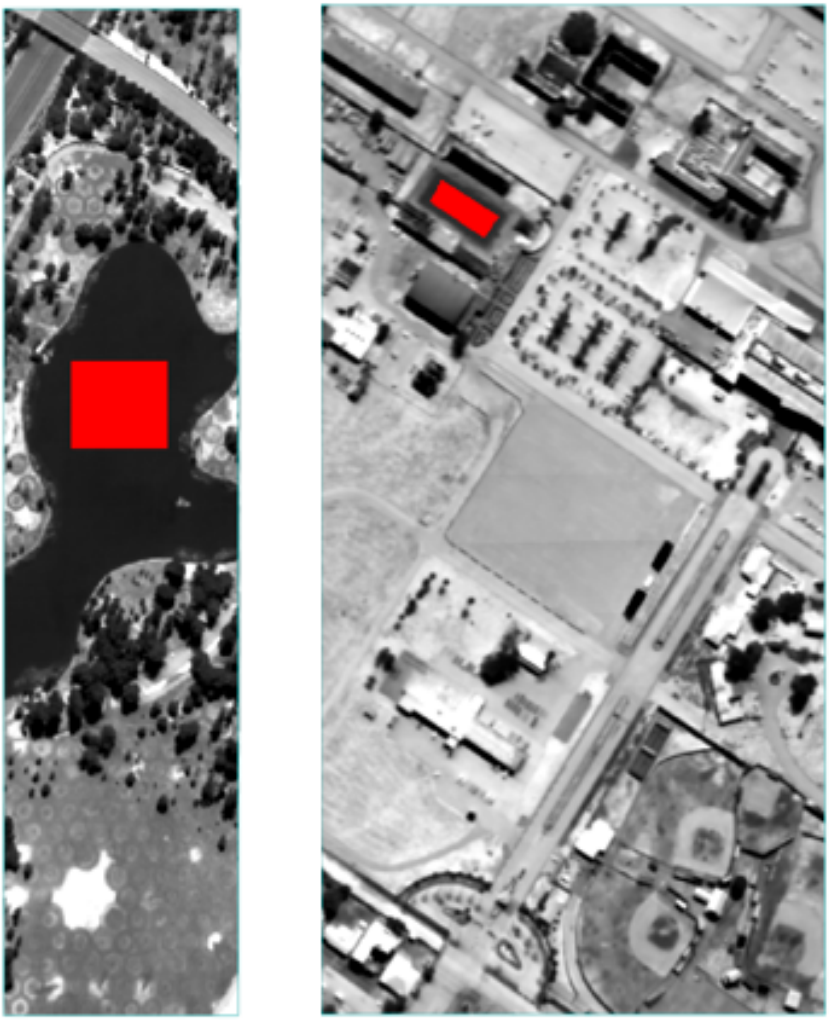

FIGURE 6.6: MURI band 6 stitched images from the testflight on October 4^{th}, 2019. Left: El Dorado East Regional Park with ROI chosen overlapping area where reference measurements were recorded. Right: JFTB pool with ROI chosen over inside of pool, away from the edges.

$$L_{sr} = \epsilon(\lambda)B(\lambda, T)\tau(\lambda) + L_u(\lambda) + [1 - \epsilon(\lambda)]L_d(\lambda)\tau(\lambda) \tag{6.1}$$

where L_{sr} is the band effective sensor reaching radiance, ϵ is the emissivity of the surface, τ is the transmission of the atmosphere, $B(\lambda, T)$ is the radiance contributed from a blackbody at a specific wavelength and temperature as described by Planck's blackbody curve, $L_u(\lambda)$ is the upwelling radiance, and L_d is the downwelling radiance.

The MURI images, provided by DRS in digital counts, are first converted to brightness temperature using calibration curves provided by DRS. Brightness temperatures are then converted to band effective radiance using a look up table which was derived using the MURI response functions. The surface emissivity for water was retrieved from the MODIS UCSB Emissivity Library [60][93].

Values for trasmissivity, upwelling radiance, and downwelling radiance were all determined using atmospheric modeling using MODTRAN4. The radiative transfer models of MODTRAN4 were informed by reanalysis data from the Goddard Earth Observing System forward processing (GEOS-FP) dataset in order to better represent the conditions under which the images were recorded [22][64]. As the GEOS-FP data is not finely sampled enough to overlap our targets both spatially and temporally, the four closest GEOS-FP data points were used to interpolate to our flights location and time using inverse distance weighting [9]. MODTRAN 4 provides atmospheric transmission, upwelling radiance, and the radiance contribution for downwelling radiance, as described in Chapter 4 Section 4.3. This means the only value left unknown is the surface temperature. By solving for $B(\lambda, T)$, a MURI specific radiance to black body temperature conversion table can be used to determine surface temperature.

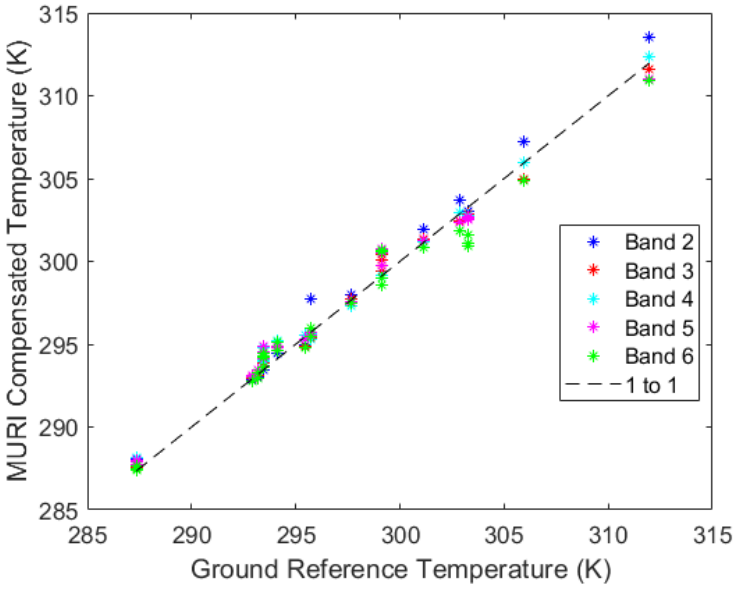

FIGURE 6.7: Single band surface temperature retrievals from MURI 2019 testflights.

6.4 MURI In-flight Surface Temperature Retrieval Performance

6.4.1 Surface Temperature and Radiometric Accuracy

Validation efforts have been focused on the collection of water bodies from the September and October testflights performed in 2019. DRS provided brightness temperature values derived from MURI imagery for the following water bodies: JFTB pool, El Dorado large and small ponds, Residence Inn pool and spa, Landsat Buoy 46025, and Landsat Buoy 46086. These values were then used to predict LST using the method described above. Results were compared to reference measurements made during the 2019 test flights. The results of the single band temperature retrieval are shown in Fig. 6.7 and Table 6.3.

For all bands, this approach leads to mean temperature errors of less than half a Kelvin and RMSE of less than a Kelvin. This demonstrates the viability of MURI data and shows the system is capable of surface temperature retrieval. This also serves to validate the atmospheric compensation approach that is required for successful application of the TES method.

The same assessment described above in terms of temperature is shown in terms of radiance in Fig. 6.8 and Table 6.4. The TIRS requirement for radiometric uncertainty during calibration is defined between 260 and 330 K as less than 2% [66].

TABLE 6.3: Single Band Temperature Retrieval Error for MURI's Fall 2019 Test Flight.

MURI Band	RMSE (K)	RMSE (%)	Mean Error (K)	Mean Error (%)
2	0.80	0.27	0.41	0.14
3	0.65	0.22	0.22	0.08
4	0.71	0.24	0.37	0.13
5	0.81	0.27	0.34	0.12
6	0.93	0.32	-0.10	0.03

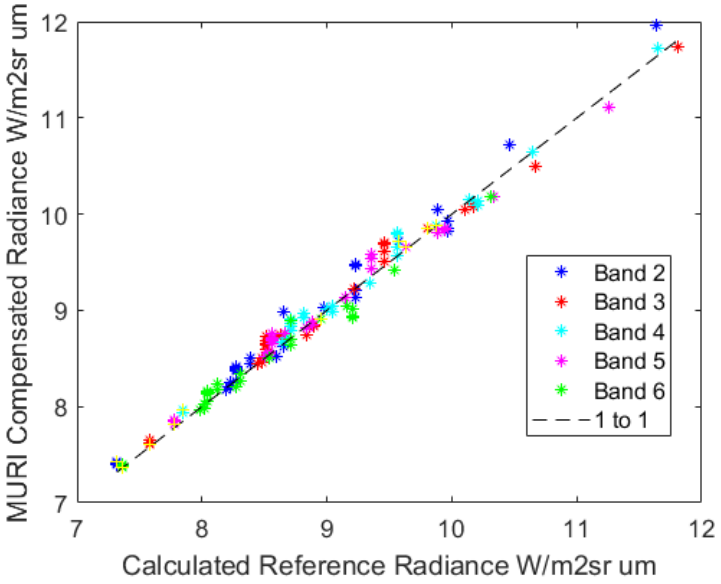

FIGURE 6.8: Surface radiance emission calculations from MURI 2019 testflights.

DRS independently demonstrated that MURI is meeting this requirement[27][32]. However, taking the root mean squared error as an estimate for the uncertainty, it is evident that this data is meeting this requirement even after applying compensation using ancillary data.

TABLE 6.4: Surface radiance emission calculations from MURI 2019 testflights.

MURI Band	RMSE ($\frac{W}{m^2 sr \mu m}$)	RMSE (%)
2	0.14	1.6
3	0.11	1.2
4	0.11	1.2
5	0.11	1.3
6	0.11	1.3

6.5 Application of Split Window Algorithm on MURI Testflight Data

6.5.1 Description of Split Window Study

The 2019 testflight campaign was designed to overlap with Landsat8 TIRS overpass. As seen in Table 6.1, five days and five targets had unobstructed coincidental flights. However, the data from 9/3 lacks a reference measurement, as the Salton Sea buoy was not reporting that day. The Salton Sea buoy was reporting on 10/7, meaning in total, there are four days of overlap over five separate targets.

Coefficients for the Split Window algorithm were derived for both MURI and TIRS using the method described in Chapter 4 [1]. While MURI testflights were performed at 11000 ft, the coefficients were calculated for 12700 ft. Recall the Split Window equation is:

$$LST = b_0 + (b_1 + b_2\frac{1-\epsilon}{\epsilon} + b_3\frac{\Delta\epsilon}{\epsilon^2})\frac{T_i + T_j}{2} + (b_4 + b_5\frac{1-\epsilon}{\epsilon} + b_6\frac{\Delta\epsilon}{\epsilon^2})\frac{T_i - T_j}{2} + b_7(T_i - T_j)^2 \quad (6.2)$$

where T_i is the brightness temperature calculated for the first of the two channels (TIRS band 1, MURI band 5), and T_j is the brightness temperature calculated for the second of the two channels (TIRS band 11, MURI band 6). ϵ is the average emissivity between the two bands ($\frac{\epsilon_i+\epsilon_j}{2}$) and $\Delta\epsilon$ is the difference between the emissivity of the bands ($\Delta\epsilon = \epsilon_i - \epsilon_j$). The system specific coefficients are defined as b_0 through b_7.

Images consisting of surface temperature retrievals using the Split Window approach were provided by Dr. Tania Kleynhans of the Rochester Institute of Technology. From these images, ROIs were identified around the areas where reference surface temperatures were recorded, which can be seen in Figure 6.9. An average number of pixels in each ROI is listed in Table 6.5. As the TIRS images are georeferenced, the ROIs are defined the same for Landsat TIRS bands 10 and 11.

MURI split window coefficients are listed in Table 6.6. The dataset used for this analysis is described in Table 6.1. The results are broken down into two parts. The

[1] Coefficients provided by Dr. Tania Kleynhans of Rochester Institute of Technology

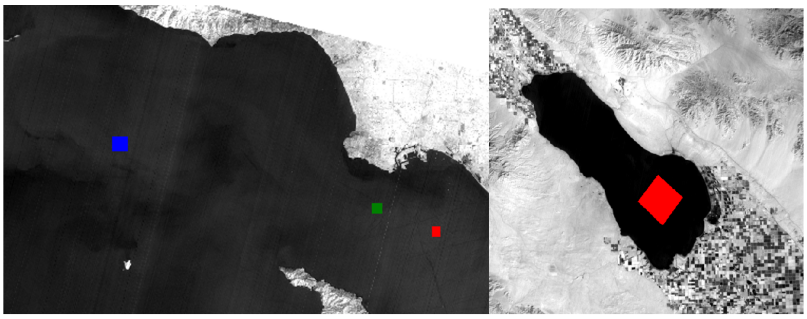

FIGURE 6.9: Sample of Split Window retrieved surface temperatures images from 2019 data set. Left: Ocean buoy targets off the coast of Long Beach California, blue: buoy 46025, green: buoy 46222, red: buoy 46253. Right: Salton Sea.

TABLE 6.5: ROI pixel counts for Landsat 8 TIRS SW temperature retrievals from 2019 coincidental flights with MURI.

Target ROI Set	Pixel Count
Ocean Buoys	6568
Lake Tahoe	6552
Salton Sea	64899

first part describes the results in terms of just the targets recorded during the coincidental flights with TIRS. For targets where there were multiple MURI flightlines over the target, the average of the retrieved temperature was calculated and reported. The second way the data is presented shows MURI performance across the entire list of targets from Table 6.1.

TABLE 6.6: Split window coefficients for MURI calculated

Coefficient	Value
b_0	3.42
b_1	0.99
b_2	0.15
b_3	-0.37
b_4	4.61
b_5	0.62
b_6	-1.95
b_7	0.15

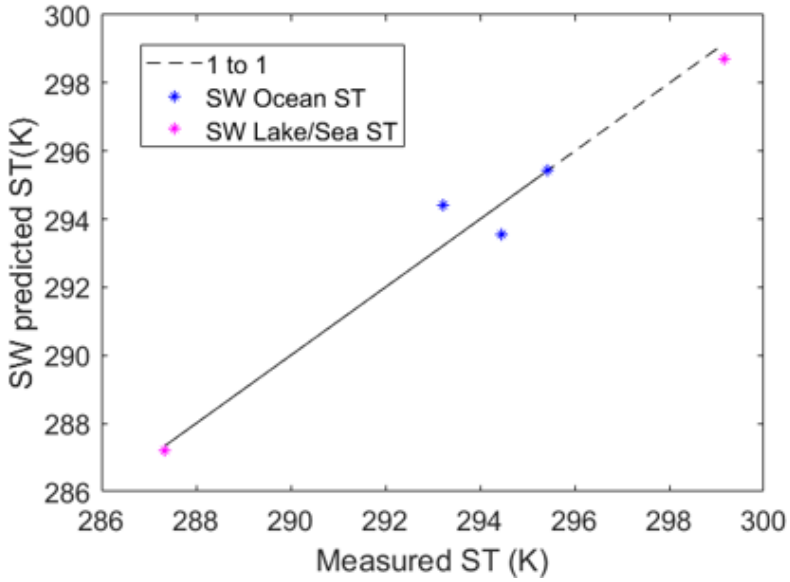

FIGURE 6.10: TIRS split window temperature retrieval from the 2019 coincidental overpass with MURI. TIRS retrieval shows a RMSE of 0.66 K.

6.5.2 Split Window Application Results

Figures 6.10 and 6.11 show the results of applying the Split Window algorithm to MURI testflight data. The TIRS split window temperature retrieval shows a RMSE of 0.66 K with an average absolute temperature difference of 0.12 K. MURI split window temperature retrieval shows a RMSE of 1.22 K with an average absolute temperature difference of 0.81 K. With this approach, MURI is being outperformed by TIRS, showing a RMSE of nearly double that of TIRS. For the cases of the Lake/Sea, MURI appears to be predicting significantly higher temperatures than the reference measurements, something that does not appear in the ocean buoy retrievals.

Figure 6.12 demonstrates the results of applying the split window algorithm to all targets shown in Table 6.1. Again, it is noted that the Salton Sea retrieved temperature is considerably higher than the reference measurement. The calculated RMSE for this set is 1.4 K and the mean absolute temperature difference is 0.79 K, similar to the subset above. Some of this error may be do to in flight calibration of the instrument. Additional error may be due to the reference measurements, as both the buoy and tidbit data loggers are accurate only within 0.5 K and 0.2 K respectively [68][6].

While MURI may not have met the standards of TIRS when applying the Split Window algorithm during this testflight period, this examination does show that

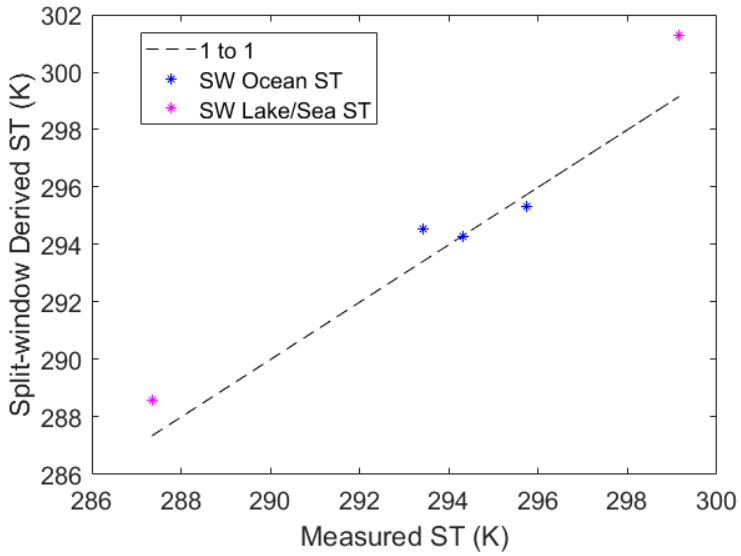

FIGURE 6.11: MURI split window temperature retrieval from the 2019 coincidental testflight with TIRS. MURI retrieval shows a RMSE of 1.22 K.

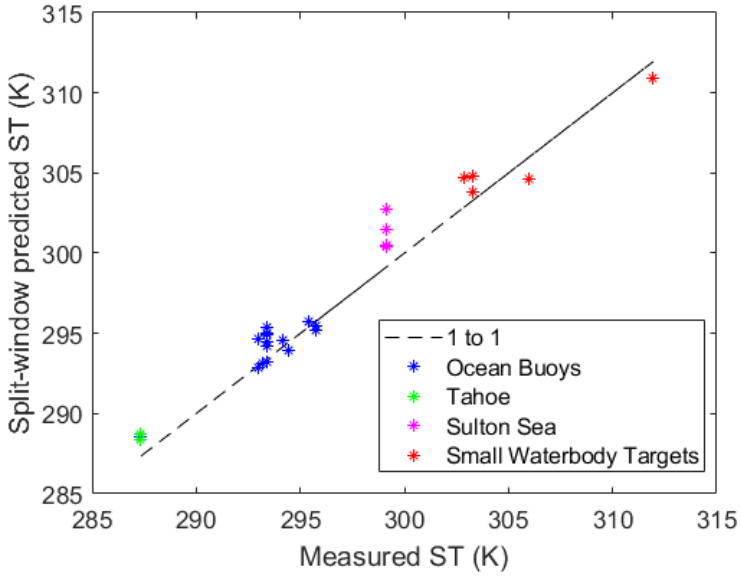

FIGURE 6.12: MURI split window temperature retrieval from the 2019 testflights including small waterbody targets. Results show a RMSE of 1.4 K.

Split Window is a viable approach for retrieving surface temperature from MURI data. Further refinement in the inflight calibration of the instrument, surface reference measurements, and post processing techniques will contribute to improvements in the accuracy of the temperature retrieval.

6.6 Application of Temperature Emissivity Separation to MURI Testflight Data

6.6.1 Description of Temperature Emissivity Separation Study

As described in Chapter 4, the Temperature Emissivity Separation algorithm requires an appropriate atmospheric compensation approach and the calculation of system specific coefficients. As shown in section 6.4.1, the chosen atmospheric approach is appropriate for temperature retrieval applications. Calculating the system specific coefficients requires selecting a group of surface emissivities to regress the coefficients that take MMD, defined in Eqn. 4.8, to minimum emissivity. The equation is defined as:

$$\epsilon_{min} = A_0 + A_1 MMD^{A_2} \tag{6.3}$$

where A_0, A_1, and A_2 are the coefficients of interest.

Four different collections of emissivities were chosen to calculate the MMD coeffients. Each of these emissivities were calculated from the ECOSTRESS spectral libraries (formerly the ASTER database) reflectance measurements utilizing Kirchoff's law. A summary of the four sample sets can be found in Table 6.7. The first set of emissivities is a collection of 53 samples from the ECOSTRESS spectral library [5][62]. This subset, which is referred to as Method 1, is the same subset used to train the TES algorithm used by ECOSTRESS and is most representative of naturally occurring geologic end-members you would observe at remote sensing scales of about 100 m. In addition to each of the samples, each sample is adjusted by a vegetation fraction of 25%, 50%, and 75% using the conifer samples in the collection. This way, the coefficients are trained on a dataset that includes representations of

mixed pixels. The result is number of samples totally 209 emissivities from which the coefficients from Eqn 6.3 are derived.

Method 2, or the second set of emissivities used to derive the TES coefficients, takes the 53 samples from Method 1 (the ECOSTRESS subset) and adds in the remaining water types from the ECOSTRESS spectral library. Method 1 includes ice and distilled water; this new set includes the water types: frost, seawater, and seafoam. Again, each sample is adjusted by a vegetation fraction of 25%, 50%, and 75% using the conifer samples. The result is a sample set of 221 samples.

Method 3 for calculating the coefficients utilizes the majority of the ECOSTRESS database. As is convention for deriving TES coefficients, samples where max emissivity within the MURI bandpasses is less than 90% were not included. TES is not accurate for non-natural gray bodies that have max emissivities of less than 90%, such as metals [36][69]. In total, 1659 samples meet the threshold for MURI. Method 4 utilizes the same samples from Method 3 with the added mixed pixel samples created using the same method as Methods 1 and 2. Method 4 therefore has a total sample size of 6633 emissivities. Table 6.8 shows the coefficients regressed using each method.

TABLE 6.7: Description of the four different emissivity sample sets used to calculate MURI TES coefficients

Method #	Description	Number of Samples
#1	ECOSTRESS subset	209
#2	ECOSTRESS +additional water samples	221
#3	Full ECOSTRESS database	1659
#4	Full ECOSTRESS database + vegetation fraction	6633

TABLE 6.8: Four different TES coefficients calculated using the methods described in 6.7 for MURI

Method #	A_0	A_1	A_2
#1	1.0096	0.7819	0.8008
#2	1.0117	0.7794	0.7921
#3	0.9902	0.7015	0.7497
#4	0.9976	0.7291	0.7807

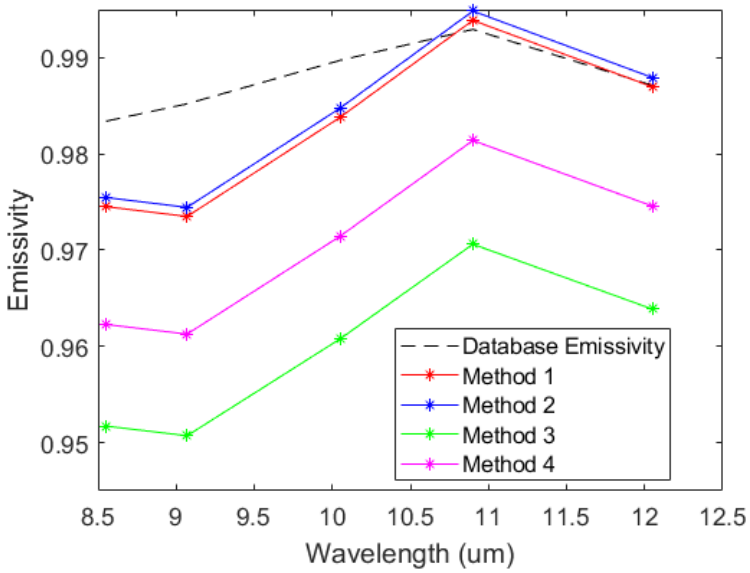

FIGURE 6.13: Mean water surface emissivity retrievals by MURI using four different sets of TES coefficients.

6.6.2 TES Application Results

The MURI image data used for this assessment is waterbody data from the October testflight performed in 2019, specifically the data shown in Table 6.1 from 10/3, 10/4, 10/5, and 10/7. In addition, the stitched imagery of El Dorado East Regional Park and JFTB pool from 10/4, described in Section 6.2.2, was used to evaluate MURI's performance with this method.

Figure 6.13 shows the TES retrieved emissivities for each of the four sets of coefficients listed above while Figure 6.14 shows the TES temperature retrievals. Table 6.9 details the RMSE in the retrieved temperatures and emissivities. Overall results indicate the application of the TES method on MURI data is capable of temperature retrievals within a Kelvin. The results also show that emissivity retrieval of about 0.01 emisivity units is possible with the TES approach.

From these results, it is noted that Method 1 slightly outperforms Methods 2 and 4, while greatly outperforming Method 3, in retrieving surface temperature. Method 1 and 2 show similar performance in emissivity retrievals, outperforming Method 3 and 4.

The results here indicate that the Temperature Emissivity Separation algorithm is a viable approach for this novel system. Water surface temperature retrievals are

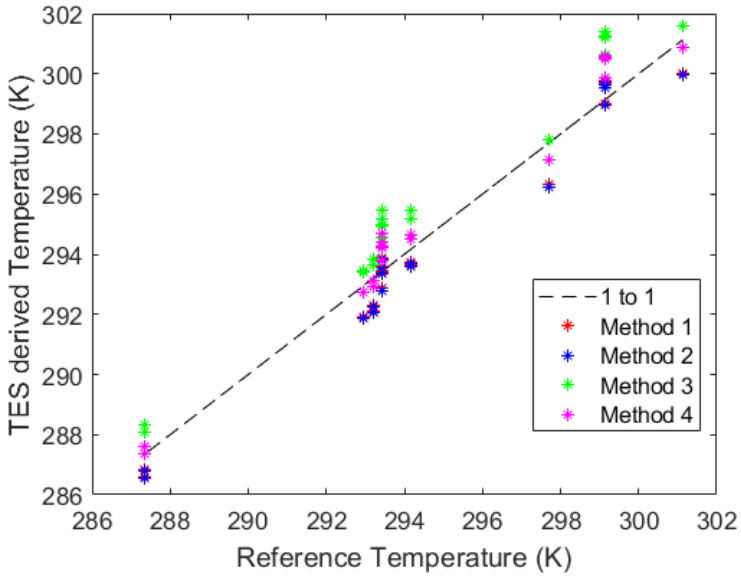

FIGURE 6.14: Water surface emissivity retrievals by MURI using four different sets of TES coefficients.

TABLE 6.9: RMSE for emissivity and temperatures retrieved using TES method on MURI 2019 testflight data.

Method #	Temp. RMSE	ϵ_2	ϵ_3	ϵ_4	ϵ_5	ϵ_6
#1	0.70	0.014	0.012	0.009	0.002	0.007
#2	0.74	0.013	0.012	0.008	0.003	0.007
#3	1.35	0.033	0.038	0.029	0.022	0.024
#4	0.76	0.024	0.024	0.019	0.012	0.014

shown to be within 1 K of reference temperatures are possible, and emissivity retrievals are shown to be within 2% of database values. The results here indicate using the ECOSTRESS subset of natural materials outperforms the other approaches. An explanation of why this is a reasonable result is exemplified in Table 6.10 and Figure 6.15. For Methods 1 and 2, all samples fall within $\pm$ 0.039 of the regression line. The regression line being derived using fewer samples means the approach will be better suited to retrieving temperature and emissivity over similar surface types.

6.7 Spatial Performance Characterization

A preflight experiment was performed to assess MURI's spatial response. A series of images were recorded in lab of a slanted edge target set six degrees from the

TABLE 6.10: Difference between regression line and emissivity samples for each method listed in Table 6.7

Method #	Emissivity Sample to Regression Line Range
#1	$\pm$ 0.039
#2	$\pm$ 0.039
#3	$\pm$ 0.161
#4	$\pm$ 0.217

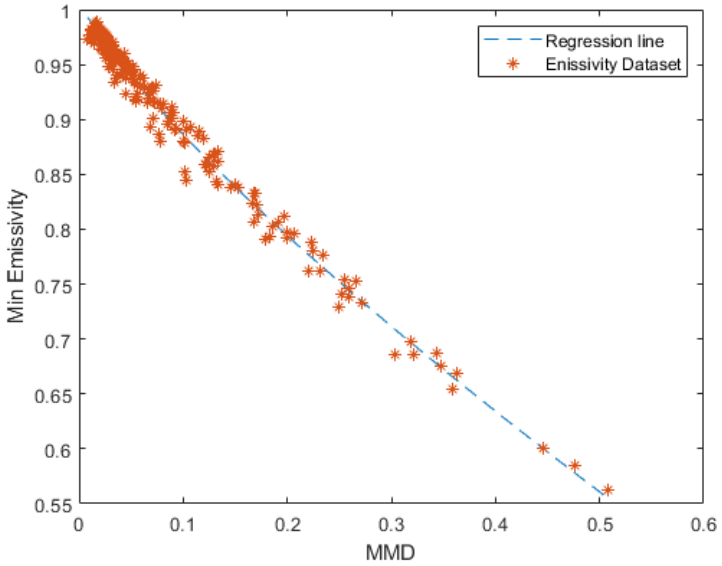

FIGURE 6.15: Relationship between ϵ_{min} and MMD based on the reflectance spectra samples of Method 1 described in Table 6.7. All samples fall within $\pm$ 0.039 of the regression line.

along track direction. Forward motion was simulated using a rotary stage, and single frames were recorded for each band using MURI's back scan method, an example of which can be seen in Figure 6.16.

This imagery allowed for the measurement of MURI's Edge Spread Function (ESF), which represents the system's response to an edge. An ESF was derived from each band using sfrmat4 [18]. This is accomplished by taking a subset of the image containing only the edge, identifying the edge in each line of pixels, then projecting each pixel onto a line perpendicular to the edge[54][100]. A visualization of this approach can be seen in Figure 6.17. This approach allows for subpixel sampling of the ESF. The ESF is then normalized to values between 0 and 1.

From the normalized ESF, the edge slope and edge extent were independently

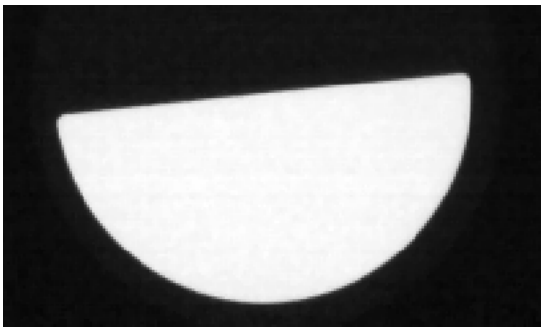

FIGURE 6.16: Single frame MURI band 5 lab recorded image of edge target.

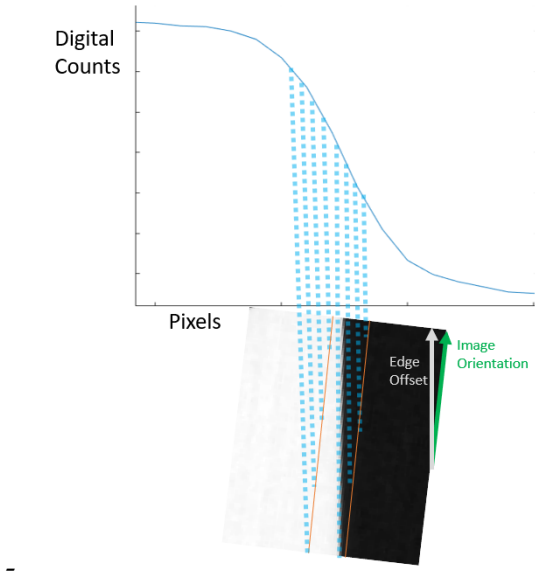

FIGURE 6.17: Edge Spread Function sampling and projection method. This approach provides a super-sampled ESF.

determined by interpolating the ESF. The edge slope requirement for TIRS is defined as the rate of change between 0.4 and 0.6 amplitude of the ESF. The edge extent requirement for TIRS is defined as the ground distance between the 0.1 and 0.9 amplitude of the ESF [100].

The edge slope and edge extent for MURI bands 5 and 6 can be directly compared to TIRS measured values for edge slope and edge extent. TIRS spatial requirements included an edge slope of > 0.7 pixels^{-1} (0.007 m^{-1}) and an edge extent of < 150 m [57]. In prelaunch measurements, TIRS demonstrated an along track edge slope of 0.53 pixels^{-1} and an edge extent of 234 m for the 10.9 μm band, and an edge slope of 0.63 pixels^{-1} and edge extent of 184.3 m for the the 12 μm band [100]. As TIRS has an approximate spatial resolution of 100 m, an edge extent of 234 m and 184.3 m

TABLE 6.11: Lab Knife-edge Image Edge Spread Function Analysis

MURI Band	Edge Slope (pixels^{-})	Edge Extent (pixels)
2	0.42	2.5
3	0.73	1.63
4	0.57	2.16
5	0.71	1.66
6	0.58	1.97

correspond to approximately 2.34 and 1.84 pixels respectively.

In order to compare the MURI spatial performance to TIRS performance, the per meter edge extent must be converted to a per pixel measurement. MURI's test flights were performed at 3.35 km (11,000 ft). At this altitude, MURI has a ground sample distance of 0.48 m. When projected to TIRS altitude of 705 km, MURI would have a ground sample distance of approximately 100 m, which is equivalent to the TIRS spatial resolution.

Edge slope and edge extent values for the lab knife-edge images are provided in Table 6.11. The results show that in a lab setting, MURI bands 3 and 5 are exceeding the prelaunch measurements of TIRS with an edge slope of 0.73 pixels^{-1} and 0.71 pixels^{-1}, respectively (compared to TIRS band 10: 0.53 pixels^{-1} and TIRS band 11 0.63 pixels^{-1}). MURI bands 3 and 5 are also exceeding TIRS prelaunch measurements of edge extent (1.63 pixels for band 3 and 1.66 pixels for band 5 compared to 2.34 pixels for TIRS band 10 and 1.84 pixels for TIRS band 11). It should be noted that band 3 and 5 are meeting the Landsat requirements for edge slope, but failing to meet Landsat requirements for edge extent by about 10%.

Referring again to Table 6.11, MURI bands 2, 4, and 6 under-perform when compared to MURI bands 3 and 5, TIRS bands 10 and 11, and to the TIRS requirements. Considering MURI bands 2, 4, and 6 reside on a different array than MURI bands 3 and 5, as described in Chapter 2 and shown in Figure 6.3, the source of this under-performance is likely focus-related and not related to the system design.

To assess MURI's in-flight spatial performance, a target was selected from the 2019 testflight dataset from a MURI collect over Russell Ranch, California. Figure 6.18 shows the field chosen for this experiment. From the test-flight dataset, a single MURI 14-frame stacked band 5 image acquired over the target was used to evaluate MURI's spatial response. Note that the lab target was recorded in the along track

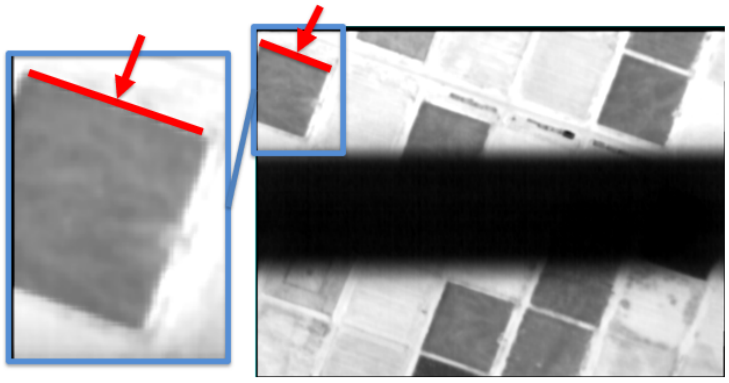

FIGURE 6.18: Right: 14 frames stacked MURI image recorded by Tam 1 in October of 2019 Russell Ranch California. Left: Selected edge target for assessment of band 5 ESF.

direction while the target from the 2019 Russell Ranch dataset was recorded in the cross track direction.

While the Russell Ranch target does contain defined edges, the target is not ideal as the bright side of the edge shows a decrease in brightness away from edge. To assess MURI's ESF using this target, a Fermi function with an added linear term was fit to the data. The adjusted Fermi function fit is defined as:

$$f(x) = b_1 + \frac{b_2 - b_1}{1 + e^{-b_3(x-b_4}} + b_5 x \tag{6.4}$$

where, b_1 can be equated to the mean value on the dark side of the ESF and b_2 can be equated to the mean value on the bright side of the edge. The additional linear term, $b_5 x$, is included due to the brightness on the bright side of the edge being inconsistent [100]. Figure 6.19 shows the results of fitting the modified Fermi function to the ESF produced using sfrmat4.

The ESF was normalized using the following equation:

$$f(x)_{normalized} = \frac{f(x) - b_1 - b_5 x}{b_2 - b_1} \tag{6.5}$$

The mean value of the dark side (b_1) and the linear term ($b_5 x$) are subtracted from the Fermi fit ESF. The result is then divided by mean value of the bright side of the edge (b_2) with b_1 subtracted out. The normalized Fermi Fit ESF for the Russell Ranch data with edge slope and edge extent identified can be seen in Figure 6.20.

Table 6.12 shows the comparison between the airborne and lab measured ESF

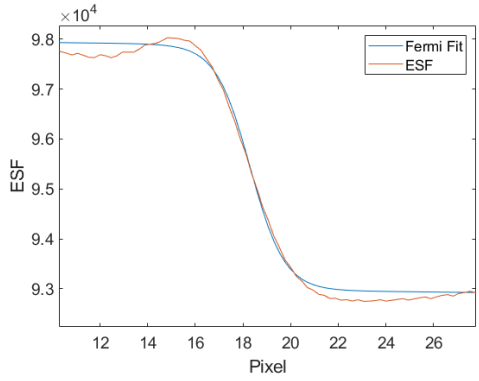

FIGURE 6.19: ESF and corresponding Fermi function fit for MURI band 5 image subset over Russell Ranch, California.

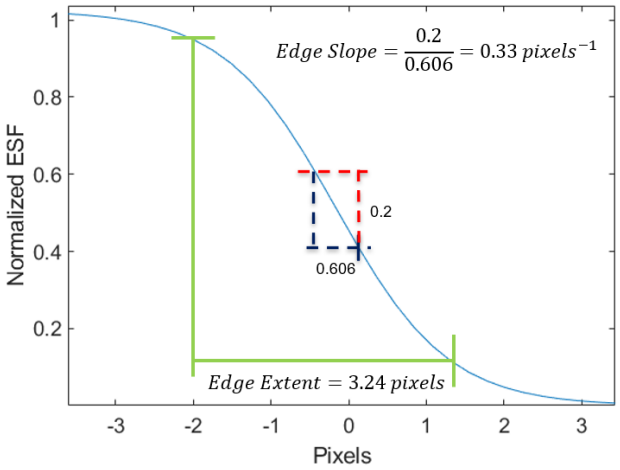

FIGURE 6.20: Normalized Fermi fit ESF with edge slope and edge extent for MURI band 5 over Russell Ranch 2019 target.

for MURI band 5 using the modified Fermi function fit method. The results show that in a lab setting, MURI is exceeding the prelaunch measurements of TIRS with an edge slope of 0.71 pixels^{-1} and an edge extent of 1.55 pixels. The system sees a drop in spatial response when airborne, resulting in an edge slope of less than half of what was recorded in the lab (0.33 pixels^{-1}) and an edge extent of nearly double the lab measured value (3.24 pixels). Although the loss is present, some of this loss of spatial response can be attributed to the movement of the aircraft, which would not affect a satellite system.

An additional spatial response examination was performed on data collected during testflights performed in 2020. This examination focused on two MURI images. The first is a single frame, unstacked image. The second is a 14 frames stacked image, stitched with an approach that utilized SIFT features to identify common

TABLE 6.12: MURI band 5 ESF analysis using modified Fermi function

Image Data Description	Edge Slope (pixels^{-1})	Edge Extent (pixels)
Lab: Single Frame	0.71	1.55
Airborne: 14 Frames Stacked	0.33	3.24

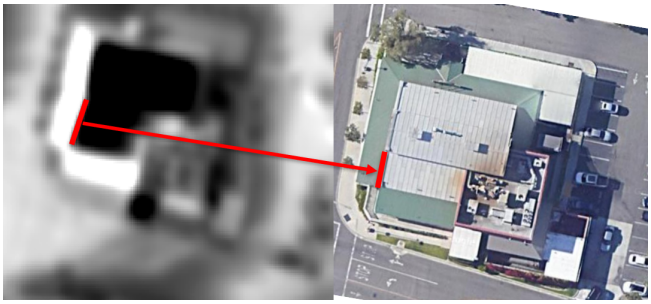

FIGURE 6.21: Left: MURI band 5 image subset of restaurant roof chosen as edge target for analysis of spatial response. Image was recorded during the Fall 2020 collect in Cypress, California. The two types of material on the restaurant roof provides a high contrast target. Right: Google maps image of the target.

features between the sets of 14 frames stacked image. The chosen target for both images, which can be seen in Fig. 6.21, is the roof edge of a restaurant in Long Beach Center, just North of the El Dorado East Regional Park.

For this examination, the band 5 ESF was examined directly and did not require use of the Fermi function approach. The results of the ESF assessment can be seen in Table 6.13. As was seen with the Russell Ranch dataset, there is a large drop in spatial response between the lab data and the airborne data. While there is a drop between the airborne single frame and the 14 frames stacked, this drop is smaller than the drop between lab and airborne. It should be noted that DRS did not finely focus the optics for the 2020 testflight, compared to the 2019 dataset, as demonstration of spatial performance was not the objective of the mission. Regardless, this serves to demonstrate the expected drop between the airborne single frame data, and the 14 frames stacked and stitched images from MURI's airborne instrument.

TABLE 6.13: MURI band 5 ESF analysis using data from 2020 dataset.

Image Data Description	Edge Slope (pixels^{-}1)	Edge Extent (pixels)
Lab: Single Frame	0.71	1.66
Airborne: Single Frame	0.28	3.72
Airborne: 14 Frames Stacked	0.22	4.47

6.8 Conclusions

The studies depicted here demonstrate the inflight capabilities of the MURI system. The initial radiometric accuracy and surface temperature estimations served to validate the MURI system, testflight operation, and the atmospheric compensation approach. The application of the Split Window technique exhibits the ability for a thermal infrared uncooled microbolometer focal plane array based system to retrieve surface temperature without the use of atmospheric compensation. While the approach did not meet the performance of Landsat 8 TIRS, MURI did show temperature retrievals close to within 1 K.

The results of applying the Temperature Emissivity Separation method on MURI data show that temperature retrievals of within 1 K of the target temperature and surface emissivity retrievals of within 0.01 are possible with this approach. Further, the examinations demonstrated the importance of choosing the spectra that are used to regress the minimum emissivity/MMD equation. For both the SW and TES approaches, additional surface types could be examined to further demonstrate the system's temperature and emissivity retrieval capabilities.

The spatial response demonstration shows how MURI behaves in both ideal and non-ideal scenarios. The data recorded in lab shows the ability of the MURI system to meet TIRS standards. Additionally, it is demonstrated that the inflight loss in spatial response due to stacking frames using MURI's backscanning method is considerably less than the loss due to aircraft movement. This indicates that a potential satellite system, which is a more stable platform, would not experience the same level of loss. For a more accurate representation of the system's capabilities, large, uniform, thermal edge targets should be used.

Chapter 7

Conclusions

Throughout this thesis, the focus has been on identifying and assessing the performance of environmental applications for a novel uncooled multispectral imaging system. The work developed into investigating two specific environmental applications: detection of enhanced atmospheric methane and surface temperature retrieval. In investigating the detection of enhanced levels of atmospheric CH_4, a novel approach to detecting methane with two thermal infrared bands was defined, the Normalized Differential Methane Index. When compared to the Matched Filter Approach, NDMI demonstrated similar levels of accuracy in some scenarios to the Matched Filter while using two bands compared to the Matched Filter's six. Drawbacks of the NDMI approach were identified, specifically the approach's sensitivity to drastic changes in surface temperature and surface emissivity. This work served to demonstrate that a thermal infrared multispectral uncooled system is capable of detecting elevated CH_4 with only a single spectral band allocated to CH_4 absorption features. Further, scenarios where detection is possible were predicted using simulated data produced using a combination of real hyperspectral data and MODTRAN. The initial studies revealed the system is capable of detecting a 20 m thick CH_4 plume of 10-20 ppm above background levels when column water vapor is low using both the NDMI and matched filter approaches. Further investigation showed how column water vapor and system noise can mask CH_4 plume signal, such that a 30 ppm plume may be undetectable when system noise and column water vapor is high. Finally, a new system was proposed to improve CH_4 detection using the matched filter. The MURI+ system, with two additional bands and a modified MURI band 1 was able to identify pixels with enhanced levels of atmospheric methane in

over twice as many cases as MURI.

Efforts to characterize the temperature retrieval capabilities of the novel system lead to the identification and evaluation of two temperature retrieval approaches: the two band Split Window and the five band Temperature Emissivity Separation algorithms. In applying the approaches to simulated data, we were able to predict the performance of the system before the completion of the testflight instrument. Additionally, an appropriate atmospheric compensation approach was identified for the system. The application of the SW algorithm allowed us the ability to directly compare the system to Landsat8 TIRS. Although the system was outperformed by TIRS during the first round of testflights (RMSE of 0.66 K for TIRS compared to 1.22 K for MURI), the investigation did indicate that SW was a viable approach for retrieving surface temperature. Application of the TES algorithm provided evidence that the system was capable of retrieving surface emissivity within 2% of database values while retrieving temperatures within 1 K of surface reference measurements. An evaluation into the calculation of TES coefficients revealed a subset of naturally occurring surface emissivities outperform coefficients calculated using a wider array of emissivity measurements.

Overall efforts to validate the MURI system's inflight performance were generally successful. Spatially, the system outperforms TIRS performance in lab, showing an edge slope of 0.71 pixels^{-} to TIRS band 10's 0.53 pixels^{-} and IRS band 11 0.63 pixels^{-} and an edge extent of 1.66 pixels for MURI band 5 compared to 2.34 pixels for TIRS band 10 and 1.84 pixels for TIRS band 11. However, inflight performance demonstrated significant loss possibly due to the movement of the aircraft. The slight shift in the as-built band 1 filter did leave the band sensitive to atmospheric water vapor and likely contributed to the band's inflight performance being dominated by the atmosphere. Additionally, band 1 may experience lower sensitivity due to its relatively narrow bandpass. The other bands, however, were able to be tested against reference measurements and demonstrated agreement with reference temperatures after atmospheric compensation.

The work detailed in this thesis served to demonstrate the that MURI system is viable for temperature and emissivity retrieval and has potential for detection of enhanced levels of atmospheric methane.

Chapter 8

Future Directions

There are three avenues for future work branching from the efforts presented in this thesis. First, while this thesis focused primarily on environmental applications based around bands 1, 5, and 6, bands 2, 3, and 4 have potential for environmental applications that have yet to be investigated, as to do so was outside the scope of this thesis. Bands 2 and 3 are designated to overlap with known SO_2 absorption features, an investigation of the system's ability to detect or characterize SO_2 plumes was beyond the scope of this thesis. However, assessment of detection methods such as the matched filter or an approach similar to NDMI could demonstrate the system's ability to provide useful data in volcanic emission or SO_2 centered applications. Further, the system is designed for surface mineral identification and vegetation monitoring. Application of the TES algorithm is a potential first step for both of these applications, yet there is room to further investigate MURI's ability to provide valuable data for these functions. As the system has demonstrated the ability to retrieve surface temperature and emissivity, examining the system's potential to be useful in evapotranspiration and water stress monitoring applications should be a focus of further investigations.

Second, further analysis of the NDMI method on real data would provide additional validation for the MURI system and the CH_4 detection approach. As the controlled release experiment had to be cancelled due to extraneous circumstances, that experiment could be performed once it is deemed safe to conduct. The apparatus for the experiment has been designed and the experiment outlined, what work remains is to construct the apparatus and conduct the experiment. The controlled release experiment would provide the chance to apply the NDMI approach to real data with

a known quantity of CH_4. Ideally, construction of a system similar to MURI with a band 1 filter closer to the specified filter could help to test the method without the added difficulty of high sensitivity to the water absorption features shown to be present in the constructed band 1 filter.

Third, further testflights of the MURI system provide additional opportunities to test methods and identify new applications. The RIT MURI team has continued to support testflights of the system, and are continuing to investigate temperature and emissivity retrieval as presented in this thesis.

Bibliography

[1] M.C. Anderson, J.M. Norman, W.P. Kustas, R. Houborg, P.J. Starks, and N. Agam. "A thermal-based remote sensing technique for routine mapping of land-surface carbon, water and energy fluxes from field to regional scales". In: *Remote Sensing of Environment* 112.12 (2008), pp. 4227–4241. ISSN: 0034-4257. DOI: https://doi.org/10.1016/j.rse.2008.07.009. URL: https://www.sciencedirect.com/science/article/pii/S0034425708002289.

[2] RK Andrew, D Peter, W Winthrop, and WS John. "Portable Fourier transform infrared spectrometer for field measurements of radiance and emissivety". In: *Appl. Opt* 35 (1996), pp. 1679–1692.

[3] A. John Arnfield. "Two decades of urban climate research: a review of turbulence, exchanges of energy and water, and the urban heat island". In: *International Journal of Climatology* 23.1 (2003), 1–26. DOI: 10.1002/joc.859.

[4] T. Arvidson, J. Barsi, M. Jhabvala, and D. Reuter. "Landsat and Thermal Infrared Imaging". In: *Kuenzer C., Dech S. (eds) Thermal Infrared Remote Sensing. Remote Sensing and Digital Image Processing*. Springer, 2013. DOI: https://doi.org/10.1007/978-94-007-6639-6_9.

[5] A.M. Baldridge, S.J. Hook, C.I. Grove, and G. Rivera. "The ASTER spectral library version 2.0". In: *Remote Sensing of Environment* 113 (2009), pp. 711–715.

[6] Julia A Barsi, John R Schott, Simon J Hook, Nina G Raqueno, Brian L Markham, and Robert G Radocinski. "Landsat-8 thermal infrared sensor (TIRS) vicarious radiometric calibration". In: *Remote Sensing* 6.11 (2014), pp. 11607–11626.

[7] W.G.M. Bastiaanssen, M. Menenti, R.a. Feddes, and A.A.M. Holtslag. "A remote sensing surface energy balance algorithm for land (SEBAL). 1. Formulation". In: *Journal of Hydrology* 212-213 (1998), 198–212. DOI: 10.1016/s0022-1694(98)00253-4.

[8] F. Becker and Z.L. Li. "Towards a local split window method over land surfaces". In: *Int. J. Remote Sens.* 11.3 (1990), pp. 369–393.

[9] A. Bekele, R. Downer, M. Wolcott, W. Hudnall, and S. Moore. "Comparative Evaluation of Spatial Prediction Methods in a Field Experiment for Mapping Soil Potassium". In: *Soil Science* 168.1 (2003), pp. 15–28.

[10] A. Berk, P. Conforti, R. Kennett, T. Perkins, F. Hawes, and J. van den Bosch. "MODTRAN® 6: A major upgrade of the MODTRAN® radiative transfer code". In: *2014 6th Workshop on Hyperspectral Image and Signal Processing: Evolution in Remote Sensing (WHISPERS)*. 2014, pp. 1–4. DOI: 10.1109/WHISPERS.2014.8077573.

[11] Alexander Berk, Gail P. Anderson, Lawrence S. Bernstein, Prabhat K. Acharya, H. Dothe, Michael W. Matthew, Steven M. Adler-Golden, Jr. James H. Chetwynd, Steven C. Richtsmeier, Brian Pukall, and et al. "MODTRAN4 radiative transfer modeling for atmospheric correction". In: *Optical Spectroscopic Techniques and Instrumentation for Atmospheric and Space Research III* (1999). DOI: 10.1117/12.366388.

[12] Alexander Berk, Larry Bernstein, and David Robertson. "MODTRAN: A moderate resolution model for LOWTRAN: Technical Report A185 384". In: (July 1987), pp. 1–35.

[13] Alexander Berk, Patrick Conforti, Fred Hawes, Tim Perkins, Chona Guiang, Prabhat Acharya, Rosemary Kennett, Brian Gregor, and Jeannette van den Bosch. "Next Generation Modtran for Improved Atmospheric Correction of Spectral Imagery". In: *Airforce Research Laboratory* AFRL-RV-PS-TR-2016-0105 (2016).

[14] R. Bhan, R. Saxena, C. Jalwani, and S. Lomash. "Uncooled Infrared Microbolometer Arrays and their Characterisation Techniques". In: *Defence Science Journal* 59.6 (2009), 580–589. DOI: 10.14429/dsj.59.1562.

[15] D. Bjerketvedt, J. Roar Bakke, and K. van Wingerden. "Gas Explosion Handbook". In: *Journal of Hazardous Materials* 52.1-150 (1997).

[16] Paul E Bortfeldt. "Thermal control design for the MODIS instrument". In: *SAE Transactions* (1994), pp. 1679–1688.

[17] Joshua B. Broadwater, Thomas S. Spisz, and Alison K. Carr. "Detection of gas plumes in cluttered environments using long-wave infrared hyperspectral sensors". In: *Proc. of SPIE 6954, 69540R-169540R-169512 Chemical, Biological, Radiological, Nuclear, and Explosives (CBRNE) Sensing IX* (Apr. 2008). DOI: 10.1117/12.784707.

[18] Peter D Burns and Don Williams. "Camera Resolution and Distortion: Advanced Edge Fitting". In: *IS&T Internat. Symp. Electronic Imaging, Image Quality and System Performance* (2018).

[19] NOAA:National Data Buoy Center. *data available at: https://www.ndbc.noaa.gov/*.

[20] R.J. Cicerone. "Biogeochemical aspects of atmospheric methane". In: *Global Biogeochemical Cycles* 2 (1988), pp. 229–327.

[21] John C. Crittenden, R. Rhodes Trussel, David W. Hand, Kerry J. Howe, and George Tchobanoglous. "Appendix B: Physical Properties of Selected Gases and Composition of Air". In: *MWH's Water Treatment: Principles and Design*. 2nd ed. John Wiley & Sons inc., 2012, pp. 1857–1858.

[22] GEOS-FP Database. *data available at: https://portal.nccs.nasa.gov/datashare/gmao/geos-fp/das/*. last access: 12 December 2019.

[23] Thermodynamic Initial Guess Retrieval (TIGR) database. *Available online:-https://ara.lmd.polytechnique.fr/index.php?page=tigr*.

[24] Chen Du, Huazhong Ren, Qiming Qin, Jinjie Meng, and Shaohua Zhao. "A Practical Split-Window Algorithm for Estimating Land Surface Temperature from Landsat 8 Data". In: *Remote Sensing* 7.1 (Aug. 2015), 647–665. DOI: 10.3390/rs70100647.

[25] Harry A. C. Eaton. "Infrared imaging bolometers". In: *Observing Photons in Space* (2013), 515–524. DOI: 10.1007/978-1-4614-7804-1_29.

[26] Philip Ely. *Personal Correspondence: DRS Technologies (Email)*. Sept. 2018.

[27] Philip Ely, Aaron Gerace, and Raymond Wagoner. "Multi-Band Uncooled Radiometer Imager (MURI) Airborne Flight Test Status". In: *Earth Science Technology Forum 2020* (June 2020), Virtual.

[28] Philip Ely, Raymond Wagoner, and John Kerekes. "Multiband Uncooled Radiometer Instrument (MURI) for NASA Instrument Incubator Program (IIP)". In: *Earth Science Technology Forum 2018* (June 2018), Silver Spring, Maryland.

[29] Philip Ely, Raymond Wagoner, and John Kerekes. "NASA Instrument Incubator Program (IIP) Multi-Band Uncooled Radiometer Instrument (MURI) Pre-Flight Test Presentation". In: *Earth Science Technology Forum 2019* (June 2019), Moffett Field, CA.

[30] G. Etiope, L. A. Doezema, and C. Pacheco. "Emission of Methane and Heavier Alkanes From the La Brea Tar Pits Seepage Area, Los Angeles". In: *Journal of Geophysical Research: Atmospheres* 122.21 (Nov. 2017). DOI: 10.1002/2017jd027675.

[31] C.C. Funk, J. Theiler, D.A. Roberts, and C.C. Borel. "Clustering to improve matched filter detection of weak gas plumes in hyperspectral thermal imagery". In: *IEEE Transactions on Geoscience and Remote Sensing* 39.7 (2001), 1410–1420. DOI: 10.1109/36.934073.

[32] A. Gerace, R. Eon, T. Kleynhans, N Raqueno, C.M. Webber, P. Ely, and P. Ventresco. "In-Flight Performance of the Multi-band Uncooled Radiometer Instrument (MURI) Thermal Sensor". In: *In review* (2021).

[33] A. Gerace, T. Kleynhans, R. Eon, and M. Montanara. "Towards and Operational, Split Window-Derived Surfacen Temperature Product for the Thermal Infrared Sensors Onboard Landsat 8 and 9". In: *Remote Sensing* 12(2).224 (2020), 1410–1420. DOI: 10.3390/rs12020224.

[34] Alan Gillespie, Shuichi Rokugawa, Tsuneo Matsunaga, J Steven Cothern, Simon Hook, and Anne B Kahle. "A temperature and emissivity separation algorithm for Advanced Spaceborne Thermal Emission and Reflection Radiometer (ASTER) images". In: *IEEE Transactions on Geoscience and Remote Sensing* 36.4 (1998), pp. 1113–1126.

[35] Alan R. Gillespie, Tsuneo Matsunaga, Shuichi Rokugawa, and Simon J. Hook. "Temperature and emissivity separation from Advanced Spaceborne Thermal Emission and Reflection Radiometer (ASTER) images". In: *Infrared Spaceborne Remote Sensing IV* (1996). DOI: 10.1117/12.255172.

[36] Alan R. Gillespie, Shuichi Rokugawa, Tsuneo Hook Simon J.and Matsunaga, and A.B. Kahle. "Temperature/Emissivity Separation Algorithm Theoretical Basis Document, Version 2.4". In: *ATBD Prepared under NASA Contract NAS5-31372* (1999).

[37] A.A. Goodenough and S.D. Brown. "Dirsig5: Next-generation remote sensing data and image simulation framework". In: *IEE Journal of Selected Topics in Applied Earth Obsvervations and Remote Sensing* 10.11 (Nov. 2017), pp. 4818–4833.

[38] Larry L. Gordley, Benjamin T. Marshall, and D. Allen Chu. "Linepak: Algorithms for modeling spectral transmittance and radiance". In: *Journal of Quantitative Spectroscopy and Radiative Transfer* 52.5 (1994), pp. 563–580. ISSN: 0022-4073. DOI: https://doi.org/10.1016/0022-4073(94)90025-6. URL: https://www.sciencedirect.com/science/article/pii/0022407394900256.

[39] I.E. Gordon, L.S. Rothman, C. Hill, R.V. Kochanov, Y. Tan, P.F. Bernath, M. Birk, V. Boudan, A. Campargue, K.V. Chance, B.J. Drouin, J.M. Flaud, R.R. Gamache, J.T. Hodges, D. Jacquemart, V.I. Perevalov, A. Perrin, K.P. Shine, M.-A.H. Smith, P.J. Tennyson, G.C. Toon, H. Tran, V.G. Tyuterev, A. Barbee, A.G. Csaszar, V.M. Devi, T Furtebnacher, J.J. Harrison, J.-M. Hartmann, A Jolly, T.J. Johnson, T. Karman, I. Kleiner, A.A. Kyuberis, J. Loos, O.M. Lyulin, S.T. Massie, S.N. Mikhailenko, N. Moazzen-Ahmadi, H.S.P. Muller, O.V. Naumenko, A.V. Nikitin, O.L. Polyansky, M. Rey, M. Rotger, S.W. Sharpe, K. Sung, E. Straikova, S.A. Tashkin, J. Vander Auwera, G. Wagner, J. Wilzewski, P. Wcisto, S. Yu, and E.J. Zak. "The HITRAN2016 molecular spectroscopic database". In: *Journal of Quantitative Spectroscopy and Radiative Transfer* 203 (2017), pp. 3–69.

[40] Christian Hill, Iouli E. Gordon, Roman V. Kochanov, Lorenzo Barrett, Jonas S. Wilzewski, and Laurence S. Rothman. "HITRANonline: An online interface and the flexible representation of spectroscopic data in the HITRAN database". In: *Journal of Quantitative Spectroscopy and Radiative Transfer* 177 (2016). XVIIIth Symposium on High Resolution Molecular Spectroscopy (HighRus-2015), Tomsk, Russia, pp. 4–14. ISSN: 0022-4073. DOI: https://doi.org/10.1016/j.jqsrt.2015.12.012. URL: https://www.sciencedirect.com/science/article/pii/S0022407315302375.

[41] G.C. Holst. *Common sense approach to thermal imaging*. SPIE Press and JCD Publishing, 2000.

[42] Simon J. Hook, William R. Johnson, and Michael J. Abrams. "NASA's Hyperspectral Thermal Emission Spectrometer (HyTES)". In: *Thermal Infrared Remote Sensing: Sensors, Methods, Applications*. Ed. by Claudia Kuenzer and Stefan Dech. Dordrecht: Springer Netherlands, 2013, pp. 93–115. ISBN: 978-94-007-6639-6. DOI: 10.1007/978-94-007-6639-6_5. URL: https://doi.org/10.1007/978-94-007-6639-6_5.

[43] Simon J Hook and Anne B Kahle. "The micro Fourier transform interferometer (μFTIR)—a new field spectrometer for acquisition of infrared data of natural surfaces". In: *Remote Sensing of Environment* 56.3 (1996), pp. 172–181.

[44] S.J. Hook, G. Chander, J.A. Barsi, R.E. Alley, A Abtahi, F.D. Palluconi, B.L. Markham, R.C. Richards, Schladow S.G., and D.L. Helder. "In-flight validation and recovery of water surface temperature with Landsat-5 thermal infrared data using an automated high-altitude lake validation site at Lake Tahoe." In: *IEEE Trans. Geosci. Remote Sens.* 42 (2004), pp. 2767–2776.

[45] Haili Hu, Jochen Landgraf, Rob Detmers, Tobias Borsdorff, Joost Aan De Brugh, Ilse Aben, André Butz, and Otto Hasekamp. "Toward Global Mapping of Methane With TROPOMI: First Results and Intersatellite Comparison to GOSAT". In: *Geophysical Research Letters* 45.8 (2018), 3682–3689. DOI: 10.1002/2018gl077259.

[46] Glynn Hulley. "ECOSTRESS Level-2 Land Surface Temperature and Emissivity Algorithm Theoretical Basis Document (ATBD)". In: *ATBD Prepared under NASA Contract* (2016).

[47] Glynn C. Hulley. "High spatial resolution imaging of methane and other trace gases with the airborne Hyperspectral Thermal Emission Spectrometer (HyTES)". In: *Atmospheric Measurement Techniques* 9.5 (Jan. 2016), 2393–2408. DOI: 10.5194/amt-9-2393-2016.

[48] Glynn C. Hulley, Frank M. Göttsche, Gerardo Rivera, Simon J. Hook, Robert J. Freepartner, Maria Anna Martin, Kerry Cawse-Nicholson, and William R. Johnson. "Validation and Quality Assessment of the ECOSTRESS Level-2 Land Surface Temperature and Emissivity Product". In: *IEEE Transactions on Geoscience and Remote Sensing* (2021), pp. 1–23. DOI: 10.1109/TGRS.2021.3079879.

[49] D J Jacob, A.J. Turner, J.D. Maasakkers, J. Sheng, K. Sun, X. Liu, K. Chance, I. Aben, J. McKeever, and C. Frankenber. "Satellite observations of atmospheric methane and their value for quantifying methane emissions". In: *Atmos. Chem. Phys* (2016). DOI: 10.5194/acp-16-14371-2016.

[50] Jetse D. Kalma, Tim R. Mcvicar, and Matthew F. Mccabe. "Estimating Land Surface Evaporation: A Review of Methods Using Remotely Sensed Surface Temperature Data". In: *Surveys in Geophysics* 29.4-5 (Dec. 2008), 421–469. DOI: 10.1007/s10712-008-9037-z.

[51] P.S. Kealy and S.J. Hook. "Separating temperature and emissivity in thermal infrared multispectral scanner data: implications for recovering land surface temperatures". In: *IEEE Transactions on Geoscience and Remote Sensing* 31.6 (1993), pp. 1155–1164. DOI: 10.1109/36.317447.

[52] Yann H. Kerr, Jean Pierre Lagouarde, and Jacques Imbernon. "Accurate land surface temperature retrieval from AVHRR data with use of an improved split window algorithm". In: *Remote Sensing of Environment* 41.2-3 (1992), 197–209. DOI: 10.1016/0034-4257(92)90078-x.

[53] Felix N. Kogan. "Operational Space Technology for Global Vegetation Assessment". In: *Bulletin of the American Meteorological Society* 82.9 (2001), 1949–1964. DOI: 10.1175/1520-0477(2001)082<1949:ostfgv>2.3.co;2.

[54] Kevin Kohm. "Modulation transfer function measurement method and results for the Orbview-3 high resolution imaging satellite". In: *International Archives of the Photogrammetry, Remote Sensing and Spatial Information Sciences* 35 (Jan. 2004).

[55] L. Kuai, J.R. Worden, K.F. Li, G.C. Hulley, F.M. Hopkins, C.E. Miller, S.J. Hook, R.M. Duren, and A.D. Aubrey. "Characterization of anthropogenic methane plumes with the Hyperspectral Thermal Emission Spectrometer (HyTES): a retrieval method and error analysis". In: *Atmos. Meas. Tech* 9 (2016). DOI: 10.5194/atm-9-3165-2016.

[56] Jet Propulsion Laboratory. *data available at: http://hytes.jpl.nasa.gov*. last access: 22 January 2019.

[57] *LDCM Science and Mission Requirements Document*. July 2013.

[58] Ira Leifer, Daniel Culling, Oliver Schneising, Paige Farrell, Michael Buchwitz, and John P. Burrows. "Transcontinental methane measurements: Part 2. Mobile surface investigation of fossil fuel industrial fugitive emissions". In: *Atmospheric Environment* 74 (2013), pp. 432–441. ISSN: 1352-2310. DOI: https://doi.org/10.1016/j.atmosenv.2013.03.018. URL: https://www.sciencedirect.com/science/article/pii/S1352231013001842.

[59] Zhao-Liang Li, Bo-Hui Tang, Hua Wu, Huazhong Ren, Guangjian Yan, Zhengming Wan, Isabel F. Trigo, and José A. Sobrino. "Satellite-derived land surface temperature: Current status and perspectives". In: *Remote Sensing of Environment* 131 (Jan. 2013), 14–37. DOI: 10.1016/j.rse.2012.12.008.

[60] MODIS UCSB Emissivity Library. *data available at: https://icess.eri.ucsb.edu/modis/EMIS/html/em.html*. last access: 23 September 2019.

[61] K Masuda, T Takashima, and Y Takayama. "Emissivity of pure and sea waters for the model sea surface in the infrared window regions". In: *Remote Sensing of Environment* 24.2 (1988), pp. 313–329.

[62] Susan K. Meerdink, Simon J. Hook, Dar A. Roberts, and Elsa A. Abbott. "The ECOSTRESS spectral library version 1.0". In: *Remote Sensing of Environment* 230 (2019), p. 111196. ISSN: 0034-4257. DOI: https://doi.org/10.1016/j.rse.2019.05.015. URL: https://www.sciencedirect.com/science/article/pii/S0034425719302081.

[63] *Model 102 Hand Portable FT-IR Spectrometer*. URL: http://www.dpinstruments.com/products/model-102-hand-portable-ft-ir-spectrometer/.

[64] Andrea Molod, Lawrence Takacs, Max Suarez, Julio Bacmeister, In-Sun Song, and Andrew Eichmann. "The GEOS-5 atmospheric general circulation model: Mean climate and development from MERRA to Fortuna". In: *Technical Report Series on Global Modeling and Data Assimilation* 28 (2012).

[65] Juan C. Jimẽnex Muñoz, Josẽ A. Sobrino, Cristian Mattar, Glynn Hulley, and Frank-M. Goöttsche. "Temperature and Emissivity Separation From MSG/SEVIRI Data". In: *IEE Transactions on GeoScience and Remote Sensing* 52.9 (Sept. 2014), pp. 5937–5951.

[66] NASA. *Landsat data continuity mission thermal infrared sensor requirements document-revision f1*. Tech. rep. NASA Goddard Space Flight Center, 2012.

[67] *Observation Tech : Instruments*. URL: https://esto.nasa.gov/obs_technologies_iip.html.

[68] Onset. *Tidbit Datalogger Specifications*. 2020. URL: https://www.onsetcomp.com/products/data-loggers/utbi-001 (visited on 01/22/2021).

[69] V. Payan and A. Royer. "Analysis of Temperature Emissivity Separation (TES) algorithm applicability and sensitivity". In: *Int. J. Remote Sens.* 25.1 (2004), pp. 15–37. DOI: 10.1080/0143116031000115274.

[70] Leonardo F. Peres and Carlos C. Dacamara. "Land surface temperature and emissivity estimation based on the two-temperature method: sensitivity analysis using simulated MSG/SEVIRI data". In: *Remote Sensing of Environment* 91.3-4 (2004), 377–389. DOI: 10.1016/j.rse.2004.03.011.

[71] Venkatchalam Ramaswamy, K. Maskell, and C.A. Johnson. *The Third Assessment Report of the Intergovernmental Panel on Climate Change*. Ed. by J.T. Houghton, Y. Ding, D.J. Griggs, M. Noguer, P.J. van der Linden, and X. Dai. 2001.

[72] Antoni Rogalski. "Infrared detectors: status and trends". In: *Progress in Quantum Electronics* 27.2 (2003), pp. 59–210. ISSN: 0079-6727. DOI: https://doi.org/10.1016/S0079-6727(02)00024-1. URL: https://www.sciencedirect.com/science/article/pii/S0079672702000241.

[73] J W Rouse, R H Haas, J A Deering, and D W Deering. "Monitoring vegetation systems in the Great Plains with ERTS". In: *Third ERTS Symposium: abstracts Washington, D.C., December 10-14, 1973*. Goddard Space Flight Center, 1973, 309–317.

[74] Offer Rozenstein, Zhihao Qin, Yevgeny Derimian, and Arnon Karnieli. "Derivation of Land Surface Temperature for Landsat-8 TIRS Using a Split Window Algorithm". In: *Sensors* 14.4 (2014), 5768–5780. DOI: 10.3390/s140405768.

[75] Carl Salvaggio and Craig J Miller. "Comparison of field-and laboratory-collected midwave and longwave infrared emissivity spectra/data reduction techniques". In: *Algorithms for Multispectral, Hyperspectral, and Ultraspectral Imagery VII*. Vol. 4381. International Society for Optics and Photonics. 2001, pp. 549–558.

[76] Carl Salvaggio and Craig J Miller. "Methodologies and protocols for the collection of midwave and longwave infrared emissivity spectra using a portable field spectrometer". In: *Algorithms for multispectral, hyperspectral, and ultraspectral imagery VII*. Vol. 4381. International Society for Optics and Photonics. 2001, pp. 539–548.

[77] M. Saunois, R.B. Jackson, P. Bousquet, B. Poulter, and J.G. Canadell. "The growing role of methane in anthropogenic climate change". In: *Environmental Research Letters* 11.12 (Jan. 2016), p. 120207. DOI: 10.1088/1748-9326/11/12/120207.

[78] John R. Schott. *Remote sensing: the image chain approach*. 2nd ed. Oxford University Press, 2007.

[79] John R. Schott, Simon J. Hook, Julia A. Barsi, Brian L. Markham, Jonathan Miller, Francis P. Padula, and Nina G. Raqueno. "Thermal infrared radiometric calibration of the entire Landsat 4, 5, and 7 archive (1982–2010)". In: *Remote Sensing of Environment* 122 (2012). Landsat Legacy Special Issue, pp. 41–49. ISSN: 0034-4257. DOI: https://doi.org/10.1016/j.rse.2011.07.022. URL: https://www.sciencedirect.com/science/article/pii/S0034425712000375.

[80] ALICAT Scientific. *ALICAT MC Series Operating Manual*. 2020. URL: https://documents.alicat.com/manuals/DOC-MANUAL-MC.pdf (visited on 06/24/2021).

[81] H Shimoda and T Kimura. "1.09.2.9 - EOS-Terra/ASTER". In: *Comprehensive Remote Sensing*. Ed. by Shunlin Liang. Oxford: Elsevier, 2018, pp. 246 –279. ISBN: 978-0-12-803221-3.

[82] Malvina Silvestri, Vito Romaniello, Simon Hook, Massimo Musacchio, Sergio Teggi, and Maria Fabrizia Buongiorno. "First Comparisons of Surface Temperature Estimations between ECOSTRESS, ASTER and Landsat 8 over Italian Volcanic and Geothermal Areas". In: *Remote Sensing* 12.1 (2020). ISSN: 2072-4292. DOI: 10.3390/rs12010184. URL: https://www.mdpi.com/2072-4292/12/1/184.

[83] J Sobrino, C Coll, and V Caselles. "Atmospheric correction for land surface temperature using NOAA-11 AVHRR channels 4 and 5". In: *Remote Sensing of Environment* 38.1 (1991), 19–34. DOI: 10.1016/0034-4257(91)90069-i.

[84] S Solomon, D. Qin, Manning M., Z. Chen, M. Marquis, Averyt K.B., M. Tignor, and H.L. Miller. *IPCC: Climate Change 2007: The Physical Science Basis. Contribution of Working Group I to the Fourth Assessment Report of the Intergrovernmental Panel on Climate Change, Intergovernmental Panel on Climate Change (IPCC)*. 2007, p. 996.

[85] *Spectral Calc High-Resolution spectra; modeling*. URL: https://www.spectralcalc.com/calc/spectralcalc.php (visited on 06/25/2021).

[86] Huajun Tang and Zhao-Liang Li. *Quantitative Remote Sensing in Thermal Infrared Theory and Applications*. Springer Berlin, 2013.

[87] M. Teena and A. Manickavasagan. "Thermal Infrared Imaging". In: *Manickavasagan A., Jayasuriya H. (eds) Imaging with Electromagnetic Spectrum.* Springer, 2014. DOI: https://doi.org/10.1007/978-3-642-54888-8_8.

[88] Spectral Response of the Thermal Infrared Sensor. *data available at: https://landsat.gsfc.nasa.gov/sites/landsat/files/2013/06/TIRS_Relative_Spectral_-Responses.BA_.v1.xlsx*. NASA Landsat Science.

[89] A. K. Thorpe, C. Frankenberg, and D. A. Roberts. "Retrieval techniques for airborne imaging of methane concentrations using high spatial and moderate spectral resolution: application to AVIRIS". In: *Atmospheric Measurement Techniques* 7.2 (Oct. 2014), 491–506. DOI: 10.5194/amt-7-491-2014.

[90] A.K. Thorpe, C. Frankenberg, A.D. Aubrey, D.A. Roberts, A.A. Nottrott, T.A. Rahn, J.A. Sauer, M.K. Dubey, K.R. Costigan, C. Arata, A.M. Steffke, S. Hills, C. Haselwimmer, D. Charlesworth, C.C. Funk, R.O. Green, S.R. Lundeen, J.W. Boardman, M.L. Eastwood, C.M. Sarture, S.H. Nolte, I.B. Mccubbin, D.R. Thompson, and J.P. McFadden. "Mapping methane concentrations from a controlled release experiment using the next generation airborne visible/infrared imaging spectrometer (AVIRIS-NG)". In: *Remote Sensing of Environment* 179 (2016), pp. 104–115. ISSN: 0034-4257. DOI: https://doi.org/10.1016/j.rse.2016.03.032. URL: https://www.sciencedirect.com/science/article/pii/S0034425716301250.

[91] J. A. Voogt and T. R. Oke. "Effects of urban surface geometry on remotely-sensed surface temperature". In: *International Journal of Remote Sensing* 19.5 (1998), pp. 895–920. DOI: 10.1080/014311698215784. eprint: https://doi.org/10.1080/014311698215784. URL: https://doi.org/10.1080/014311698215784.

[92] J.A Voogt and T.R Oke. "Thermal remote sensing of urban climates". In: *Remote Sensing of Environment* 86.3 (2003), 370–384. DOI: 10.1016/s0034-4257(03)00079-8.

[93] Z. Wan, D. Ng, and J. Dozier. "Spectral emissivity measurements of land-surface materials and related radiative transfer simulations". In: *Advances in Space Research* 14.3 (1994), 91–94. DOI: 10.1016/0273-1177(94)90197-x.

[94] Zhengming Wan. "New refinements and validation of the collection-6 MODIS land-surface temperature/emissivity product". In: *Remote Sensing of Environment* 140 (2014), 36–45. DOI: 10.1016/j.rse.2013.08.027.

[95] Zhengming Wan and J. Dozier. "A generalized split-window algorithm for retrieving land surface temperature from space." In: *IEEE Trans. Geosci. Remote Sens.* 34 (1996), 892–905.

[96] Cody M. Webber and John P. Kerekes. "An examination of enhanced atmospheric methane detection methods for predicting performance of a novel muliband uncooled radiometer imager". In: *Atmospheric Measurement Techniques* 13 (2020), pp. 5359–5367.

[97] D. Weber, B.A. Marquez, C. Taylor, P. Raya, P. Contrera, D. Howard, I. Nwachuku, K. Fusco, F. Morales, and L.A. Doezema. "Macroseepage of methane and light alkanes at the La Brea tar pits in Los Angeles". In: *Journal of Atmos Chem* 74 (2017), pp. 339–356. DOI: 10.1007/s10874-016-9346-4.

[98] Qihao Weng. "Thermal infrared remote sensing for urban climate and environmental studies: Methods, applications, and trends". In: *ISPRS Journal of Photogrammetry and Remote Sensing* 64.4 (2009), 335–344. DOI: 10.1016/j.isprsjprs.2009.03.007.

[99] Qihao Weng, Dengsheng Lu, and Jacquelyn Schubring. "Estimation of land surface temperature–vegetation abundance relationship for urban heat island studies". In: *Remote Sensing of Environment* 89.4 (2004), 467–483. DOI: 10.1016/j.rse.2003.11.005.

[100] Brian N Wenny, Dennis Helder, Jungseok Hon, Larry Leigh, Kurtis J Thome, and Dennis Reuter. "Pre- and Post-Launch Spatial Quality of the Landsat 8 Thermal Infrared Sensor". In: *Remote Sensing* 7.2 (2015), pp. 1962–1980.

[101] R. Christ Wilson, Simon J. Hook, Phillip Scheider, and S. Geoffrey Schladow. "Skin and bulk temperature difference at Lake Tahoe: A case study on lake skin effect". In: *OURNAL OF GEOPHYSICAL RESEARCH: ATMOSPHERES* 118.18 (2013), pp. 10,332–10,34649. DOI: https://doi.org/10.1016/j.rse.2011.07.022. URL: https://doi.org/10.1002/jgrd.50786.

[102] Stephen J. Young, B. Robert Johnson, and John A. Hackwell. "An in-scene method for atmospheric compensation of thermal hyperspectral data". In: *Journal of Geophysical Research* 107.D24 (Dec. 2002). DOI: 10.1029/2001jd001266.